DEVELOPMENT OF PCB AND TEXTILE-BASED ULTRA-WIDEBAND METAMATERIAL-BASED ABSORBERS FOR 5G AND MM-WAVE APPLICATIONS

GÖKBERK AKARSU

Master's Thesis

Graduate School
Izmir University of Economics
Izmir
2022

DEVELOPMENT OF PCB AND TEXTILE-BASED ULTRA-WIDEBAND METAMATERIAL-BASED ABSORBERS FOR 5G AND MM-WAVE APPLICATIONS

GÖKBERK AKARSU

A Thesis Submitted to

The Graduate School of Izmir University of Economics

Master's Program in Electrical and Electronics Engineering

Izmir

2022

ABSTRACT

DEVELOPMENT OF PCB AND TEXTILE-BASED ULTRA-WIDEBAND METAMATERIAL-BASED ABSORBERS FOR 5G AND MM-WAVE APPLICATIONS

Akarsu, Gökberk

M.Sc. in Electrical and Electronics Engineering

Advisor: Prof. Dr. Diaa Gadelmavla

July, 2022

Metamaterials present extraordinary physical properties which conventional materials cannot exhibit, they present splendid opportunities to adjust the transmission, reflection, and absorption of the electromagnetic waves. Phenomenal properties of metamaterials attracted researchers to develop different types of metamaterials-based applications. The application areas of metamaterials are mainly related to the control of the reflected, absorbed, and the transmission of electromagnetic waves. The common applications including but not limited to, sensors, filters, antennas, solar cells, photodetectors, electromagnetic cloaking, and absorbers. The control of the absorption rates and minimization of reflected electromagnetic waves led to the development of metamaterial-based perfect absorbers which offers high absorptivity rates over a narrow bandwidths. Usage of metamaterial-based perfect absorbers are promising in the development of mm-Wave applications and RF energy harvesting systems however the proposed absorbers in literature cannot fulfil the wide-bandwidth requirements. In this study our developed designs are based on Rogers RT5880, FR-4 rigid substrates and textile-based materials, namely, Felt, Denim and Polyester fabrics. Obtained results show that our designs are ultra-wideband, in the ranges of 20 GHz to 70 GHz for textile-based 5G, mm-wave applications. Additionally, for 6G textile-based smart-wearable applications, a novel design is achieved around 114.4 GHz. For PCB-based applications, the outcomes show that the designs are ultra-wideband in the ranges from 10 GHz to 60 GHz. Comparison with other similar studies shows that our designs are compact in size, thin, and proposing ultra-wideband with reaching 99.99% absorptivity rates. The current designs are promising for future textile-based smart-wearable applications and for monitoring systems.

Keywords: Metamaterials, Metamaterial Absorbers, Ultra-wideband Absorbers, RF Energy Harvesting Systems, 5G, Millimeter-wave Applications.

ÖZET

5G VE MM DALGA UYGULAMALARI İÇİN PCB VE TEKSTİL TABANLI ULTRA GENİŞBANT METAMALZEME TABANLI SOĞURUCULARIN GELİŞTİRİLMESİ

Akarsu, Gökberk

Elektrik ve Elektronik Mühendisliği Yüksek Lisans Programı

Tez Danışmanı: Prof. Dr. Diaa Gadelmavla

Temmuz, 2022

Metamalzemeler, geleneksel malzemelerin sergileyemeyeceği olağanüstü fiziksel özellikler sunarlar, elektromanyetik dalgaların iletimini, yansımasını ve emilimini ayarlamak için muhteşem fırsatlar sunarlar. Metamalzemelerin olağanüstü özellikleri, araştırmacıları farklı türde metamalzeme tabanlı uygulamalar geliştirmeye çekti. Metamalzemelerin uygulama alanları temel olarak elektromanyetik dalgaların yansıması, soğurulması ve iletiminin kontrolü ile ilgilidir. Sensörler, filtreler, antenler, güneş pilleri, fotodedektörler, elektromanyetik gizleme ve soğurucuları içerir ancak yaygın kullanım alanları sadece bunlarla sınırlı değildir. Emilim oranlarının kontrolü ve yansıyan elektromanyetik dalgaların en aza indirilmesi, dar bir bant genişliği üzerinde yüksek emilim oranları sunan metamalzeme bazlı mükemmel soğurucuların geliştirilmesine yol açmıştır. Metamalzeme bazlı mükemmel soğurucuların kullanımı mm-Dalga uygulamalarının ve RF enerji hasat sistemlerinin geliştirilmesinde umut vericidir, ancak literatürde önerilen soğurucular geniş bant genişliği gereksinimlerini karşılayamamaktadırlar. Bu çalışmada geliştirilen tasarımlarımız Rogers RT5880, FR-4 rijit yüzeyler ve tekstil bazlı malzemeler olan Keçe, Denim ve Polyester kumaşlara dayanmaktadır. Elde edilen sonuçlar, tasarımlarımızın tekstil tabanlı 5G, mm dalga uygulamaları için 20 GHz ile 70 GHz aralığında ultra geniş bant olduğunu göstermektedir. Ayrıca 6G tekstil tabanlı akıllı giyilebilir uygulamalar için 114,4 GHz civarında yeni bir tasarım elde edilmiştir. PCB tabanlı uygulamalar için sonuçlar, tasarımların 10 GHz ila 60 GHz aralığında ultra geniş bant olduğunu göstermektedir. Diğer benzer çalışmalarla bir karşılaştırma yapıldığında, tasarımlarımızın boyut olarak kompakt, ince ve %99,99 soğurma oranlarına ulaşan ultra geniş bant önerdiğini gösteriyor. Mevcut tasarımlar, gelecekteki tekstil tabanlı akıllı giyilebilir uygulamalar ve izleme sistemleri için umut vericidir.

Anahtar Kelimeler: Metamalzemeler, Metamalzeme Soğurucular, Ultra geniş bant soğurucular, RF enerji hasadı sistemleri, 5G, Milimetre-dalga uygulamaları.

To my family…

ACKNOWLEDGEMENTS

I would like to express my greatest appreciation to my supervisor, Prof. Dr. Diaa Gadelmavla for his continuous support, wonderful supervision, and motivation, constructive and valuable comments along my graduate and undergraduate studies. I feel very motivated and proud to become his student, thanks to his supreme leading I am improving myself continuously for the goals I desire.

I would like to express my appreciation to Prof. Dr. A. Allam for his valuable and continuous support and enlightening feedbacks, for his great ideas and for his help in the fabrication and measurements.

Many thanks to Dr. Hany Taher for his fruitful discussions during the preparation of my publications.

I also express my sincerest gratitude to my mother, my father and my sister for their all-time support, motivation, moral and encouragements. I am so grateful and proud to be their son and very happy to be brother of my sister.

TABLE OF CONTENTS

LIST OF TABLES

LIST OF FIGURES

CHAPTER 1: INTRODUCTION

The demands for electricity, telecommunication systems, transportation, connectivity, healthcare, and the need for self-defense are linearly increasing year by year. Advances from the invention of gunpowder to steam train, power generation with primitive motors and coils, light bulb, automobile, and radio increased the necessity of extra energy resources and raw materials. In the course of history, the humankind developed water wheels, windmills, transformers, batteries, hydroelectric plants, thermal power plants and even nuclear plants to supply the tremendous demands for energy.

The evolution of new technologies comes with the requirements of power supply, camouflage, interference and shielding. To meet the demands of new technologies' requirements, various developments such as electromagnetic wave absorbers, camouflage applications, shielding systems, stealth applications, RF energy harvesting, 5G applications, 6G applications, mm-wave applications have been proposed in the literature.

Electromagnetic wave absorbers are structures that are designed to absorb electromagnetic waves at a certain region of the spectrum regarding their nature (Costa et al., 2016). During World War II, the development of electromagnetic wave absorbers was advanced to reduce the reflection of interfering objects, which resulted in the development of the radar camouflage applications. German scientists developed absorption configuration structures with flexible rubber sheets which they loaded with iron powder and the Jaumann absorber. On the other side, the scientists from the United States developed rubber sheets exhibiting behavior of resonant absorber with a concentrated iron particles and this resonant absorber was named as Salisbury screen absorber.

The Salisbury screen structure is consisted of resistive sheet with a 377-ohm resistance, and it is located at about a quarter-wavelength ($\lambda/4$) from the reflective surface. The absorption bandwidth of this structure was narrow due to its resonance behavior (Chambers and Tennant, 2006). For higher bandwidths the Jaumann absorber is referred to as an extension of the Salisbury screen because it is composed of two or

more resistive sheets separated by a quarter-wavelength ($\lambda/4$), allowing multiple resonances to occur at multiple wavelengths with minimal reflections, resulting in a broadband absorption (Knott and Lunden, 1995). The absorption of the Jaumann absorber can be enhanced by the addition of new layers, therefore, resulting into thick and bulky structures. The Dällenbach layer structure refers to absorbers that are made up of a single high-lossy layer and a ground plane. The idea behind this structure is to minimize reflection on the surface while utilizing the high-lossy layer to absorb incident radiation. Circuit Analog (CA) absorbers are another type of electromagnetic wave absorber; they are made up of one or more-layer sheets with resistive and reactive elements arranged in a periodic array on a single ground layer (Munk et al., 2007). CA absorbers can achieve high absorption over a wide range of frequencies. The background of this studies opened a new way to the development of electromagnetic absorber-based applications such as camouflage, shielding, stealth technologies.

RF energy harvesting is a technique the ambient electromagnetic waves and convert them into usable energies. The obtained output energy could be AC or with the use of a proper matching network and rectifiers it could be DC as well. (Amer et al., 2020). The experimental records of the RF energy harvesting systems can be traced back to the 1960s, when William Brown proposed an experimental study in 1969 (Brown, 1969). In this experiment a small helicopter structure, a focusing antenna, a rectifying antenna and a microwave generator were used to harvest the microwave energies. The frequency band in that structure was 2.45 GHz with a 5-kW magnetron microwave generator source, and the focusing antenna; also known as the transmitting antenna, it was used to direct the microwave energy into a narrow beam. The rectenna used in that experiment could produce about 270 watts of DC power and was enough to operate the 5 lb. helicopter with an altitude of 50 feet for about 10 hours continuously. The concept and idea of this study opened a new era for new developments in this field.

Powering portable or difficult-to-reach instruments, motors, sensors, electronics, and systems necessitate the use of generators or batteries, which have numerous drawbacks. The usage of batteries causes numerous limitations on the system, primarily the life-time of batteries are definite and of hand the batteries' life-times also depend on the temperature, moisture, power consumption and chemical reactions in the batteries (Diouf and Pode, 2015). Secondly, batteries are harmful for

the environment because of the many toxic elements they contain. In addition, they continuously require to be recharged in a process that decreases the battery capacity due to the chemical reactions (Tröltzsch et al., 2006). Furthermore, eventually batteries may require to be replaced and all-time cycle of production of the new batteries affect the environment, and increase the cost, and the need of raw materials.

In order to overcome these constraints of battery needs, self-consistent systems (energy harvesters) can dispose the necessity of and replacing batteries. The employment of self-consistent systems could supply infinite energy or close to the limitless operating life especially to low-powered devices (Piñuela et al., 2013). Since the harvested energy from RF energy systems are clearly minor in milliwatt (mW) or microwatt (μW) levels, the following parameters need to be continuously optimized and enhanced. They are namely, the radiation efficiency of the receiver antenna, the conversion efficiency of the rectifier circuit and matching network, the amount of the generated RF power, the aperture of the antenna, and the gain of the antenna. The target is to achieve obtain maximum harvesting from the RF energy sources and to increase the bandwidths of the receiver antenna and rectifier circuit (Georgiadis et al., 2021). Researchers proposed several studies and designs as reported in the literature for RF energy harvesting solutions and to and resolve the efficiency issues, and to improve the operating bandwidth (Lu et al., 2015).

In 2020s, the internet of things (IoT) as planned to integrate sensors, biomedical implants, smart wearable technologies, self-driving autonomous cars, unmanned aerial vehicles (UAVs), smart home appliances, and indeed smart cities necessitate the need for massive number of high bandwidths connected networks. Furthermore, when third generation (3G) and fourth generation (4G) communication technology networks began to fall short of today's standards in terms of speed, stability, accessibility, and channel capacity, new researches were focused on higher frequency (mm-waves) communication technologies which led to the emergence of the 5^{th} Generation (5G) standards, and to the first steps toward a 6^{th} Generation (6G). Reaching extremely fast speeds requirements, all time accessibility, low latency, and stability are just few of the benefits and promises that 5G and 6G will bring in future (Andrews et al., 2014).

The 5G technology is based on two frequency spectra, the sub-6 GHz, and the

millimeter-wave (mm-Wave) frequency ranges. The sub-6 GHz band operates at frequencies below 6 GHz and, while it is close to the LTE and 4G spectra, the provided speed and bandwidth are not as high as in mm-Wave ranges. However, because low frequency signals can penetrate obstacles better than mm-Waves, also can overcome the atmospheric attenuation, and are very appropriate for larger geographical area coverages. However, the speed and bandwidth limitations of the sub-6 GHz band are no longer sufficient for future infrastructure, so the requirements of larger bandwidths, faster speeds, and lower latencies have led to the use of mm-Wave band applications. This utilization of the mm-Wave band also opens a way to the development of future studies such as the 6G communication technology (Saad et al., 2020).

However, up to now most of the suggested studies cannot fulfill the needs for the aforementioned applications in term of the operation bandwidth, compactness, stability, lightness, dimension, size, absorption rate, cost, ease of manufacture and flexibility in integration.

These requirements can be met by employing metamaterials and taking advantage of their numerous applications at various operating frequencies.

The word of metamaterial originates from the meta- and material which depicts that the materials are beyond the natural ones. Simply they are structures which artificially tailored to exhibit exclusive electromagnetic properties do not ordinarily found in nature. The concept and theory of modern metamaterials are firstly introduced by the Russian scientist Victor Veselago in 1967 which theoretically suggested the double negative materials hypothesis (Veselago, 1968). The Veselago's work suggested the left-handed materials and their special electromagnetic features such as reverse doppler effect, Snell's law and Vavilov-Cherenkov radiation effect (Lai *et al.*, 2004). Veselago identified the materials as right-handed and left-handed materials, according to plane monochromatic wave, if electric permittivity and magnetic permeability are larger than zero ($\varepsilon > 0$) and ($\mu > 0$) the E, H and K form right-handed vectors and, if they are both less than zero ($\varepsilon < 0$) and ($\mu < 0$) they form left-handed vectors.

The left-handed vectors are the opposite vectors of the right-handed vectors which form a right-handed materials and they are referred as left-handed materials or double negative materials. Left-handed materials sustain electromagnetic waves with

phase and group velocities which they travels in the opposite directions or termed as backward-waves. This phenomenon is the reverse of the right-hand rule and differs from conventional material's vector properties, so materials that exhibit these supernatural inverse vector properties are termed as metamaterials.

The stimulation of negative index materials attracted scientists to investigate and develop extra scientific works, in the end of 90's, John Pendry and this collaborators theoretically simulated and experimentally proved that the effective negative magnetic permeability, and the effective negative electric permittivity are possible. Pendry and his collaborators proposed microstructures that exhibit effective magnetic permeability which can be arranged to form various microstructures, continuous wire structure showing negative permeability. These microstructures gave a potential to develop artificial materials with negative permeability, and this is explained by the structure of the split ring resonators yielding a capacitive resonance (Pendry et al., 1998). Pendry and collaborators also developed a medium which has effective negative electric permittivity at microwave regions with a usage of split ring resonators (Pendry et al., 1999). They also developed a study with a negative refractive index, a super lens which presents beyond the refractive index (Pendry, 2000). Pendry's work was focused on the development of super lenses with the usage of negative refraction, this led to the suppression of the limitations of the wavelength of the light. They assumed that the unit cell of the microstructures are less than the wavelength of the radiation and a periodic array of nonmagnetic conducting elements results with approximation of the excellent effective medium.

In the year 2000, D. R. Smith and collaborators have developed a composite medium which has double negative properties of effective permeability $\mu_{eff}(\omega)$ and permittivity $\varepsilon_{eff}(\omega)$ in the microwave region (Smith et al., 2000). They claimed that the combination of the negative permeability and negative permittivity in the specified regions could results with double negative left-handed material. This structure allowed to first experimental verification of the left-handed materials, they fabricated split ring resonators on a printed circuit board with a lattice spacing of $\lambda_0/4$ between nonmagnetic array elements and addition of the fabricated split ring resonators to the wire cylindrical array in a parallel, they created a passband in a specified frequency. This study is the first tailored material with a both double negative permittivity and permeability features allowing the development of new metamaterial studies. These

studies pioneered the concept of new metamaterials with the possibility of producing metamaterials from conventional materials by arranging normal structures according to wavelength, geometry, and material types.

Advancements on the metamaterials gave enormous increase to development of metamaterial-based applications and studies. In the past several years, with the improvements and requirements in emergent technologies, various studies were proposed for the different type of applications such as electromagnetic cloaking (Schurig et al., 2006), sensors (Chen et al., 2012), wireless power transfers (WPT) (Wang et al., 2011), antennas (Dong and Itoh, 2012), super lenses (Pendry, 2000), filters (Gil et al., 2007), magnetic resonance imaging (MRI) scanners (Freire et al., 2011), energy harvesting systems (Din et al., 2012), sound acoustics (Cummer et al., 2016), solar cells (Rufangura and Sabah, 2015), radars (Iwaszczuk et al., 2012), radomes (Perhirin and Auffret, 2013), shieldings (Lv et al., 2019), semiconductors (Hoffman et al., 2007) and, absorbers (Watts et al., 2012). These applications were suggested nearly for the whole range of electromagnetic spectrum, and the frequency range of this applications are dependent on the utilization type of desired purpose. The exotic behaviors of metamaterials attracted many researchers to conduct studies namely in metamaterial-based applications and metamaterial-based absorbers.

Metamaterial-based absorbers are tailored electromagnetic wave absorbers that exhibit unusual properties such as near to zero reflectivity, wide bandwidth, ability to operate over wide oblique incident angles, different polarization angles as a result of the zero reflectivity.

The first metamaterial-based perfect absorber was proposed in 2008 by Landy and his collaborators (Landy et al., 2008). This work claimed that it is possible to absorb incident electric and magnetic fields by controlling both the electric permittivity ε and magnetic permeability μ. This can be achieved by matching both ε and μ with respect to the impedance of free space which causes minimum reflectivity. The same study stated that metamaterials can be designed to produce narrow-band perfect absorbers. They designed one single unit cell of the absorber consisting of two metallic elements named as electric ring resonator (ERR), a dielectric substrate and split-wire for the designing of perfect metamaterial-based absorber. In this work they also claimed that the electric field and the magnetic field can be tuned with respect to

the substrate thickness, geometry of the ERR and the cut wire, by tuning these parameters, the effective electrical permittivity ε_{eff} and magnetic permeability $\mu_{eff\ are}$ also tuned. Their theoretical simulation results showed that at frequency of 11.5 GHz, the structure could reach 96% absorption rates. Their measurements with a fabricated FR-4 structure of about 0.2 mm thickness showed 88% absorption rate. The narrow-band perfect absorption behavior of their structure was explained by the limitations on the copper thickness, minimized copper width fabrication tolerances. They fabricated the structure with an array of 15 x 15 cm prototype FR-4 board and they pointed out that the fabrication of the structure affects the simulation results. They pointed out that possible potential application of their metamaterial-based structure was bolometer. They also claimed the possibility of their metamaterial-based absorber to absorb energies at other wavelengths such as mm-Wave and THz frequencies which allows for high resolution imaging. This particular study led the way to new metamaterial-based perfect absorbers at many operating frequencies. The enormous advantages of metamaterials and their fantastic reconfigurable features also motivated metamaterial-based RF energy harvesting applications.

Metamaterial-based energy harvesting application was developed as a split ring resonator (SRR) structure by O. Ramahi and his collaborators (Almoneef and Ramahi, 2013). They suggested a unit cell structure that made of Rogers RT5880 substrate with a thickness of 0.79 mm, the SRR design and a soldered resistive element for the AC microwave energy harvesting with resistive a resistor element of about 2.3 KΩ which operated at 5.8 GHz. For the experiment they prepared an array of 9 x 9-unit cells with a resistor value of 2.7 KΩ and they indicated that their initial aim was the conversion of electromagnetic wave energy into AC energy with an experimental proof. So, the presented study showed that these metamaterial structures have great potential for electromagnetic energy harvesting applications.

In recent years, more metamaterial-based energy harvesting designs were proposed in the literature, for instance a study by Cheng (Cheng et al., 2016) suggested that a metamaterial perfect absorber can be utilized for electromagnetic energy harvesting applications. Cheng and his collaborators proposed an electric-inductive-capacitive (ELC) resonator unit cell with dimensions of 8 x 8 x 1.6 mm^3, a Rogers RT6010 substrate, a 190 Ω resistor. Their proposed unit cell design was operating at 2.65 GHz with close-to-unity absorption rates. It is important to indicate here that,

even the achieved close-to-unity absorption rate, the proposed absorber design was suffering from narrow-band limitations.

For widening the absorption bandwidth and increasing the absorption bands of the metamaterial-based microwave energy harvesting absorbers, several studies were suggested in the literature, some of the techniques include the usage of multi-layer structure (Karaaslan et al., 2017) and usage of high losses resistive elements (Karaaslan et al., 2018).

Apart from all the conventional rigid counterparts PCB-based metamaterial absorbers also several studies were designed on the flexible substrates (Yoo et al., 2014; Ha et al., 2021). Recently, textile-based flexible absorbers are promising for futures new technologies for instance smart wearable technologies, self-consistent smart wearable systems (Akarsu et al., 2022; Tao et al., 2008; Xin et al., 2017). The textile-based wearable applications are very promising for future especially if they support high frequencies and of course because of their flexibility and compactness. Tak and his colleagues designed a unit cell for the radar indoor clear applications, using a Felt substrate with a 1 mm thickness and it was able to absorb more than 90% of the incident energy with dual-band in the range frequencies of 9.0 and 9.8 GHz (Tak and Choi, 2017). Mohammed and colleagues designed a reconfigurable metamaterial absorber's unit cell with a 2 mm Felt substrate and a varactor diode operated over the frequency range of 4.9-5.06 GHz (Bait-Suwailam et al., 2019).

Up to now, most of the proposed studies were not successful to accomplish all requirements of future's smart wearable applications and mm-Wave applications such as compactness, lightness, low profile structure, wide incident angle, ultra-wideband behavior, reaching high absorptivity rates, supporting of higher operating frequencies, flexibility, and easy fabrication.

The main tasks of the current research work are: 1) development of ultra-wideband PCB-based metamaterial absorbers to collect more electromagnetic energy from 5G and mm-Wave sources, 2) development of state-of-the-art self-consistent textile-based absorbers, 3) development of compact sized ultra-wideband ultra-thin metamaterial-based absorber systems for mm-Wave applications, 4) enhancements of the absorptivity rates at higher angles of incidents for ultra-wideband metamaterial-based absorbers, 5) enhancement of

bandwidth and absorptivity rates of symmetric narrow-band metamaterial absorbers, 6) development of metamaterial absorbers for future's promising 6G applications.

This thesis structured as followed: in Chapter 2, the theoretical background of metamaterials and methodology we employed in this thesis are explained. In Chapter 3, the developed and specifically designed metamaterial-based absorbers were presented together with the simulation and experimental results. Finally, a brief conclusion for the developed metamaterial absorbers and their promising fields are presented.

CHAPTER 2: THEORITICAL BACKGROUND AND METHODOLOGY

Summary: In this chapter, the background electromagnetic equations and the classification of materials are briefly explained. The theoretical background of the metamaterials and characterization of metamaterial-based absorbers are explained with their related equations. The numerical methods and used techniques of computations and the measurement of metamaterial-based absorbers are clarified. The computation of the scattered waves and the methodology used in this study are clearly described. Finally, the development and the design of the metamaterial-based absorber are described in details, including the use of appropriate dielectric materials, the significance of geometrical shapes, symmetries, fabrication techniques, and the test setup are also explained.

2.1. Background Equations

Maxwell equations are laws that govern the behaviors of electromagnetic wave, the propagation of an electromagnetic wave across a medium, and how the electromagnetic wave interacts with objects (Turnbull, 2013). These equations are the basis of electromagnetism fields and propagation of electromagnetic waves. They were established by James Clerk Maxwell in 1873 (Achard, 2005). Considering the electric and the magnetic fields are time harmonics with a time convention factor of $e^{i\omega t}$, Maxwell's phasor form of the equations can be expressed as in Eqn. 1-4,

$$\nabla \times \boldsymbol{E} = -i\omega \boldsymbol{B} \tag{1}$$

$$\nabla \times \boldsymbol{H} = i\omega \boldsymbol{D} + \boldsymbol{J} \tag{2}$$

$$\nabla \cdot \boldsymbol{D} = \rho \tag{3}$$

$$\nabla \cdot \boldsymbol{B} = 0 \tag{4}$$

where, E represents the electromagnetic field vector $[V/m]$, H represents the magnetic field vector $[A/m]$, D represents the electric flux density vector $[C/m^2]$, B represents the magnetic flux density vector $[wb/m^2]$, ρ represents the charge density $[C/m^3]$, and the J is the current density vector $[A\ /\ m^2]$.

These equations were derived from theories by Gauss' and Stokes' as written in Eqn. 5-8.

$$\oint_C \boldsymbol{E} \cdot dl = -i\omega \int_s \boldsymbol{B} \cdot ds \tag{5}$$

$$\oint_C \boldsymbol{H} \cdot dl = i\omega \int_s \boldsymbol{D} \cdot d_s + \int_s \boldsymbol{J} \cdot ds \tag{6}$$

$$\oint_S \boldsymbol{D} \cdot ds = \int_V \rho \cdot dv \tag{7}$$

$$\oint \boldsymbol{B} \cdot ds = 0 \tag{8}$$

The electric flux density vector ($\boldsymbol{D}$) and the magnetic flux vector are expressed in free space by Eqn. 9-10.

$$\boldsymbol{D} = \varepsilon_0 \boldsymbol{E} \tag{9}$$

$$\boldsymbol{B} = \mu_0 \boldsymbol{H} \tag{10}$$

Where: ε_0 is electric permittivity, μ_0 is magnetic permeability of free space. with values of $\epsilon_0 = 8.854 \times 10^{-12} \cong \frac{10^{-9}}{36\pi}[f\ /\ m]$, $\mu_0 = 4\pi \times 10^{-7}[H\ /\ m]$.

The electric permittivity (ε), magnetic permeability (μ), and conductivity (σ) relate the electric flux density (D), magnetic flux density (B), and electric current density (J), respectively as shown in Eqn. 11-13

$$\boldsymbol{D} = \varepsilon \boldsymbol{E} \tag{11}$$

$$\boldsymbol{B} = \mu \boldsymbol{H} \tag{12}$$

$$\boldsymbol{J} = \sigma \boldsymbol{E} \tag{13}$$

The electric permittivity, magnetic permeability, and the electrical conductivity of the medium are represented as $[F/m]$, $\mu\,[H/m]$, $\sigma\,[S/m]$, respectively. The permittivity and magnetic permeability of the materials are important in determining their ability to store electric and magnetic energies, respectively. Their general forms can be written as depicted in Eqn. 14-15.

$$\varepsilon = \varepsilon_r \varepsilon_0 = \varepsilon' - j\varepsilon'' = \varepsilon_0(1 + x_\varepsilon) \tag{14}$$

$$\mu = \mu_r \mu_0 = \mu' - j\mu'' = \mu_0(1 + X_m) \tag{15}$$

Where: x_ε, and X_m are the electric and magnetic susceptibilities, respectively. The relative permittivity (ε_r) or the dielectric constant (ε_r) is a measure of a materials ability to store the electrical fields. The relative permeability μ_r is a measure of the materials' ability to store magnetic fields.

A material with low conductivity but with a relative permittivity constant (ε_r) greater than 1.0 is named as dielectric material. Materials with higher dielectric constants can store more electrical energies but it should be noted that increasing the dielectric constants maximizes the dielectric losses at higher frequencies (Campo, 2008). So, the dielectric losses are the key factors for high frequency microwave-based applications.

2.2. Classification of Materials

Materials can be divided into four sections according to their permittivity and permeability values as shown in Fig. 1, materials with positive permittivity and permeability values ($\varepsilon > 0$, $\mu > 0$) are considered as double positive (DPS) materials. Materials with permittivity values less than zero and permeability values greater than

zero ($\varepsilon < 0, \mu > 0$) are termed as epsilon negative (ENG) materials. As aforementioned before, materials with both negative electric permittivity and magnetic permeability are termed as double negative (DNG) materials. Natural materials cannot exhibit both negative permeability and permittivity values and this class is only possible with artificially tailored engineering methods. Materials with permittivity value greater than zero and permeability less than zero ($\varepsilon < 0, \mu > 0$) are termed as mu-negative (MNG) materials. The permittivity and permeability can also define the refractive index of the material, the characteristic impedance, and the wave number where k_0 which is the free-space wave number and they are all given in Eqn. 16-18, respectively.

$$n = \pm\sqrt{\varepsilon\mu} \tag{16}$$

$$\eta = \sqrt{\frac{\mu}{\varepsilon}} \tag{17}$$

$$k = k_0\sqrt{\varepsilon\mu} \tag{18}$$

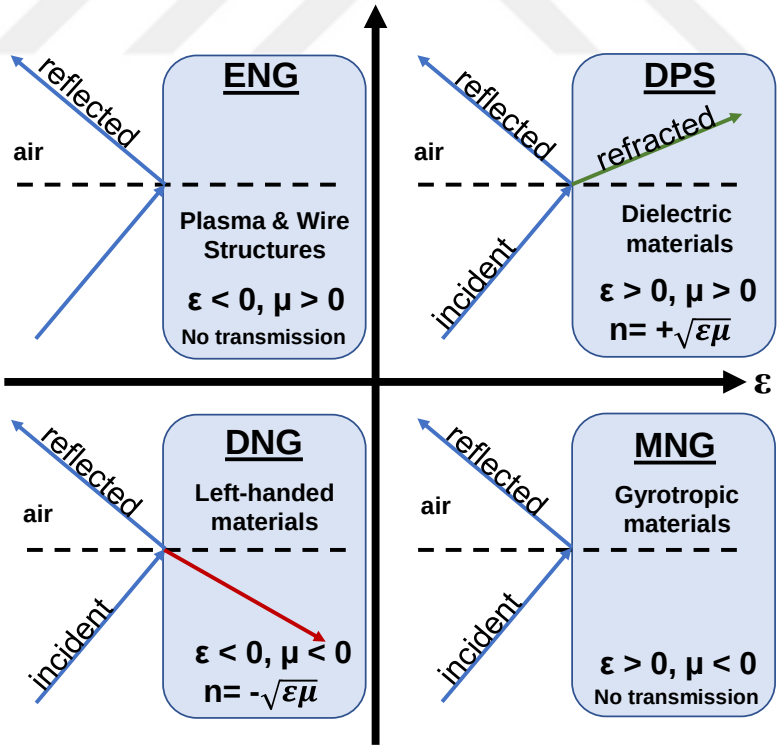

Figure 1. Classification of materials based on the permittivity (ε) and the permeability (μ) values.

2.2.1. Double Positive Materials (DPS Materials)

DPS materials represent right-handed type of materials and obeys the right-hand rule, these materials can be found in nature and named as conventional materials. The dielectrics are good example of the DPS materials.

2.2.2. Epsilon Negative Materials (ENG Materials)

The ENG materials are depicted as electric plasmas which support evanescent waves at optical and microwave frequencies. Normally, silver, gold, aluminum only display negative permittivity at optical frequencies. The first ENG materials at the microwave frequencies was developed and was experimentally proved by the J. Pendry and his colleagues (Pendry et al., 1998). They periodically placed an array of thin wires to having epsilon negative medium at the microwave region. They structure was based on thin wires which were represented with a radius *r* and a unit cell side length represented by *a*. Furthermore, they explained that if the incident electromagnetic wave's wavelength coming through the structure is larger than the unit cell side length ($\lambda >> a$), the electrons will generate a negative medium where the electrical field propagate through the whole structure. The representation of the array of thin wires structure is given in Fig. 2.

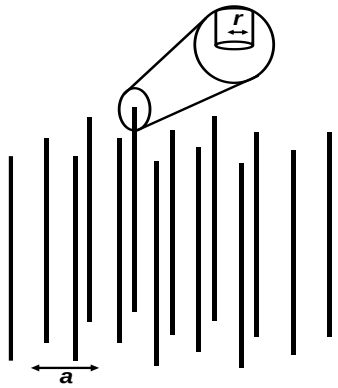

Figure 2. Array of thin wires aligned with respect to the unit cell side length *a* and radius with *r*, (Source: Pendry et al., 1998).

The plasma frequency of the metals can be calculated as given by Eqn. 19.

$$\omega_p^2 = \frac{n_e^2}{\varepsilon_0 m_e} \tag{19}$$

where n is the electron density, e is the charge of electron and m is the mass of electron. The plasma frequency of metals can be calculated from the square root of the ω_p^2. Metals with oscillating frequencies less than that of the plasma frequency show negative ε values.

The movements of the electrons are restricted within the thin wires and in the media, electrons will form effective electron density and electron mass as given by Eqs. 20-21,

$$n_{eff} = n\frac{\pi r^2}{a^2} \tag{20}$$

$$m_{e_{ff}} = \frac{\mu_0 N_e^2 \, r^2 \, ln\, a/r}{2} \tag{21}$$

Where: n is the density of the electrons in the wires, r is the radius of the wire and a is the unit cell side length of the square lattice with the thin wires being periodically arranged. For a significantly thin wire, the effective electron density can be smaller than the electron density, which considerably decreases the medium's plasma frequency.

The same authors gave an example about the deduction of plasma frequency to the microwave regions, using of a thin array of wires structure with a 1.0 x 10^6 mm radius, a unit cell side length of 5 mm, an electron density of 1.806 x 10^{29} m^{-3} of aluminum. The classical equation of the plasma frequency given by Eqn. 22.

$$\omega_p^2 = \frac{n e_{ff} e^2}{m e_{ff} \varepsilon_0} = \frac{2\pi c_0^2}{a^2 \, ln(a/r)} \tag{22}$$

where, c_0 is the speed of light in free-space, the obtained value in the microwave region is ω_p = 5.15 x 10^{10} rad s^{-1} = 8.20 GHz.

The created negative medium which resulted with a tuned electron density and electron mass, has an effective plasma frequency at the microwave region of the electromagnetic spectrum.

2.2.3. Mu Negative Materials (MNG Materials)

MNG materials are gyrotropic and gyromagnetic materials that are exhibiting negative permeability in nature. To artificially generate the MNG material, initially a split ring resonator structures were proposed and designed (Pendry et al., 1999) as shown in Fig. 3.

Figure 3. An illustration of the split ring resonator (SRR) structure.

The designed SRR structure acts like a RLC circuit, the circular ring creates a resistance and inductance, and the cut areas (the open-ended edges) are the capacitance. The magnetic field component of the electromagnetic wave transmitted over the SRR structure is set to be perpendicular to the structure. This perpendicular magnetic field induces current on each split ring. The magnetic flux loss between the rings at each column is negligible if the rings are very close to each other, thus the magnetic flux is given by Eqn. 23.

$$\phi = \frac{\mu_0 \pi r^2 I}{l} \tag{23}$$

Where l represent the distance between each SRR, r is the radius of the circular ring.

The inductance value of each ring can be calculated as shown by Eqn. 24

$$L = \frac{\phi}{I} = \frac{\mu_0 \pi r^2}{l} \tag{24}$$

The ring-generated depolarizes the magnetic flux lines which are uniformly distributed across the medium resulting into mutual inductance between the SRRs. The equation of the mutual inductance is given by Eqn. 25.

$$M = \frac{\pi r^2}{a^2} L = FL \tag{25}$$

where F represent the fractional volume of the unit cell employed by the SRR form. Wartak and his colleagues assumed that the magnetic field is incident on the SRR structure as shown by Eqn. 26,

$$H = H_0 e^{i(w_t - k \cdot r)} \chi \tag{26}$$

And the induced source is generating an electric current I in each rings as given by Eqn. 27. According to Eqs. 26 and 27 they applied Ohm's second law on closed SRR circuit to obtain relative effective magnetic permeability of the medium which is calculated with the Eqs. 27-31 (Wartak Marek S. et al., 2011).

$$U = i\omega\mu_0\pi_r^2 H_0 \tag{27}$$

$$U = [R + i\ /\ (\omega C) - i\omega L + i\omega M]I \tag{28}$$

Where, R is the ohmic resistance of each SRR ring,

$$R = 2\pi r\sigma \tag{29}$$

$$I = -\frac{H_0 l}{(1-F) - \frac{1}{(\omega^2 LC)} + \frac{iR}{(\omega L)}} \tag{30}$$

$$\mu_r = 1 - \frac{F}{1 - \frac{1}{(w^2 LC)} + \frac{iR}{(\omega L)}} \tag{31}$$

the relative effective magnetic permeability is calculated according to Eqs. 23-31 and it is pointed out that the magnetic permeability has negative value in the range of: $\frac{\mathbf{1}}{\sqrt{\boldsymbol{LC}}} < \boldsymbol{\omega_p} < \frac{\mathbf{1}}{\sqrt{\boldsymbol{LC}(\mathbf{1}-\boldsymbol{F})}}$, in addition they mentioned about the importance of the resonant frequency of the structure which depends on the SRR rings' inductance (L), capacitance (C) and the periodicity of structure.

Hereby, the possibility of having double negative materials is enabled by having both negative effective electric permittivity (ε) and negative effective magnetic permeability (μ) with the utilization of ENG and MNG materials, respectively.

2.2.4. Double Negative Materials (DNG Materials)

DNG materials represent the left-handed materials and do not obey the right-hand rule which is not possible for conventional materials obeying the natural constraints. As aforementioned, the DNG materials which exhibit non-natural features are called metamaterials. To clarify the waves propagation in double negative medium and to explain the extraordinary properties of metamaterials, Maxwell's equations are employed as given in Eqs. 32-41.

$$\nabla \times E = -\mu_0 \mu_r \frac{\partial H}{\partial t} \tag{32}$$

$$\nabla \times H = \varepsilon_0 \varepsilon_r \frac{\partial E}{\partial t} \tag{33}$$

$$\nabla^2 E = -\varepsilon_0 \mu_0 \varepsilon r \mu_r \frac{\partial^2 E}{\partial t^2} \tag{34}$$

$$\nabla^2 H = \varepsilon_0 \mu_0 \varepsilon_r \mu_r \frac{\partial^2 H}{\partial t^2} \tag{35}$$

For time-harmonic and plane wave fields are stated on Eqs. 36-37.

$$E = E e^{i(\omega t - k_r)} \tag{36}$$

$$H = H e^{i(\omega t - k_r)} \tag{37}$$

As stated above the time-harmonic and plane monochromatic wave fields are proportional to $e^{i(\omega t - k_r)}$ and they can be reduced as given in Eqs. 38-39.

$$\boldsymbol{k} \times \boldsymbol{E} = \omega |\mu| \boldsymbol{H} \tag{38}$$

$$\boldsymbol{k} \times \boldsymbol{H} = -\omega |\varepsilon| \boldsymbol{E} \tag{39}$$

So, it is clear that the three vectors, the electric field intensity vector $\boldsymbol{E}$, the

magnetic field intensity vector $\boldsymbol{H}$ and the wave vector $\boldsymbol{k}$ form the right-hand rule for a DPS medium.

For a DNG materials or as stated before the metamaterials plane wave propagations are controlled by Eqs. 40-41.

$$\boldsymbol{k} \times \boldsymbol{E} = -\omega|\mu|\boldsymbol{H} \tag{40}$$

$$\boldsymbol{k} \times \boldsymbol{H} = \omega|\varepsilon|\boldsymbol{E} \tag{41}$$

So, for $\varepsilon < 0$, and $\mu < 0$ they form left-handed triplet vectors, which is theoretically proven by V. Veselago (Veselago, 1968).

The propagation of wave direction follows the backward direction in these mediums. Due to the negative permeability, and permittivity the refractive index of this materials are negative also, they also known as negative index materials (NIMs).

The direction of poynting vector can be defined as given by Eq. 42 (independent of the medium either DPS or DNG):

$$\boldsymbol{S} = \frac{1}{2} Re[\boldsymbol{E} \times \boldsymbol{H}^*] \tag{42}$$

In DNG medium, the **S** poynting vector is at the opposite direction to wave propagation vector $\boldsymbol{k}$ as shown in Fig. 4. The direction of poynting vector is not related to the medium either DPS or DNG.

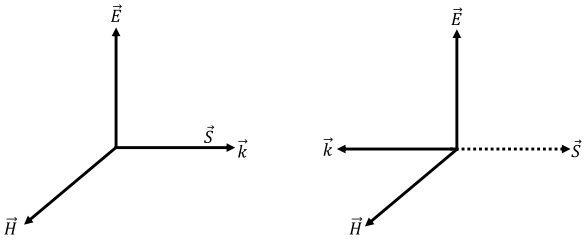

a) b)

Figure 4. Forward and reverse propagation of waves

a) forward propagating wave b) reverse propagating wave

One of the important features of DNG medium is the propagation of incident rays, the propagation of incident rays are at the same side of normal. According to the Snell's law it can be clarified as given in Eqn. 43.

$$n_1 \sin\theta_1 = n_2 \sin\theta_2 \quad (43)$$

Where: n_1 and n_2 are the indices of refractions of the medium 1 and 2, respectively, and θ_1 and θ_2 are the angles of incident and refracted rays. On metamaterials with both negative electrical permittivity and magnetic permeability, the incident ray and the refracted ray are at the same side, thus metamaterials have negative refractive index as given in Eq. 44.

$$n = -\sqrt{\varepsilon\mu} \quad (44)$$

The first experimental DNG material was developed by the D. R. Smith and his collaborators (Smith et al., 2000), they created a composited medium with simultaneously negative values of effective permeability and effective permittivity. A redrawing of designed structure is shown in Fig. 5.

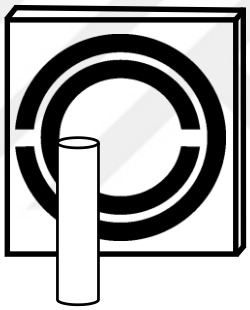

Figure 5. The proposed design of Smith's DNG metamaterial (Source: Smith et al., 2000).

Shortly after this design, another important design of a DNG material was developed by the Shelby, D. R. Smith, and S. Schultz in 2001 (Shelby et al., 2001).

2.3. Metamaterial-based Absorbers (MMA)

Absorbers that are employed as metamaterials with an appropriate effective permeability and permittivity are frequently called as metamaterial-based absorbers, metamaterial perfect absorbers (MPAs), metamaterial-based absorbers (MMA). As previously mentioned the first experimentally verified metamaterial perfect absorber is developed by the Landy and collaborators (Landy et al., 2008). The developed design was based on the principle of impedance matching of free-space, complex electrical permittivity, and magnetic permeability. According to the Landy's work the

effective medium of metamaterials is characterized by a complex permittivity and magnetic permeability as given in Eqns. 45-46.

$$\varepsilon(\omega) = \varepsilon_1 + i\varepsilon_2 \tag{45}$$

$$\mu(\omega) = \mu_1 + i\mu_2 \tag{46}$$

Where ε_1 and μ_1 correspond to the real parts and ε_2 and μ_2 correspond to the imaginary parts, these imaginary parts define to the dielectric losses of energies, and they are allowing for high absorption by minimizing the wave reflection and transmission. The developed absorber consists of the electric ring resonator (ERR) and exhibits a narrow-band absorption in the microwave region. Landy stated that it is possible to tune the magnetic response of a structure by tuning the geometry of cut wires. According the first metamaterial perfect absorber study, the metamaterials can achieve absorption by minimizing the reflection using the equalization of the impedance of the structure and that of the free-space as stated in Eq. 47.

$$Z = \sqrt{\mu/\varepsilon} = 1 \tag{47}$$

The MPA structure consists of three layers, on the top of the structure a metallic geometric pattern or patch design which is periodically arranged to create a resonance, then a dielectric material with a proper thickness, and on the bottom a continuous metallic plate or what is called the ground plane.

The dielectric material or the dielectric substrate of the design plays a crucial role in the MPAs. The substrate thickness should provide enough thickness to absorb the electromagnetic waves inside the structure while the dielectric constant and imaginary parts of the permittivity and permeability are responsible for the required absorption to reach appropriate values.

The top layer of the structure which is consisting of periodically arranged metallic elements is responsible to provide the Ohmic losses for an effective medium that matches the impedance of the free-space and thus to minimize the reflection and yields to the absorption of electromagnetic waves into the substrate. The absorbed electromagnetic waves from the periodically organized metallic parts of special geometries on the substrate part of the absorber now prevent the reflection of

electromagnetic waves in the structure with their proper imaginary parts of permittivity and permeability. Finally, the ground plane which consists of continuous metal is preventing the transmission of the absorbed electromagnetic waves from the structure.

The absorption rate is related to the reflection and transmission coefficients as given by Eq. 48. The absorption rate $A(\omega)$ is computed as:

$$A(\omega) = 1 - R(\omega) - T(\omega) = 1 - |S_{11}|^2 - |S_{21}|^2 \quad (48)$$

Where, $R(\omega = |S_{11}|^2)$ and $T(\omega = |S_{21}|^2)$ represent the reflection and transmission coefficients. If the reflection coefficient and transmission coefficient are equal to zero, the absorption rate will be equal to 100%.

2.4. S-Parameters

The S-matrix or S-parameters are the important tool to understand the characteristics of electromagnetic, and the RF components or the N-port network system elements. The abbreviation of the letter "S" has been derived from the word "*scattering"*. According to F. Caspers, for high frequency applications, the description of network characteristics in terms of electromagnetic fields are more useful instead of voltages or currents (Caspers, 2012).

The electromagnetic waves going into n^{th}-port are a= (a_1, a_2, …, a_n), and the waves travelling away from the m^{th}-port system are termed as b= (b_1, b_2, …, b_m). By the definition, currents going into the n^{th}-port are counted as positively and currents flowing out of the m^{th}-ports are negatively. The relation between a_n and b_m is given in Eqns. 49-50 (for two-port network; see Fig. 6).

$$b_1 = S_{11}a_1 + S_{12}a_2 \quad (49)$$

$$b_2 = S_{21}a_1 + S_{22}a_2 \quad (50)$$

Where: S_{11} is the return losses at port 1 of the network which is terminated by a matched load of a_2=0. S_{21} is the forward transmission coefficient (from port 1 to port 2), S_{12} is the reverse transmission coefficient from (port 2 to port 1) and the S_{22} is the output reflection coefficient at port 2. The equation of the reflection coefficient at port 1 is given in Eqn. 51.

$$S_{11=\frac{b_1}{a_1}}\Big|_{a_{2=0}} = \Gamma = \frac{Z_L - Z_0}{Z_L + Z_0} \tag{51}$$

Where, Γ is the input reflection coefficient and Z_L indicates that impedance of the load, Z_0 is the characteristic impedance. All ports of the n-port system must be terminated by matched loads.

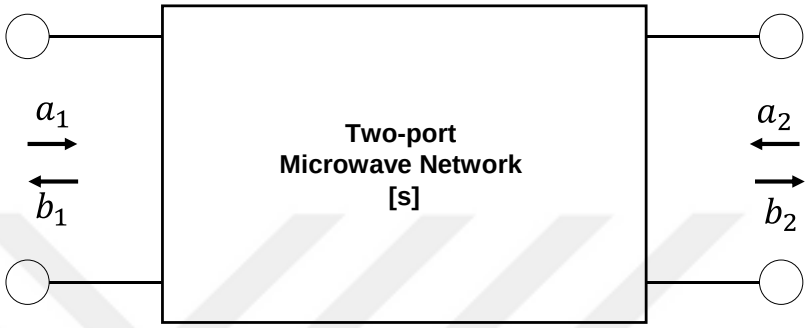

Figure 6. Two-port microwave network.

The scattering matrix of the two-port microwave network is given in Fig. 6, and the relations between the scattering parameters and the scattering matrix is also given in Eqns. 52-56.

$$S_{11=\frac{b_1}{a_1}}\Big|_{a_{2=0}} \tag{52}$$

$$S_{12=\frac{b_1}{a_2}}\Big|_{a_{1=0}} \tag{53}$$

$$S_{21=\frac{b_2}{a_1}}\Big|_{a_{2=0}} \tag{54}$$

$$S_{22=\frac{b_2}{a_2}}\Big|_{a_{1=0}} \tag{55}$$

$$\begin{bmatrix} b_1 \\ b_2 \end{bmatrix} = \begin{bmatrix} S_{11} & S_{12} \\ S_{21} & S_{22} \end{bmatrix} \begin{bmatrix} a_1 \\ a_2 \end{bmatrix} \tag{56}$$

As previously mentioned, the voltages and currents cannot be measured directly at the microwave frequencies or at higher frequencies. The complex amplitude

of the incident and reflected waves can be measured by the usage of vector network analyzer (VNA). The fundamental characteristics of the device under test (DUT) are usually analyzed by well-calibrated S-parameter measurements, the importance of the calibration methods in removing the systematic measurement errors (Root *et al.*, 2013). The analyzed DUT properties are include but not limited to gain, reflection coefficient, transmission coefficient, absorption rate, directivity, noise, voltage standing wave ratio (VSWR).

2.5. Numerical Methods

Many standard numerical methods can be employed in the determination of solutions of the electromagnetic problems, but the proper method should be chosen as some methods may lead to huge computations times, systematic numerical errors, or to incorrect results. Three main standard methods are prevailing the others, and most of the commercial electromagnetic solvers are built on these three methods. These methods are namely, the Finite Different Time Domain (FDTD), Finite Element Method (FEM), and the Finite Integral Technique (FIT).

2.5.1. Finite Difference Time Domain (FDTD) Method

The trace of this method goes back to 1966, a study by Kane Yee who developed algorithm for isotropic and nondispersive medium (Yee, 1966). The first acronym of the FDTD comes from a paper of Allen Taflove (Taflove, 1980). On the same side Yee's developed a FDTD based algorithm to compute both the electric and the magnetic fields in time and space domain using the Maxwell's curl equations (Sevgi, 2014).

The algorithm developed by Yee (Yee, 1966) points out that when an object encounters an obstacle, the incident wave will be scattered. The formulation of the scattering decomposed in two-way transverse electric and transverse magnetic fields as given in Eqns. 57-58.

For a transverse electric wave (TE): $H_x = H_y = 0$, $E_z = 0$.

$$-\mu\frac{\partial H_z}{\partial t}=\frac{\partial E_y}{\partial x}-\frac{\partial E_x}{\partial y},\ \varepsilon\frac{\partial H_z}{\partial y}=\frac{\partial E_x}{\partial t},\ -\frac{\partial H_z}{\partial x}=\varepsilon\frac{\partial E_y}{\partial t} \quad (57)$$

For a transverse magnetic wave (TM): $E_x = E_y = 0$, $H_z = 0$.

$$\varepsilon\frac{\partial E_z}{\partial t}=\frac{\partial H_y}{\partial x}-\frac{\partial H_x}{\partial y},\ \mu\frac{\partial H_x}{\partial t}=-\frac{\partial E_z}{\partial y},\quad \mu\frac{\partial H_y}{\partial t}=\frac{\partial E_z}{\partial x} \quad (58)$$

2.5.2. Finite Element Method (FEM)

The history of the finite element method goes back to 1943, a study by Courant (Courant, 1943) was needed to solve the structural mechanics problem. This method was numerically based on solving the differential equations which emerged in the engineering and mathematical modeling from aerospace, electrical, and mechanical engineering. The equations were partial differential equations in two or three space boundaries. FEM decomposes the large components into many elements, the structure was divided into many pieces termed as mesh points. The applications of FEM comprise fluids dynamics, solid mechanics, electrostatic problems, heat problems, and electromagnetism.

2.5.3. Finite Integration Technique (FIT)

The first introduction of the finite integration technique was introduced by Weiland in 1977 (Weiland, 1977), where Maxwell's equations were applied in integral form for solving the electrodynamics problems (Weiland, 1977), (Marklein, 2002). To simulate real-world electromagnetic field problems with complex geometries, this technique is considering all the six vector components of electric field strength and magnetic flux density on the entire system (Clemens and Weiland, 2001).

2.6. Materials and Methodology

Within the scope of this thesis, the developments and simulations of novel PCB and textile-based metamaterial absorbers were achieved using the CST Microwave (MW) Studio. The numerical plane-wave simulations of the designs were processed

using the CST Studio's finite integral technique (FIT) on the frequency domain. The proposed absorbers' scattering parameters and absorptivity rates were computed for each designed absorbers' unit cell structure.

In the proposed absorber designs the dielectric losses of the materials and the dielectric constant of the dielectric materials were considered, and the geometry optimizations were done with respect to these parameters. Furthermore, the proposed unit cells developed after a vast number of plane-wave simulations, a research and development process and many parametric studies.

The following steps were followed during the design process of this thesis:

1) Deep research about metamaterials and metamaterial-based electromagnetic wave absorbers was done.

2) Identifying the insufficiencies and the still not explored new fields which are still open to improvement in this area of electromagnetic wave absorbers.

3) After the determination of insufficiencies, the goals of the current research were set to achieve.

4) To develop a metamaterial-based absorber data sheets of the available PCB standards were analyzed, and the best fitting materials were chosen to use in the current plane-wave simulations.

5) Novel unit cells were developed with the help of the 3-D computer aided design (CAD) tools in the used CST simulation program.

6) The developed designs were simulated in the true boundary conditions, global mesh settings and domains.

7) According to the instructive output of scattering parameters, the generated designs were optimized with a help of many geometrical parametrical studies.

8) After reaching the final optimized design, different parametric studies were conducted on the unit cell of the developed absorbers such as examining their responses to different oblique incidence angles and analyzing the impacts of various real-time conditions.

9) Enhancement of the final design with respect to the real-time condition necessities.

10) Preparing of the unit cell for the fabrication process, the fabrication of the developed design with lithography method.

11) Calibration of the VNA to prevent systematic errors, and measurements of the absorber's reflection coefficient were taken to examine the performance of the fabricated absorber in comparison to the designed one.

CHAPTER 3: RESULTS AND DISCUSSION

Summary: In this chapter, wideband, ultra-wideband and wide-angle metamaterial-based absorbers are developed. They are explained following the order of publication. According to the obtained findings, the absorption behaviors of the developed metamaterial absorbers were investigated and their responses at different real-time scenarios were examined. The designed structures of metamaterial absorbers were investigated in term of the bandwidth, thickness of substrates, size, the response to various incident angles, geometries, and absorption rates.

3.1. PCB-Based A Novel 5G Wideband Metamaterial Based Absorber for Microwave Energy Harvesting Applications

Summary: This study presents a novel unit cell design of compact, thin, and wideband metamaterial-based absorber (MMA). It is targeted for microwave energy harvesting and for 5G applications. To achieve perfect absorption rates over a broad band, the unit cell is attentively designed and optimized with proper physical and geometrical configurations.

The structure of this study is as follows:

1) Developing a unit cell of the proposed absorber

2) Parametric studies

3) Simulation and performance analysis

4) Effect of incident angles

3.1.1. Unit Cell of Proposed "G&S" Absorber

In this part, the suggested MMA's unit cell is presented with the design geometry, design parameters, and with the physical properties. To achieve maximum

electromagnetic wave absorption rates, the unit cell of this MMA should be perfectly matched with the impedance of free space as abovementioned. The computations of the reflection coefficients and absorption rates are done according to the Eq. 48.

The design of this unit cell consists of three-layers, a special geometry of patch structure and a ground layer from copper with a thickness of 0.035 mm and with conductivity value of 5.96 x 10^7 S/m. A substrate layer is placed between the patch and the ground layers.

In this study, two different substrates were considered, and their physical properties are given as following: (1) FR-4 with thickness of 1.2 mm, with a relative dielectric constant of $\varepsilon_r = 4.4$, and dielectric loss tangent of tanδ=0.02. (2) Rogers RT5880 substrate have the thickness of 1.575 mm, the relative dielectric constant of $\varepsilon_r = 2.2$ with a dielectric loss tangent of tanδ= 0.0009. The unit cell of this study is given in Fig. 7 and the design parameters are given in Table 1.

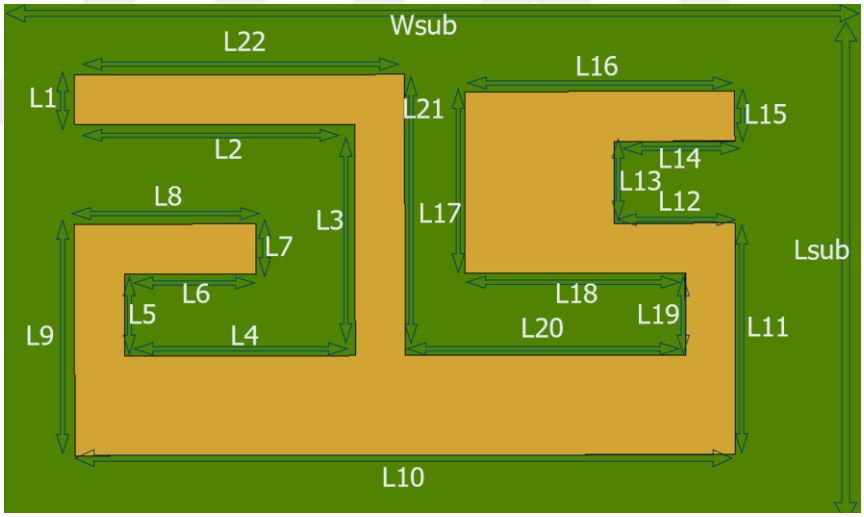

Figure 7. The proposed G&S MMA design with the design parameters.

Table 1. A parameter values of the proposed G&S MMA.

Parameters	**L_1**	**L_2**	**L_3**	**L_4**	**L_5**
Value (mm)	0.2585	1.4605	1.2020	1.2020	0.4265
Parameters	**L_6**	**L_7**	**L_8**	**L_9**	**L_{10}**

Table 1 (continued)

Value (mm)	0.6850	0.2585	0.9435	1.2020	3.4381
Parameters	**L_{11}**	**L_{12}**	**L_{13}**	**L_{14}**	**L_{15}**
Value (mm)	1.2020	0.6290	0.4265	0.6290	0.2585
Parameters	**L_{16}**	**L_{17}**	**L_{18}**	**L_{19}**	**L_{20}**
Value (mm)	1.4045	0.9435	1.1460	0.4265	1.4605
Parameters	**L_{21}**	**L_{22}**	**W_{sub}**	**L_{sub}**	**H_{sub}**
Value (mm)	1.4605	1.7190	4.5403	2.7713	1.575

As shown above, the overall unit cell size of the proposed absorber is 4.5403 x 2.7713 mm. The novel geometry of the patch arises from two different letters G & S.

3.1.2. Parametric Studies of G&S MMA

Numerous parametric simulations were conducted to design the wideband MMA with a compact, thin and single-layer low profile absorber. Additionally, the study of different PCB-based dielectric materials was also important to analyze the effect of lower dielectric losses in the design phase of the MMA.

In this part of study, the simulation results of parametric studies and the impacts of the dielectric losses are showed.

The trace width of copper and other parts of the proposed geometry required over numerous simulations to achieve final design. The best results in term of absorption rates and minimized return losses were achieved with value of the parameters L7 = L15 = W.

The best result is chosen by considering the reflection coefficient, bandwidth, peak absorption, and the average absorption rate. As given in Figs. 8 (a & b), the final optimized design is achieved with the value of W=0.2585 mm.

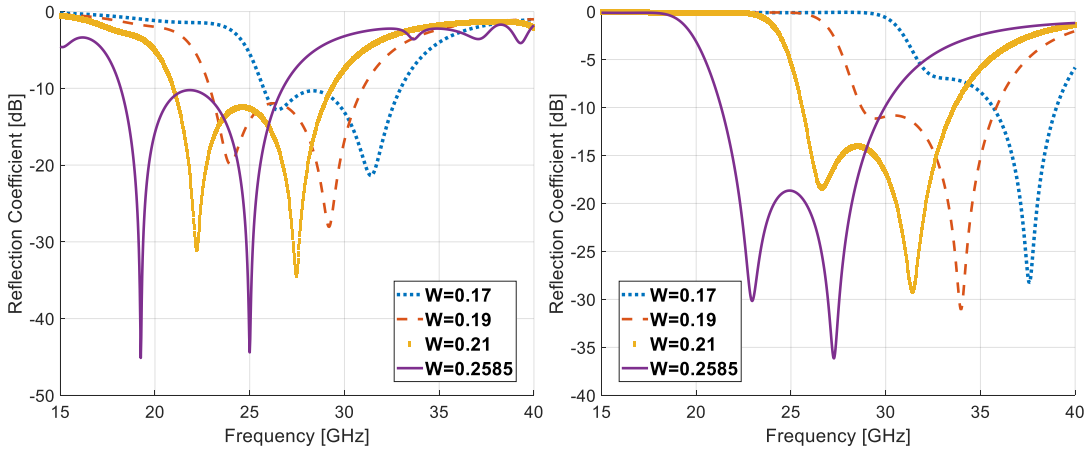

Figure 8. The reflection coefficient of parametric study on the "W" parameter a) FR-4 b) Rogers RT5880

After achieving and optimized value of W = 0.2585, the optimization process of this study continued for both the Rogers RT5880 and FR-4 materials to obtain a wide bandwidth and high absorptivity rates behaviors.

3.1.3. Simulation and Performance Analysis of G&S MMA

The numerical plane-wave simulations of the current design showed that after plentiful studies of the unit cell of this structure is achieved, the perfect impedance match with the impedance of free-space can be achieved. The operation frequencies of the proposed absorber indicate that, the spectrum is fitting very well for the 5G and microwave energy harvesting applications. The final results of the reflection coefficients and absorption rates of both the FR-4 and Rogers RT5880 materials are given below. It can be noted that the MMA has wideband feature both in the two considered dielectric materials as shown in Figs. 8&9. The dielectric material FR-4 offers a wide bandwidth between 18.00 GHz and 26.8 GHz with an average of 96% absorption rates. The Rogers RT5880 substrate offers operation frequencies from 21 GHz to 30 GHz with close to the perfect absorption rates due to the lower dielectric losses.

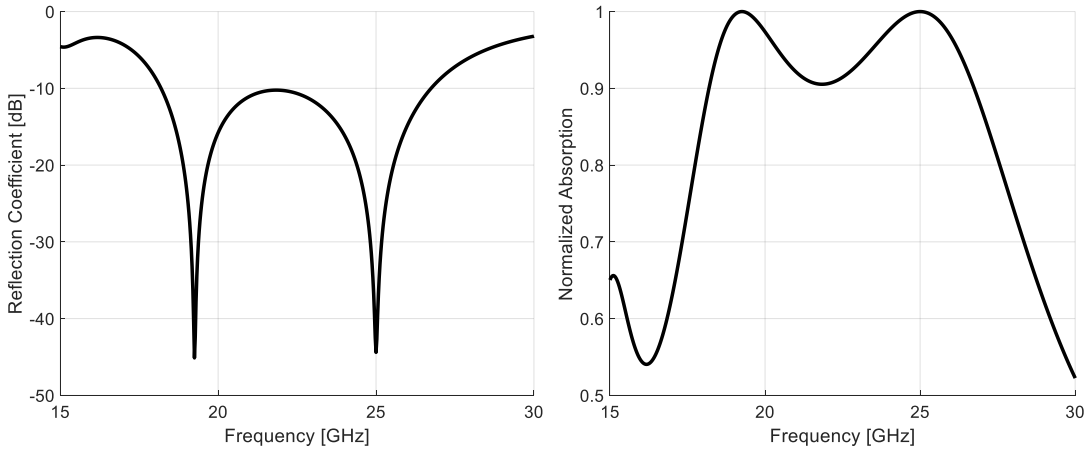

a) b)

Figure 9. The reflection coefficients and normalized absorption rates of FR-4 a) reflection coefficients b) normalized absorption rates

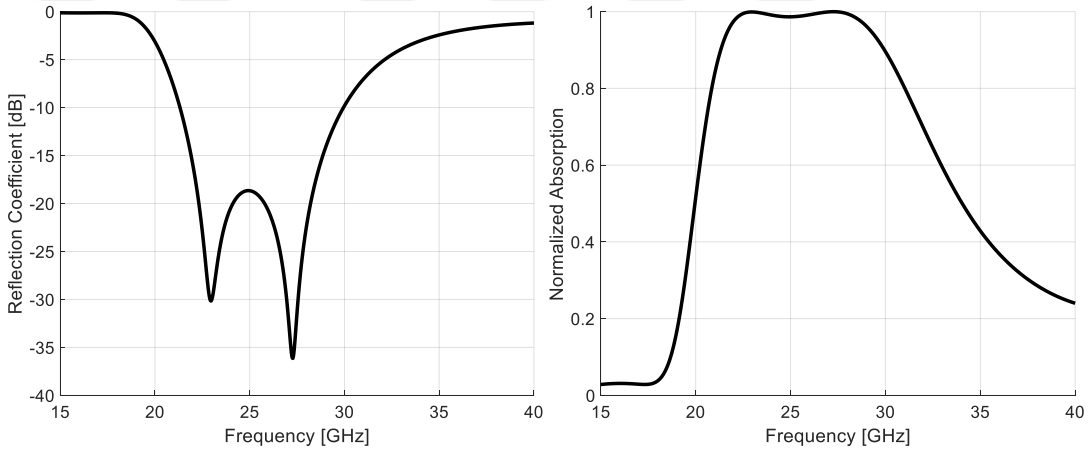

a) b)

Figure 10. The reflection coefficients and normalized absorptions of Rogers RT5880 a) reflection coefficients b) normalized absorption rates

A comparison of both the FR-4 and Rogers RT5580 dielectric materials is given in Table 2.

Table 2. The comparison of Rogers RT5880 and FR-4 in terms of the absorptivity rate and fractional bandwidth.

Material Type	**Frequency Range**	**Absorption Fractional Bandwidth**	**Absorptivity (%)**	**Unit Cell Size (mm^3)**
FR-4	18-26 GHz	36.4 %	≈ 96	4.5 x 2.7 x 1.2
RT 5880	21-30 GHz	35.3 %	≈ 99	4.5 x 2.7 x 1.2

As seen from Table 2, the Rogers RT5880 provides near to perfect absorption rates, on the other hand despite the high dielectric losses, the FR-4 dielectric offers slightly higher fractional bandwidth with an average of 96% absorption rate.

3.1.4. Effects of Incident Angles on G&S MMA

In MMAs, the response of the designed absorbers to different angles of incidence are very crucial for different applications based on electromagnetic waves coming with different angles to the MMA. So, the designed absorber needs to persist a stable absorptivity for different angles of incidence over the whole absorption bandwidth.

To understand whether the designed MMA has a stable absorptivity at different angles of incidence, parametric studies were conducted in the range of θ=0°-30°.

As it clearly seen from Figs. 10&11 that the designed unit cell regardless of dielectric material offers a stable absorption bandwidth for both FR-4 and Rogers RT5880.

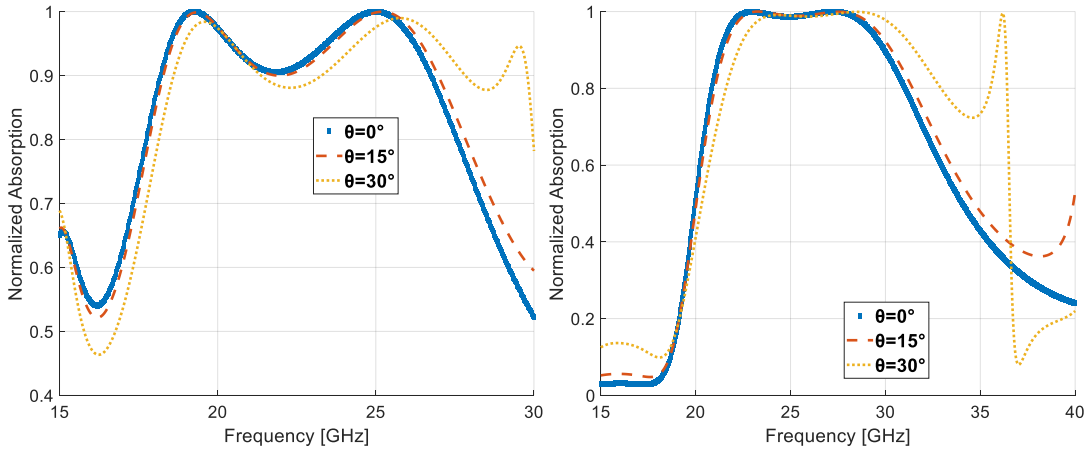

a) b)

Figure 11. The normalized absorption rates of dielectric materials on incident angle 0°-15°-30° a) FR-4 b) Rogers RT5880

The absorptivity rates of the proposed MMA stays higher than 99% in Rogers RT5880 with minor right-handed shift after above 30°. The common bandwidth of Rogers RT5580 is about 7.7 GHz for the angle of incidences in the range 0°-30°, it is important to note that this is a significant result for development of the wide-angle MMA. Furthermore, in the FR-4 dielectric material, the absorptivity rate stays higher than 94% with minor right-handed shift and minor decrease in the absorption rate. At the same time, the FR-4 has common bandwidth of 8.1 GHz, which is a promising step for the development of wide-angle MMAs. The proposed structure preserved most of the offered absorption rates and bandwidth under different oblique incident angles.

As shown in Table 3, the average absorptivity rate is computed for θ=0, 15, and 30 degrees and Rogers RT5880 is chosen for the comparison with other suggested previous studies.

Table 3. A comparison of the proposed G&S design in terms of the incident angles, absorption bandwidth and unit cell size with related previous studies.

Frequency Range	**Fractional Absorption Bandwidth**	**Absorptivity (%)**	**Unit Cell Size (mm^3)**	**References**
10.6 - 16.6 GHz	44.11 %	≈ 85 ≈ 71 ≈ 77	7.0 x 7.0 x 1.6	(Ramya and Srinivasa Rao, 2017)

Table 3 (continued)

15.7 - 23.8 GHz	41.01 %	≈ 90 ≈ 75 ≈ 30	7.0 x 7.0 x 1.6	(Khanna and Awasthi, 2020)
21 – 30 GHz	35.3 %	≈ 99 ≈ 96 ≈ 94	4.5 x 2.7 x 1.575	Our Proposed Structure

It is apparent that, the proposed structure has higher absorptivity rate, thinner and more compact compared to other previous studies, however the fractional bandwidth is slightly lower than others.

3.1.5. Conclusion of G&S MMA

In this study, a novel wideband metamaterial absorber is developed with perfect absorption rates for 5G and electromagnetic wave harvesting applications. The designed unit cell is achieved with the combination of optimized letter-shaped patches (G&S). The response of the developed design to different angles of incidence clearly indicate that it is suitable for angles in the range θ=0-30 degrees. The proposed design has stable absorption rates higher than (on the average) of 96% for FR-4 and about 99% for Rogers RT5880 substrate. The obtained results of this study claims that the development of single-layer wideband MMA can be achieved without the bulky, bigger and heavy structures.

3.2. PCB-Based Multiband Double-Layered Metamaterial Based Perfect Absorber for Microwave Energy Harvesting Applications

Summary: The purpose of this study is to propose a new design of a double-layered perfect MMA with triple-band for harvesting of electromagnetic energies for 5G applications.

In this study, a double-layer, triple-band, metamaterial-based perfect absorber design with high absorption rates was developed by using the broadband metamaterial-based perfect absorber unit cell design we previously developed. This study is unlike our previous studies, it has a multi-band structure, multi-layer architecture and the possibility of working at high frequencies. The obtained design in this study operates as a triple-band MMA between 26 GHz and 42 GHz operating frequencies. This operating range covers the upper frequency range of the 5G frequency spectrum. Since the developed design has a very high absorption rate, it is extremely suitable for 5G and mm-Wave energy harvesting applications.

The developed structure of this study is summarized as follows:

1) The proposed double-layer of MMA Unit Cell.

2) The simulation results and performance analysis of MMA

3) Conclusion.

3.2.1. Proposed unit Cell of Double-layered MMA

The aim of this study is to develop a novel multi-band, double-layer metamaterial-based perfect absorber design for 5G and RF energy harvesting applications. To achieve perfect metamaterial absorber with a multi-band feature the design of the double unit cell is projected. the design of the proposed double-layer unit cell computed and the spacing between these two layers are calculated according to following.

The design of this structure consists of two layers, the first layer consists of ungrounded substrate on the bottom of the previously developed patch and the other layer consists of a grounded substrate with the same geometry. In addition to this, the spacing between these two layers is calculated according to Eq. 59.

$$\lambda = \frac{c}{f\sqrt{\varepsilon_r}} \tag{59}$$

Where: the wavelength λ is computed using ε_r= 2.2 and f = 30 GHz.

Figure 12. The proposed double-layer MMA.

The design parameter values of the unit cell are given in Fig. 7 and listed in Table 1, also the double-layered structure is illustrated in Fig. 12. The bottom layer of the first body, namely the ground and the top layer is the patch which is made of 0.035 mm thick copper with a conductivity of 5.96 x 10^7 S/m. The substrate height of ROGERS RT5880 (dielectric constant ε_r= 2.2 and loss tangent value tan δ = 0.009) is about 1.575 mm.

3.2.2. Simulation and Performance Analysis of Double-layered MMA

The results of single unit cell metamaterial-based perfect absorber which we previously developed shows a single band characteristic as indicated in Fig. 9. As can be seen in Fig. 13, the double-layered MMA developed on the dielectric material Rogers RT5880 has a triple band feature and a high absorption rate in the operating frequencies range from 26 GHz to 42 GHz.

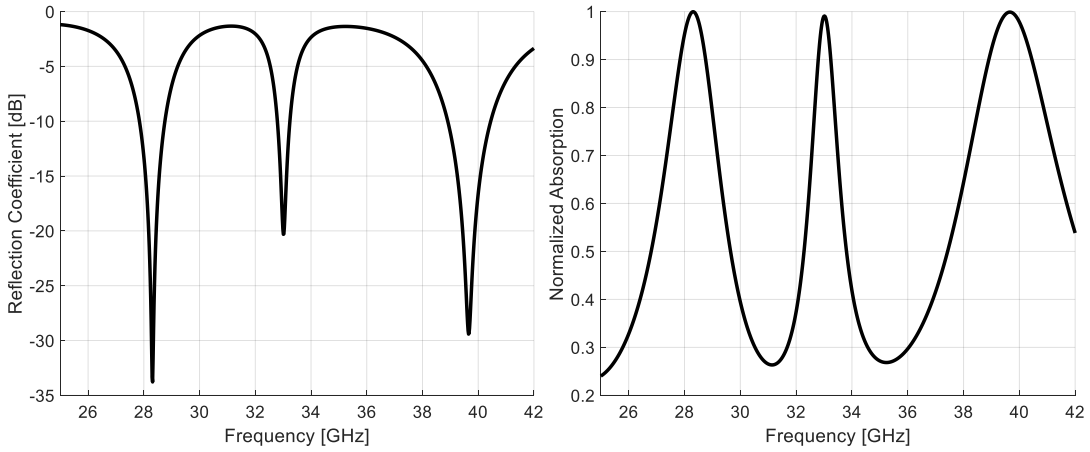

a) b)

Figure 13. The reflection coefficient and normalized absorption of double-layered MMA with spacing λ/2 = 3.371 a) reflection coefficient b) normalized absorption

According to the parametric studies carried out to find the most optimized parameters of this design, it was observed that λ/2 (3.371 mm) spacing gave better results than λ (6.672 mm) spacing, and these optimized results are given in Fig. 13.

Table 4. A comparison of the proposed double-layer design in terms of the incident angles, absorption bandwidth and unit cell size with related previous studies.

Frequency Range (GHz)	**Absorption (%)**	**Absorption Fractional Bandwidth**	**Unit Cell Size (mm^3)**	**References**
23.1 – 24.1	≈ 96	4.23 %	6 x 6 x 0.2	(Jeong *et al.*, 2016)
24.62- 26.15	≈ 93.5	6.02 %	10 x 10 x 1.58	(Hannan *et al.*, 2019)
36-36.8	≈ 90	2.20 %	13 x 13 x 1.5	(Singh *et al.*, 2018)
27.84 - 28.76 32.80 - 33.24 38.90 - 40.45	≈ 99	3.25 % 1.33 % 3.91 %	4.5 x 2.7 x 1.575	This MMA

A comparison of the previously developed metamaterial-based absorbers and our proposed absorber was done as shown in the Table 4. The currently developed

MMA has high absorptivity rates with a triple-band behavior, and the unit cell is more compact in comparison to other studies.

3.2.3. Conclusion of Double-layered MMA

This study was mainly focused on the development of multiband metamaterial absorber for 5G and mm-wave applications. The designed double-layered MMA has triple-band properties over a wide frequency range, and it is well applicable to 5G and RF energy harvesting applications owing to its high absorption rates. According to the obtained simulation results, the suggested double-layered MMA design has extremely high absorption rates of up to 99.98% for optimized spacing of $\lambda/2$= 3.371 mm.

3.3. Development of Ultra-Wideband Textile-Based Metamaterial Absorber for mm-wave Band Applications

Summary: This study introduces a state-of-the-art textile-based ultra-wideband metamaterial absorber for wearable smart applications. The unit cell geometry of this design was previously suggested for PCB-based energy harvesting applications, but in this study, we optimize the same unit cell on the textile-based fabric dielectric materials. The textile-based fabrics and the traditional rigid counterparts are compared in terms of bandwidth and absorption rates.

As a main focus of textile-based MMA, this work mainly focused on real-time scenarios of flexible textile properties such as bending conditions and the possibilities of facing incident waves with different angles of incidence as a result of bending. The outcome of this work shows that the designed and developed structure is favorable for smart-textile applications on mm-Wave.

The development process followed in this study is summarized as follows:

1) Proposed Textile-based G&S MMA Unit Cell

2) Comparison between PCB and Textile-based substrates

3) The effect of substrate thickness on the absorption coefficient

4) Observation of different textile-based dielectric materials

5) Effects of incident angle on the absorption rates

6) Investigate bending condition of proposed MMA for real-time scenarios

3.3.1. Unit Cell of Textile-based G&S MMA

In this part, the previously developed MMA unit cell is applied to the textile-based Felt fabric dielectric material with a relative permittivity ε_r= 1.22, dielectric loss tangent tan δ = 0.009, thermal conductivity of 0.05 W/m.K and thickness of 1.0 mm. The copper material on the ground and the patch both have a thickness of 0.035 mm with conductivity of 5.96 x 10^7 S/m. The proposed textile-based fabric design and the parameter values of the design are given in Fig. 14 and Table. 5, respectively.

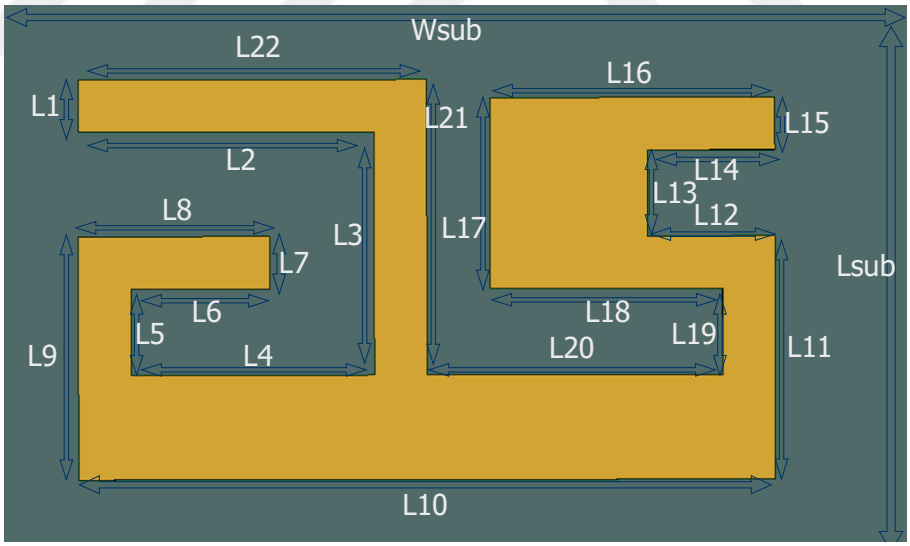

Figure 14. The proposed textile-based G&S MMA with design parameters.

Table 5. Design parameter values of the proposed textile-based G&S MMA.

Parameters	**L_1**	**L_2**	**L_3**	**L_4**	**L_5**
Value (mm)	0.2585	1.4605	1.2020	1.2020	0.4265
Parameters	**L_6**	**L_7**	**L_8**	**L_9**	**L_{10}**
Value (mm)	0.6850	0.2585	0.9435	1.2020	3.4381
Parameters	**L_{11}**	**L_{12}**	**L_{13}**	**L_{14}**	**L_{15}**
Value (mm)	1.2020	0.6290	0.4265	0.6290	0.2585
Parameters	**L_{16}**	**L_{17}**	**L_{18}**	**L_{19}**	**L_{20}**
Value (mm)	1.4045	0.9435	1.1460	0.4265	1.4605
Parameters	**L_{21}**	**L_{22}**	**W_{sub}**	**L_{sub}**	**H_{sub}**
Value (mm)	1.4605	1.7190	4.5403	2.7713	1.0000

3.3.2. Parametric Studies of Textile-based MMA

To investigate the behaviors of the suggested MMA under different conditions and to make a comparison between the PCB and textile-based dielectric materials, several parametric studies were conducted based on finite-integration-technique (FIT) plane-wave simulations. The comparison between the PCB and the textile-based simulations were done in the final optimized parameters. As previously mentioned, the structure itself is optimized but the thicknesses of the PCB-based dielectrics are different for FR-4 and Rogers RT5880 which are the 1.2mm, 1.575 mm, respectively. On the other hand, the Felt dielectric has about 1.0 mm thickness. The physical properties of the used dielectric materials in this comparison are given in Table 6.

Table 6. Physical properties of FR-4, Rogers RT5880, Felt substrates.

Material Type	**Dielectric Constant**	**Tangent Loss**	**Thermal Conductivity (W/m.K)**
FR-4	4.3	0.02	0.025
Rogers RT5880	1.7	0.0009	0.020
FELT	1.22	0.0016	0.050

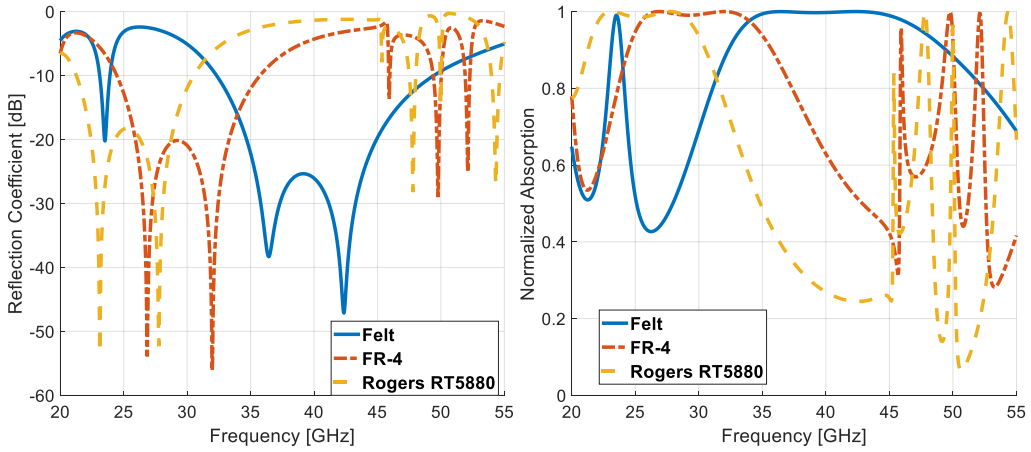

a) b)

Figure 15. A comparison between a textile-based material and counterparts PCBs a) reflection coefficient b) normalized absorption

The parametric studies of the MMA showed that the consideration of textile-based dielectric material offers an ultra-wideband property as demonstrated in Fig. 15. The textile-based Felt has the widest bandwidth compared to the rigid PCB-based substrates. The obtained fractional bandwidths of the three different dielectric materials are 36.4%, 35.30%, 41.87% for FR-4, Rogers RT5880 and Felt, respectively. It is clearly seen that; they are all offering wideband behaviors. The Felt fabric provides an ultra-wideband feature compared to other dielectrics. As stated in Table 7, the average absorption of 99 % is achieved with Rogers and Felt substrates and for a FR-4 an average of 96 % is achieved due to the higher dielectric losses of FR-4. But it is important to indicate that even the thin structure of Felt, the achieved absorption bandwidth of Felt is higher than others.

Table 7. A comparison of conventional PCB and textile-based substrates on the obtained absorptivity values in term of dimension and substrate thickness.

Material Type	**Frequency Range**	**Absorption Fractional Bandwidth**	**Absorptivity (%)**	**Unit Cell Size (mm^3)**
FR-4	18 - 26 GHz	36.40 %	≈ 96	4.5 x 2.7 x 1.2
RT5880	21 - 30 GHz	35.30 %	≈ 99	4.5 x 2.7 x 1.575
FELT	32.32 - 49.44 GHz	41.87 %	≈ 99	4.5 x 2.7 x 1.0

3.3.3. The effect of substrate thickness on the absorption coefficient

To investigate the effect of changing the dielectric thickness on the operation performance of the suggested design, parametric studies were done on the Felt fabric with different thicknesses, 1 mm, 2 mm, 3 mm, 4 mm. According to Fig. 16, the increase in thickness affects the absorption bandwidth while the resonance frequencies are shifting or diminishing. The increase of thickness from 1 mm to 2 mm exhibits left-handed shifting to the lower frequencies. For the increase of thickness from 2 mm to 3 mm decreases the bandwidth. Increasing of 3 mm to 4 mm exhibits a right-handed shifting to the higher frequencies.

It is important to highlight that the absorption rates are greatly affected by the thickness of the substrate as shown in Fig. 16 (b).

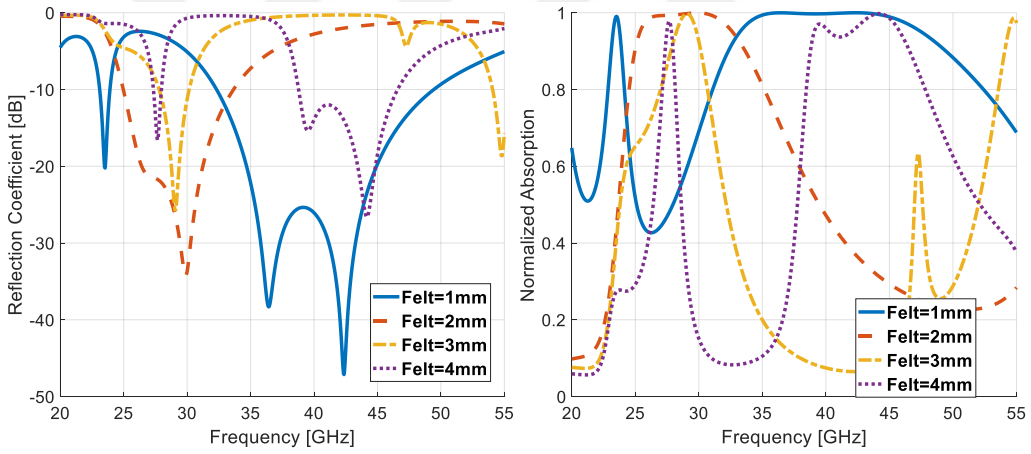

a) b)

Figure 16. The impact of the substrate thickness on textile-based G&S MMA
a) reflection coefficients b) normalized absorption rates

3.3.4. Absorptivity rates of different textile-based materials

In this part, the investigation of different textile-based dielectric materials is done to observe the effect of changing the dielectric constants and the physical properties of different materials on the reflection coefficients, bandwidths, and absorption rates.

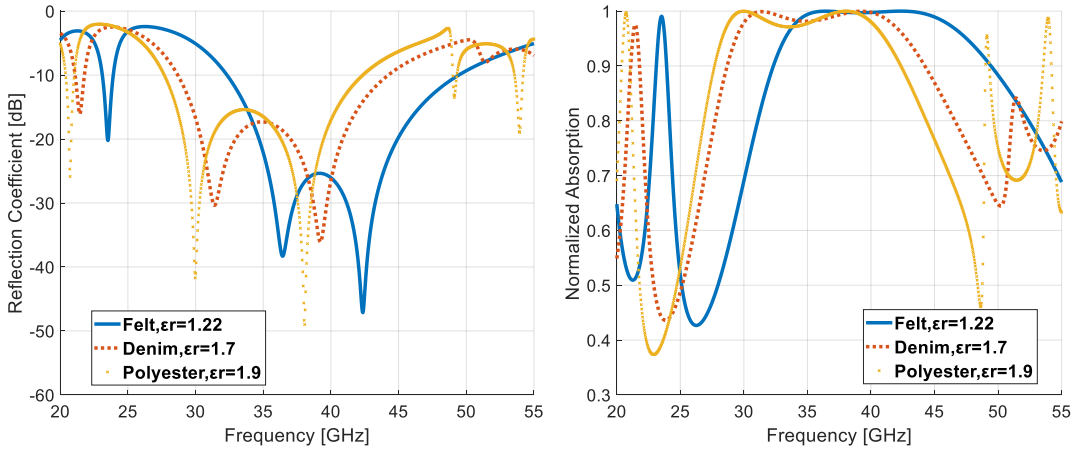

a) b)

Figure 17. The impact of the different dielectric material on textile-based G&S MMA a) reflection coefficients b) normalized absorption rates

As it can clearly see from Fig. 17, the felt fabric-based material shows the best bandwidth and absorption rate and the physical properties of textile-based materials were given in Table 8.

Table 8. Physical properties of textile-based substrates.

Textile Type	**Dielectric Constant**	**Tangent Loss**	**Thermal Conductivity (W/m.K)**
POLYESTER	1.9	0.0045	0.14
DENIM	1.7	0.025	0.050
FELT	1.22	0.016	0.050

The obtained result of this part shows that the dielectric constant affects the results of absorption. The material with the lowest dielectric constant offers the best absorption and peak absorption rate. The fractional bandwidth of three materials are 42.834%, 43.65%, 42.828% for Polyester, Denim and Felt, respectively.

3.3.5. Effect of incident angle on the absorption

The angle of incidences of waves falling on the MMA are crucial. In order to achieve stable absorptivity rates at different angle of incidences and in order to to determine the common absorption bandwidths, several parametric studies were conducted with the numerical plane-wave computations.

This part is deeply examining the response of the MMA at different angles of incidence, oblique angles range in the range of θ = 0°-15°-30° are considered. As shown below in Fig. 18, the increase of incident angles affects the reflection coefficients and average absorption rates.

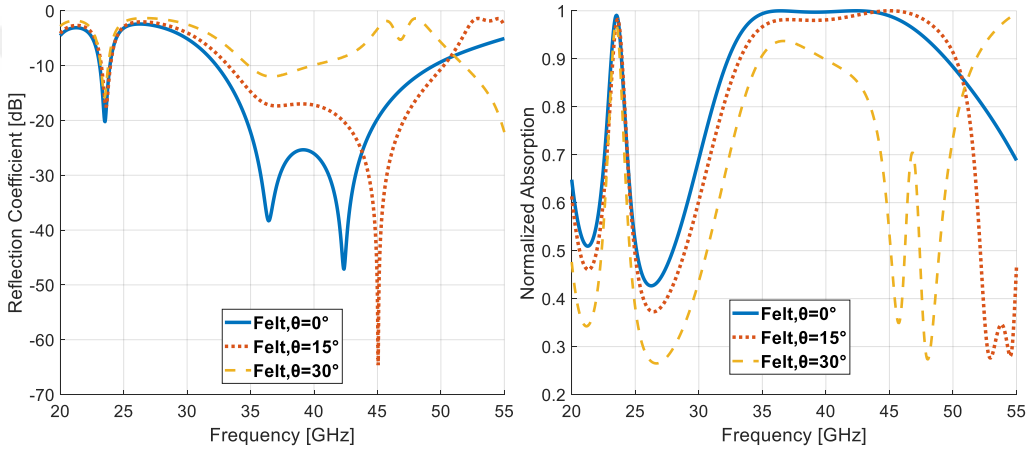

a) b)

Figure 18. The impacts of the incident angle on textile-based G&S MMA

a) reflection coefficients b) normalized absorption rates

For angles in the θ = 0-30 degrees, a common bandwidth of approximately 5 GHz is achieved with average absorptivity rate is about 95%. Conversely, the average absorption rate is about 99 % for an incident angle of θ = 0°.

3.3.6. Bending Effect

The consideration of textile-based dielectric material in this study offers an inevitable chance to investigate the bending conditions on the behavior of MMA, as the elasticity is one of the important advantages of the textile-based materials. The flexibility of the material could affect the absorption and impedance matching of

structure as well. To investigate the absorption mechanism and performance of absorption under different bending conditions, many numerical plane wave simulations were performed. With the task to have a stable flexible absorber, the proposed structure must preserve the performance of the absorptivity and absorption bandwidth under the different bending conditions.

To investigate these scenarios, many simulations were performed with cylindrical bending of radii 1 mm, 3 mm, 5 mm, 7 mm, 9 mm, 11 mm. The illustration of cylindrical bending process is illustrated in Fig. 19.

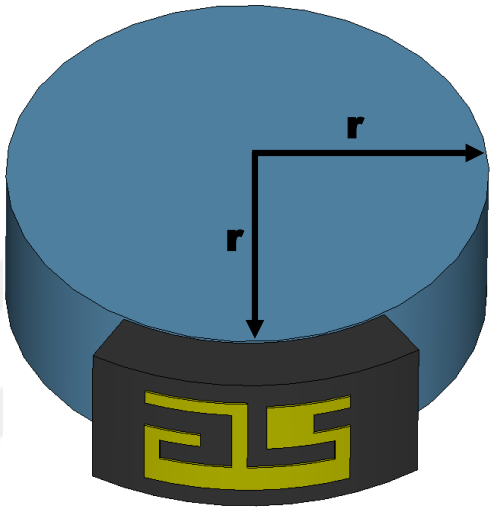

Figure 19. Illustration of the proposed textile-based G&S MMA with cylindrical bending.

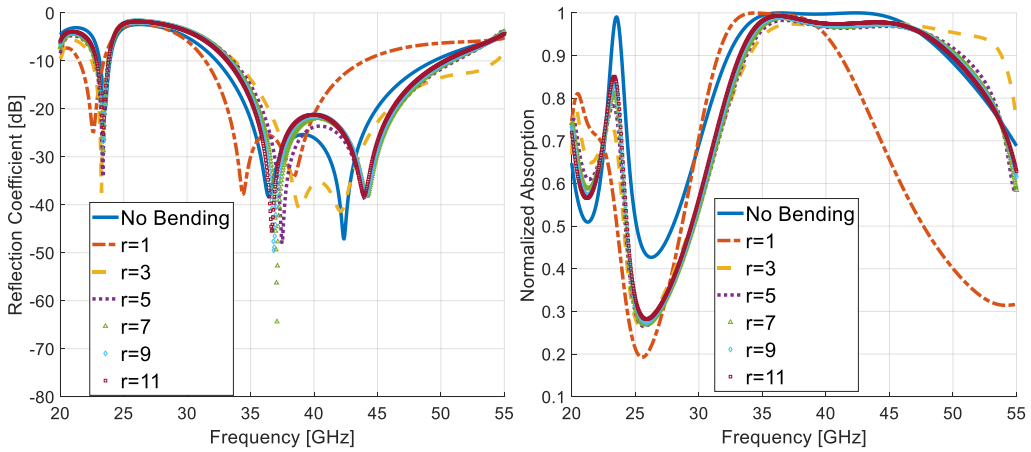

a) b)

Figure 20. The impacts of bending on the textile-based G&S MMA

a) reflection coefficients b) normalized absorption rates

As depicted in Fig. 20, under extreme bending conditions of the structure the MMA still preserves the peak, average absorption rates behaviors since the geometry of MMA is well matched. In the cylindrical bent with radii between 3-11 mm, there is a minor right-handed resonant frequency shift while for the radius of 1 mm a remarkable left-handed shift occurred. The best absorption rate and peak absorption is achieved with a flat structure. The decrease of bandwidth and absorption rates can be clarified by the impedance mismatching with free-space increases under different bending conditions. It should be noted that, twisting the structure results in more narrower bandwidths.

Table 9. A comparison with related previous studies of the textile-based flexible dielectric materials in terms of absorptivity values and absorption fractional bandwidths.

Material Type - Absorber Geometry	**Frequency Range**	**Absorption Fractional Bandwidth**	**Absorptivity (%)**	**Unit Cell Size (mm^3)**	**References**
FELT - SRR	9–10.5 GHz	15.43 %	≈ 90	30 x 30 x 1.0	(Tak and Choi, 2017)
FELT - SRR	4.9-5.06 GHz	3.21 %	≈ 99	18 x 18 x 2.0	(Bait-Suwailam *et al.*, 2019)
FELT	23.11-23.92 32.32-49.44 GHz	3.44 % & 42.828 %	≈ 99	4.5 x 2.7 x 1.0	Our MMA

To show that the currently designed MMA exhibits a state-of-the-art ultra-wideband textile-based MMA, a comparison with recent studies is done. The comparison study is depicted in Table 9. It can be shown that the current design is more compact in size and since it proposes 2.77 times wider bandwidth than the first study and 13.34 times wider than the second study, it is clear that has much wider and more compact than the other studies

3.3.7. Conclusion of Textile-based G&S MMA Design

In this study, the development of an ultra-wideband textile-based absorber achieved with employment of Felt substrate with a previously developed unit cell

geometry. The main aim of this work is developing a textile-based absorber for various mm-Wave applications. The obtained plane-wave simulation results show that the proposed MMA can work at different angles of incidence and bending conditions. *It is important to note that the use of different textile-based substrates allows the tenability and re-configurability of frequencies.* The achieved results indicate that our ultra-wideband textile-based absorbers are initial steps for the development of electronic based smart applications such as electromagnetic energy harvesting, smart health monitoring, smart textile-based sensor, and infrared of this.

3.4. A PCB-based Novel Ultra-Wideband Metamaterial-Based Perfect Absorber for 5G Millimeter-Wave Applications

Summary: This study presents a novel design of an ultra-thin, small-scale ultra-wideband MMA for 5G millimeter-wave applications. The generated unit cell is achieved by combining of two letters (H&S). The obtained simulations results show that the developed design offers an ultra-wideband MMA with low-profile, miniature structure.

The structure of this work is as follows:

1) Design of the unit cell of the proposed H&S MMA

2) Parametric Studies of the substrate thickness

3) Parametric Studies of Scaling On the role of the unit cell's side and Letter-shape patches

4) Simulations and performance analysis of the H&S MMA

5) Investigating the effects of incident angles on H&S MMA absorption coefficients

3.4.1. Unit Cell of Proposed H&S MMA

This work is mainly focused on the development of ultra-thin, ultra-wideband MMA for mm-Wave applications. To develop a thin ultra-wideband absorber, the designed structure should be matched to the impedance of free-space and the thickness

of structure should be minimum. In this suggested design, the overall size of the optimized MMA unit cell is 4.385 x 2.417 x 0.787 mm, which is very thin and compact in size compared to other published designs. The MMA consists of three layers, on the top of structure a combined letter-shape patch and two side patches, on the bottom, the ground plane exist and between them is the Rogers RT5880 substrate with a thickness of 0.787 mm. The Rogers RT5880 has a dielectric constant of ε_r= 2.2 and a loss tangent value of tan δ = 0.009 as previously given. The copper which is used on both patches and on the ground has a thickness of about 0.035 mm and a conductivity of 5.8 x 10^7 S/m. The developed design and the design parameters are given in Fig. 21, and Table 10.

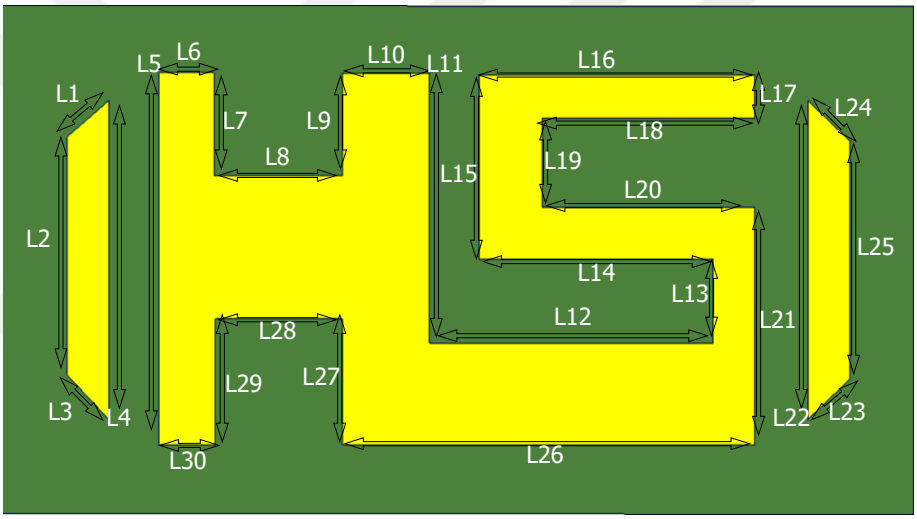

Figure 21. The proposed ultra-thin H&S MMA with design parameters.

Table 10. Design parameter values of proposed ultra-thin H&S MMA.

Parameters	**L_1**	**L_2**	**L_3**	**L_4**	**L_5**
Value (mm)	0.276462	1.145340	0.276462	1.527120	1.785085
Parameters	**L_6**	**L_7**	**L_8**	**L_9**	**L_{10}**
Value (mm)	0.265630	0.493622	0.623170	0.493622	0.423219
Parameters	**L_{11}**	**L_{12}**	**L_{13}**	**L_{14}**	**L_{15}**
Value (mm)	1.296231	1.373369	0.404656	1.135240	0.884104
Parameters	**L_{16}**	**L_{17}**	**L_{18}**	**L_{19}**	**L_{20}**
Value (mm)	1.338743	0.206040	1.031703	0.401948	1.033183

Table 10 (continued)

Parameters	**L_{21}**	**L_{22}**	**L_{23}**	**L_{24}**	**L_{25}**
Value (mm)	1.137943	1.527120	0.276462	0.276462	1.145340
Parameters	**L_{26}**	**L_{27}**	**L_{28}**	**L_{29}**	**L_{30}**
Value (mm)	2.005343	0.604663	0.616100	0.604663	0.272700

3.4.2. Parametric Studies of Substrate Thickness on H&S MMA

To achieve ultra-wideband MMA with ultra-thin structure, several parametric studies were conducted on the substrate thickness of the design, these studies were performed with the consideration of the fabrication tolerances and to be ready to be fabricated on standard PCB properties.

To perform a parametric study on the substrate thickness, the following thickness values of the Rogers RT5880 substrate were chosen as 0.381 mm, 0.508 mm, 0.787 mm. Figure. 22 clearly shows that thin structure can resonate over a wide-bandwidth.

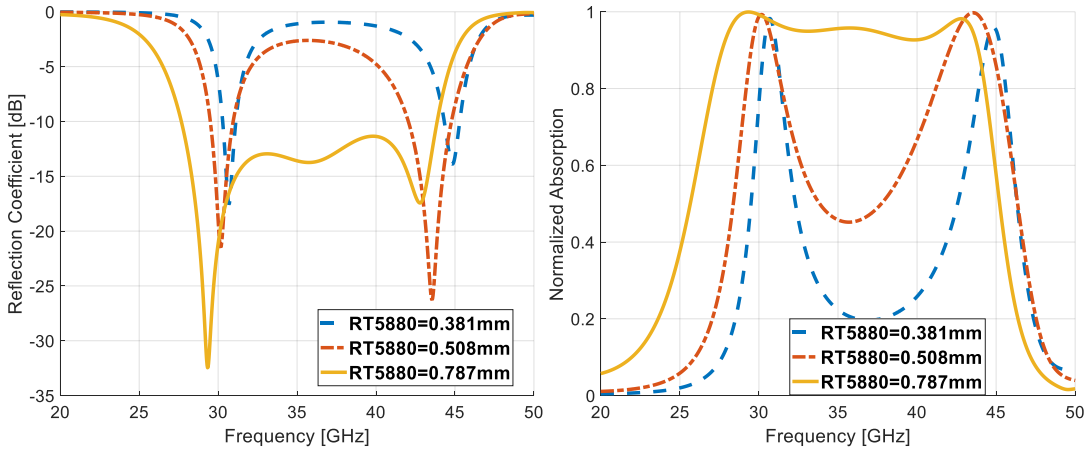

a) b)

Figure 22. The effects of the parametric study on the substrate thickness of H&S MMA a) reflection coefficients b) normalized absorption rates

Figure 22 demonstrates that if the substrate is not enough to create a resonance, the developed design is reflecting the electromagnetic waves from the structure to free-space instead of absorbing the waves.

3.4.3. Parametric studies of scaling factors of side patches on the developed H&S MMA

The final optimized design is achieved by scaling the two side patches. To see their effects on the output resonance frequencies and absorption rates, parametric studies were conducted in the range of scaling factors of 0.4, 0.8, 1.01 on the scale ratio in addition to the case without the two side patches.

As can be seen from the Fig. 23, the effect of the side patches is remarkably affecting the absorption rates of the MMA. The bandwidth of the structure is narrow, and the absorption rate are significantly low without the usage of both side patches.

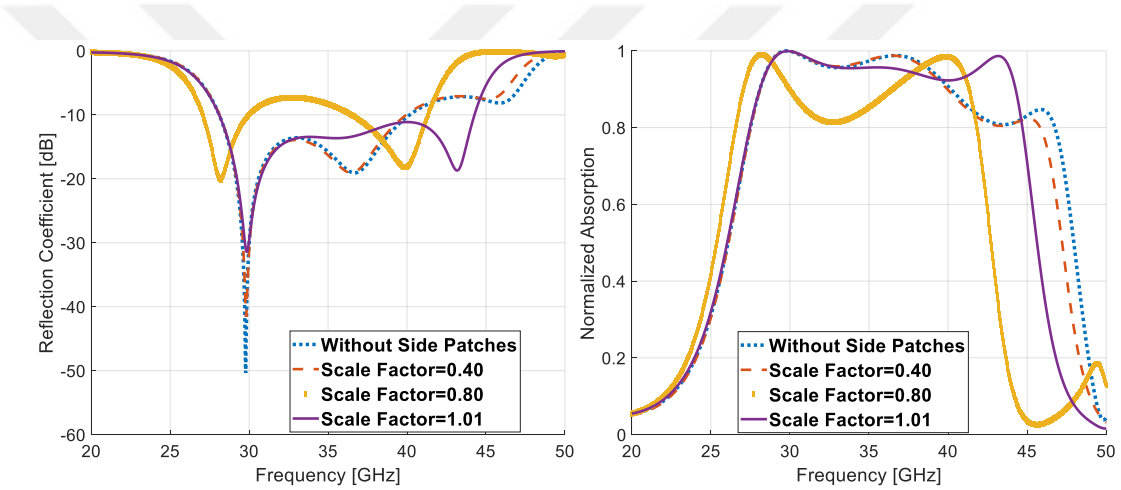

a) b)

Figure 23. The effects of the parameters of the side patches on the H&S MMA a) reflection coefficients b) normalized absorption rates

As shown in Fig. 23, the presence of the side patches reduces the return losses while also assisting in the generation of a multi-resonant structure, which in turn generates wider bandwidths and higher absorption rates. As shown in Fig. 23, a scaling factor of 1.01 is providing the maximum absorption bandwidth.

3.4.4. Parametric Scaling Studies of Letter-shape Patch on H&S MMA

With the target to achieve the maximum widest bandwidth and high average absorption rates, we vary one more parameter of the design, namely the size of the two letters. The combined letter shapes (H & S) are now scaled with a scaling factor of 0.85, 0.90, 0.95, 1.01.

After the numerical plane-wave simulations and computations of the scaling factors are done, a value of 1.01 is found as the optimum scaling factor and the final design parameters were determined according to this parameter. The results of the parametric studies are given in Fig. 24.

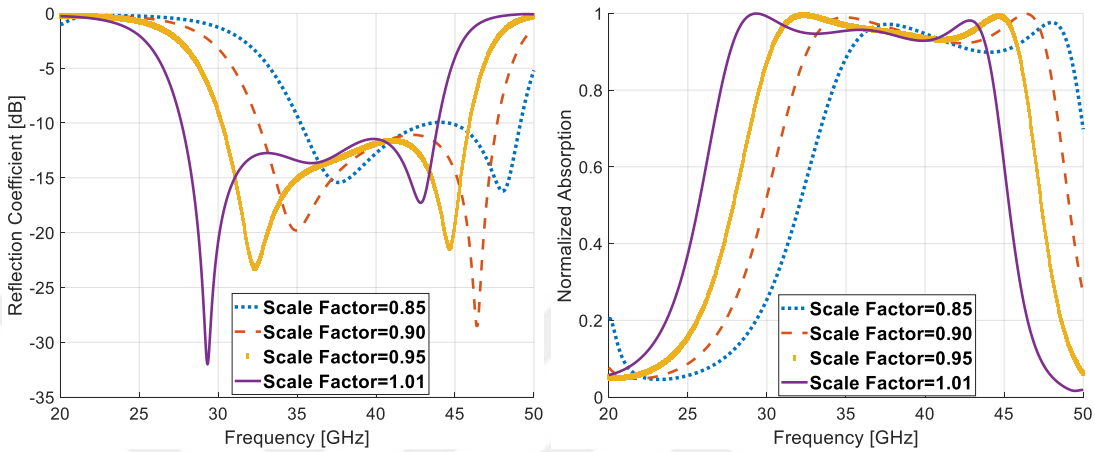

a) b)

Figure 24. The effects of the parameters on the combined letters of H&S MMA a) reflection coefficients b) normalized absorptions

As shown in Figures 23 and 24, a scaling factor of 1.01 is found optimum, and scaling of both geometries with the same factor offers the widest bandwidth achieved with a great average absorptivity rate.

3.4.5. Simulations and performance analysis of H&S MMA

The obtained results of the MMA clearly indicate that the optimized design and parameters provide an ultra-wideband and ultra-thin MMA with high absorptivity rates. The final results of the optimized design are presented Fig. 25.

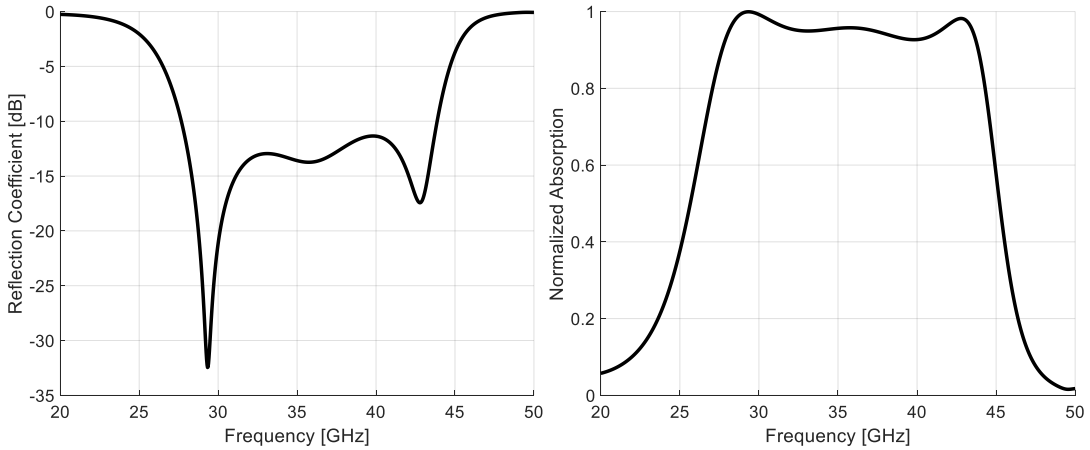

a) b)

Figure 25. The final optimized results of the ultra-thin H&S MMA
a) reflection coefficients b) normalized absorption rates

As it can be seen from Fig. 25, the designed MMA has ultra-wideband absorption bandwidth between the frequency range in the range from 27.67 GHz to 43.87 GHz with a minimum of 94% absorption rate and maximum peak of about 99.99%. This provide fractional bandwidth of 45.28% with an average absorption rate of 96.995% by the proposed ultra-thin MMA, which covers the higher frequency of the 5G mm-wave applications.

3.4.6. Effects of angles of incidence on the H&S MMA

In the MMAs, the stability of the absorbers in terms of angle of incidence at different incident angles is one of the requirements of metamaterial-based absorbers.

In this study, to examine whether the design facing different incident-angles shows a stable absorptivity or not, a parametric study was conducted for different incident angles in the range between $\theta=0°$ and 30°. The results are given in Fig. 26.

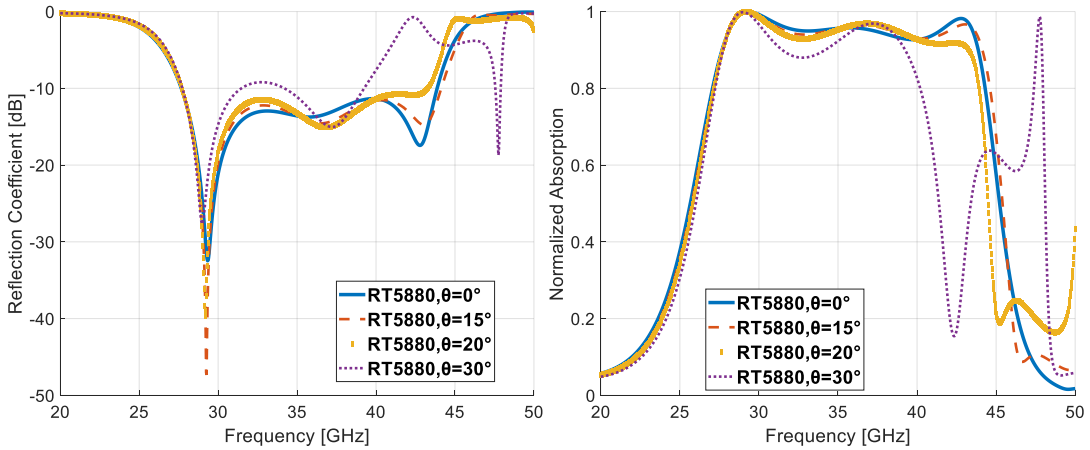

a) b)

Figure 26. The impacts of incident angle on H&S MMA a) reflection coefficients b) normalized absorptions

As shown in Fig. 26, it is clearly presented that the proposed unit cell design has a stable absorptivity in the range between θ= 0° to 30° with an ultra-wideband bandwidth property. The absorptivity rate of the MMA is still above 95% in the incident angle range of 0° to 20°. On the other hand, for an incident angle θ=30°, the absorptivity rate decreases to 88.8%. A common bandwidth of approximately 11.9 GHz is found for a θ=0° to 30.

3.4.7. Conclusion of H&S MMA Design

In this work, a novel compact and ultra-thin MMA is designed which has about 0.787 mm substrate thickness, the designed structure is well fitting for the military stealth, specific absorption rate (SAR) reduction, electromagnetic interference reduction, and electromagnetic energy harvesting applications. The final results are obtained by merging multiple resonance structures such as side patches and combined letter-shape patches. The proposed MMA has ultra-wideband property in the frequency range from 27.67 GHz to 43.87 GHz with an absorptivity peak of 99.9 % and an average of 96.5 % absorptivity rate.

3.5. Development of metamaterial absorber with lumped elements for the bandwidth improvements in usage of 5G millimeter-wave applications

Summary: In the symmetric absorbers as a nature of their symmetry the response of the absorbers to the different angle and conditions is decent. On the other hand, the bandwidth of the symmetrical designs are narrow and tight compared to asymmetrical designs. The main aim of this work is to enhance the narrow-band behavior of the developed symmetric MMA with the use of resistive lumped elements. This work presents a novel one-layer symmetrical MMA for mm-Wave applications. To obtain ultra-wideband absorber with a high absorptivity rate, a novel unit cell is developed and improved using the lumped elements technique.

The development process of the proposed work is summarized as follows:

1) Development of novel unit cell of octagonal design

2) Parametric studies of the designed octagonal MMA

3) Iterations of the optimized octagonal MMA geometry

4) Effects of the lumped elements on octagonal MMA

5) Effects of changing the resistive values on the octagonal MMA

6) Effect of incident angles on octagonal MMA

3.5.1. Unit Cell Design of Octagonal MMA

The initial goal of this study is to develop a symmetric MMA unit cell for millimeter-wave applications. The developed unit cell is achieved by the use of symmetrical octagonal cut rings and octagonal ring patch geometry printed on a 10 x 10 mm grounded layer with a Rogers RT5880 substrate (relative permittivity ε_r = 2.2 and dielectric loss tangent of tanδ = 0.0009). The copper layer has a 0.035 mm thickness and conductivity of 5.96 x 10^7 S/m. To enhance the absorption bandwidth of the MMA design, a technique based on lumped elements is applied to the proposed octagonal MMA. The proposed MMA design can be seen in Fig. 27 (b), and the final optimized unit cell design is achieved after three iterations as shown in Fig. 27 (a).

a)

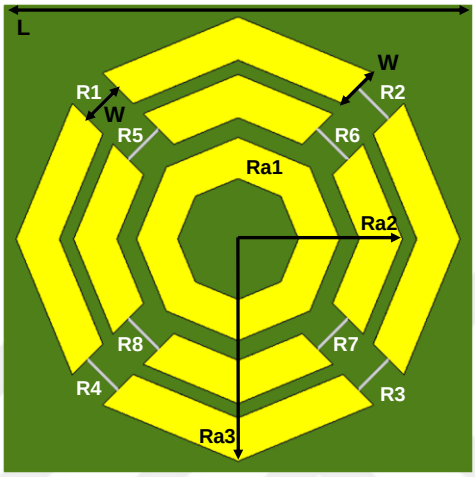

b)

Figure 27. The proposed octagonal MMA a) design iterations b) with design parameters and resistive values

Table 11. Design parameter values of the proposed octagonal MMA.

Parameters	**Ra_1**	**Ra_2**	**Ra_3**	**W**	**L**
Value (mm)	2.1612	3.5000	4.7250	0.9188	10.0000

Table 12. Resistor values of the proposed octagonal MMA.

Parameters	**R1**	**R2**	**R3**	**R4**
Value (Ω)	220	220	220	220
Parameters	**R5**	**R6**	**R7**	**R8**
Value (Ω)	370	370	370	370

3.5.2. Parametric studies and results of the octagonal MMA

This part intensely investigates the properties of the octagonal MMA in term of different resistive lumped element values, iterations of the geometries, and angles of incidences. Numerous simulations were run in order to improve the proposed symmetrical MMA's narrow bandwidth.

3.5.3. Iterations of the optimized octagonal MMA geometry

The final design is achieved after three iterations and could be seen in Fig. 28.

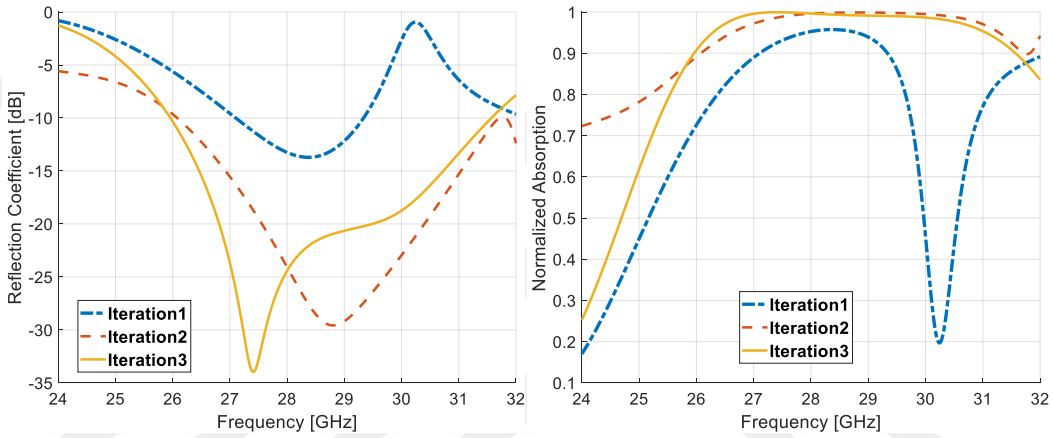

a) b)

Figure 28. Impacts of the iterations on proposed octagonal MMA a) reflection coefficients b) normalized absorption rates

The first iteration of MMA design consists of only one octagonal-shaped cut ring as can be seen in Fig. 27 (a). The corresponding bandwidth of the first iteration is narrow compared to the other iterations as depicted in Fig. 28. On the second iteration, the bandwidth of the octagonal MMA is higher than the first and third iteration, but it should be taken into account that the absorption rate of the second iteration is lower than the third iteration. On the third iteration the bandwidth and the absorption rate of the proposed MMA is proper for the final achieved result.

3.5.4. Effect of the lumped elements on octagonal MMA

As previously mentioned, the main aim of this work is the development of a symmetric MMA and then the enhancement of the narrow bandwidth of the MMA. One of the important techniques to obtain a significant enhancement in the proposed MMA is the use of lumped elements. The simulations were run two times, one with lumped elements and the second without lumped elements as shown in Fig. 29.

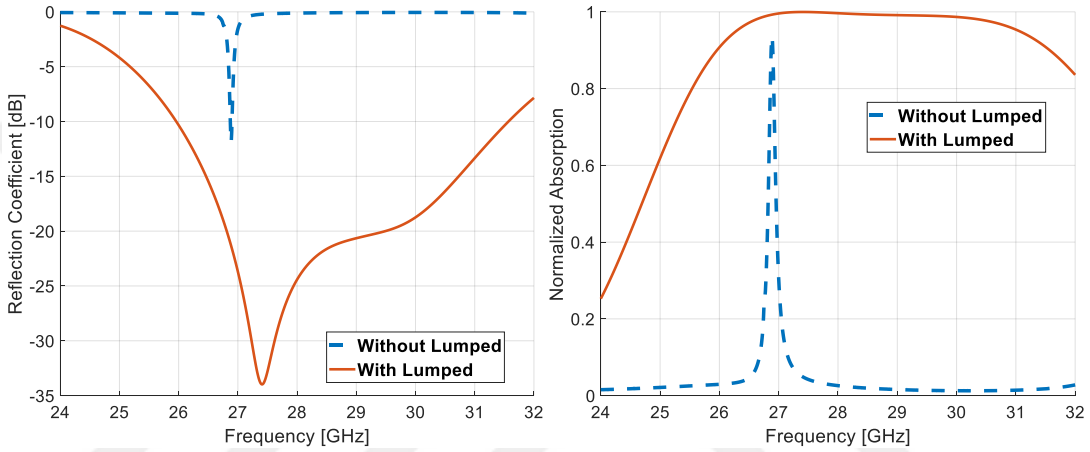

a) b)

Figure 29. The effect of the lumped element on proposed octagonal MMA a) reflection coefficients b) normalized absorption rates

As shown in Table 13, there are noteworthy enhancements in the absorption rate and in the bandwidth. The fractional bandwidth of the design with lumped resistors is nearly 187.5 times larger than the bandwidth of the case without lumped elements. The employment of resistive lumped elements increases the absorption peak of 99% and on the average about 98%.

Table 13. A comparison with and without lumped elements on the obtained absorptivity values in term of bandwidth.

MMA Type	**Frequency Range**	**Fractional Bandwidth**	**Absorptivity (%)**	**Unit Cell Size (mm^3)**
Without Lumped	26.872-26.90 GHz	0.104 %	≈ 93.5	10 x 10 x 1.575
With Lumped	25.959-31.57 GHz	19.50 %	≈ 98	10 x 10 x 1.575

3.5.5. Effects of changing resistive values on octagonal MMA

To show the effects of changing the resistive values on the performance unit cell, a parametric is study prepared. This parametric study is demonstrated by varying the optimized values with factors of 0.5 and 1.5 as seen in Fig. 30.

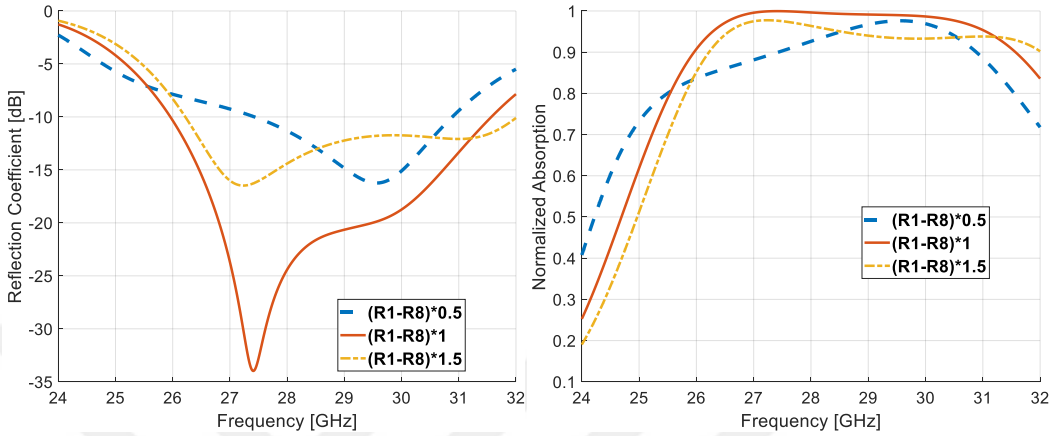

a) b)

Figure 30. The effects of the resistance values on octagonal MMA a) reflection coefficients b) normalized absorption rates

The increase in the resistance values by a factor of 1.5 decreases the absorption rate about 6%. On the other hand, decreasing the resistance values by a factor of 0.5 decreases the absorption bandwidth around 12.4%.

3.5.6. Effect of Incident angles on the octagonal MMA

As previously mentioned, the stability of MMAs under different angles of incidence is so crucial when dealing with so many incident oblique angles. To examine the common bandwidth of this proposed octagonal MMA, a parametric study was conducted with the use of different incident angles ranging from θ=0°-20° as seen in Fig. 31.

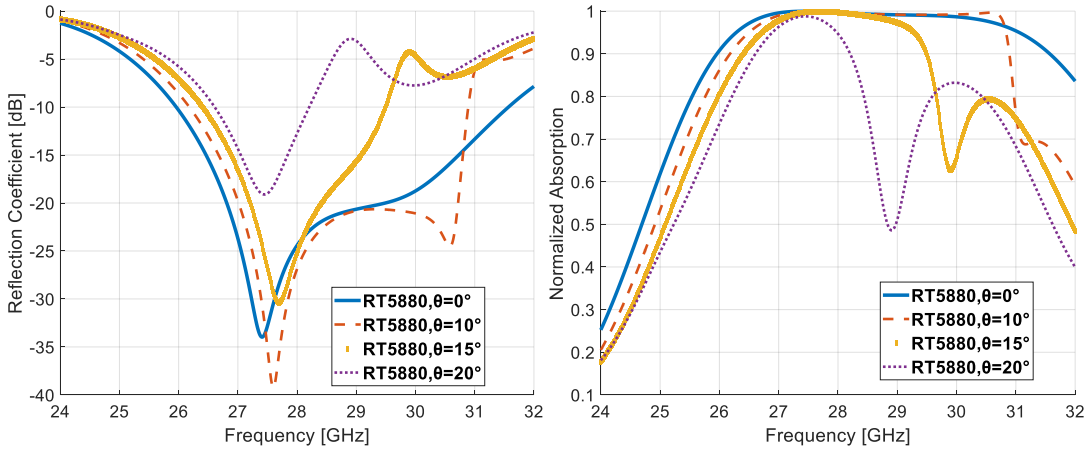

a) b)

Figure 31. The impacts of incident angles on the octagonal MMA a) reflection coefficients b) normalized absorption rates

According to the achieved results, a common bandwidth of around 4.64 GHz is reached for θ = 0°-10°. For incident angles in the range from 0° to 15°, a common bandwidth of 3.1 GHz is achieved. For a θ = 0° - 20°, a common bandwidth of about 1.6 GHz is found.

3.5.7. Conclusion of octagonal MMA design

In this study, the development of wideband symmetrical MMA is achieved with using lumped resistive elements. A novel octagonal unit cell of this symmetrical MMA is very suitable for mm-wave applications. The obtained results showed that the developed and enhanced MMA has wideband property. This study proved that the use of resistive elements could improve the narrow bandwidth of symmetrical MMA's. The achieved results are promising that in the future works a symmetrical ultrawideband MMA can be designed with a using of lumped resistive elements.

3.6. Development of a novel ultra-wideband textile-based metamaterial absorber for mm-wave band applications

This study provides a novel ultra-wideband MMA for smart electronic textile (e-textile) applications. The design geometry is based on a new cell structure made up of two combined letter shape patches (A&S) printed on a grounded textile substrate. This unit cell architecture was designed and optimized exclusively for mm-wave applications.

The development steps of the proposed work is summarized as follows:

1) Novel unit cell of textile-based MMA design

2) Parametric studies of designed textile-based MMA

3) Comparison between PCB and textile-based substrates

4) The effect of substrate thickness on the absorption coefficient

5) Absorptivity rates of different textile-based materials

6) Effect of incident angles on the absorption rates

7) Bending effects

3.6.1. Unit Cell Design of A&S MMA

The current project aims to develop a novel MMA unit cell for textile-based fabric materials in the mm-wave ranges. To obtain high absorption rates at the desired operating frequencies, the size and geometrical characteristics of the MMA absorber's unit cell must be carefully optimized. The textile-based absorber design in this work is based on a new cell geometry made of two adjoined letters (A&S) and two side patches printed on a grounded textile substrate. The Felt dielectric material fabric is considered as a substrate for this design with relative permittivity of ε_r = 1.22, dielectric loss tangent of tanδ = 0.016, thermal conductivity of 0.05 W/m.K and with a 0.8 mm thickness. The patch, side patches and ground which uses copper with a

thickness of 0.035 mm and conductivity of 5.96 x 10^7 S/m. The proposed design is presented in Fig. 32 and the design parameters are given in Table 14.

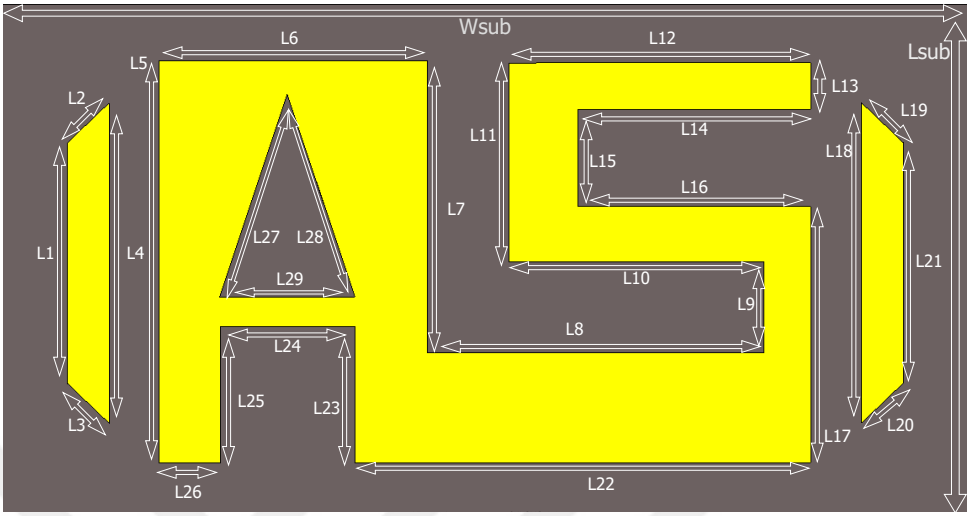

Figure 32. The proposed textile-based A&S MMA with design parameters.

Table 14. The proposed A&S MMA textile-based structure with design parameters.

Parameters	**L_1**	**L_2**	**L_3**	**L_4**	**L_5**
Value (mm)	1.0773	0.2600	0.2600	1.4364	1.8029
Parameters	**L_6**	**L_7**	**L_8**	**L_9**	**L_{10}**
Value (mm)	1.2038	1.3092	1.5084	0.4073	1.1413
Parameters	**L_{11}**	**L_{12}**	**L_{13}**	**L_{14}**	**L_{15}**
Value (mm)	0.8929	1.3521	0.2081	1.0420	0.4060
Parameters	**L_{16}**	**L_{17}**	**L_{18}**	**L_{19}**	**L_{20}**
Value (mm)	1.0435	1.1493	1.4364	0.2600	0.2600
Parameters	**L_{21}**	**L_{22}**	**L_{23}**	**L_{24}**	**L_{25}**
Value (mm)	1.0773	2.0451	0.6107	0.6026	0.6107
Parameters	**L_{26}**	**L_{27}**	**L_{28}**	**L_{29}**	**L_{Sub}, W_{Sub}**
Value (mm)	0.2754	0.9582	0.9582	0.6060	2.32 / 4.35

3.6.2. Parametric Studies and Results of A&S MMA

In this part, the characteristics of the MMA are analyzed in term of different types of materials, textile-based substrates, substrate's thicknesses, dielectric loss tangents, angles of incidence, and the material flexibility.

3.6.3. Comparison between PCB and Textile-based substrates on A&S MMA

The flexible textile-based fabric dielectric materials are compared to the standard rigid PCB technology. The used parameters are given in the comparison and in the study as stated in Table 15.

Table 15. The physical parameters of FR-4, Rogers RT5880 and FELT.

Textile Type	Dielectric Constant	Tangent Loss	Thermal Conductivity (W/m.K)
FR-4	4.3	0.02	0.025
Rogers RT5880	1.7	0.0009	0.020
FELT	1.22	0.016	0.050

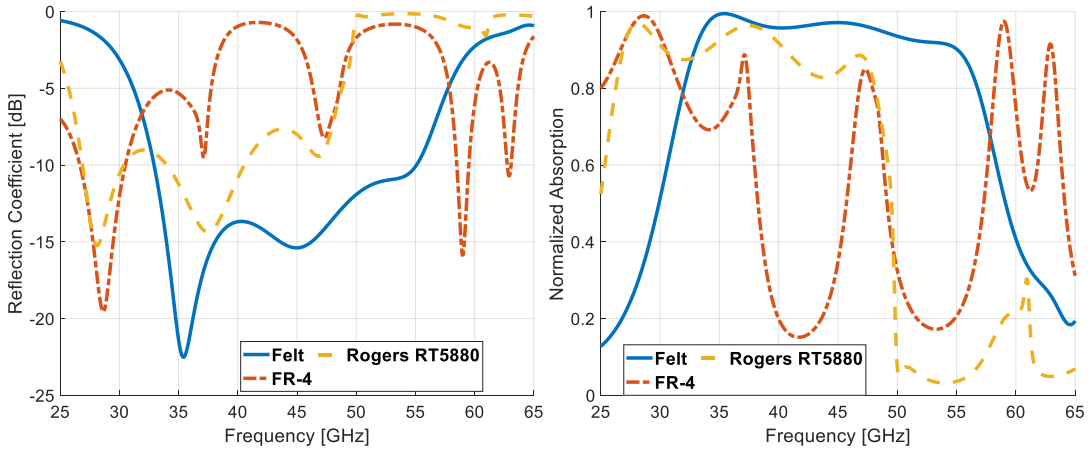

a) b)

Figure 33. A comparison between a textile-based material and its counterparts PCBs on A&S MMA a) reflection coefficients b) normalized absorption rates

As shown in Fig. 33, the comparison demonstrates that the Felt fabric has the widest bandwidth, whereas the PCB-based rigid materials have narrow bandwidths in comparison to the Felt's ultra-wideband characteristic. Over the whole bandwidth, the textile-based Felt material achieves absorption rates of more than 90%. In Table 16, the output results of the materials can be seen in term of the fractional bandwidth, absorptivity, and dimensions.

Table 16. A comparison of conventional PCB and Textile-based substrates on the A&S MMA fractional bandwidth, absorptivity rates and cell size.

Material Type	**Frequency Range**	**Fractional Bandwidth**	**Absorptivity (%)**	**Unit Cell Size (mm^3)**
FR-4	26.61-30.49 GHz & 58.48-59.50 GHz	13.59 % & 1.73 %	≈ 96	4.35 x 2.32 x 0.8
RT-5880	26.88-40.55 GHz	40.54 %	≈ 90	4.35 x 2.32 x 0.787
FELT	32.92-55.08 GHz	50.36 %	≈ 94	4.35 x 2.32 x 0.8

As given in Table 16, it is indicated that the -10 dB absorption bandwidth of the textile material Felt is higher than 10% of that shown by RT-5880 and with an average absorption rate of 94.67%.

3.6.4. The effect of substrate thickness on the A&S MMA

Four substrate thickness values between 0.6 and 1.2 mm are investigated in order to obtain a better knowledge of the effect of adjusting the substrate thickness on the performance of the suggested MMA. The absorption bandwidth is considerably affected by changing the thickness. When the thickness of the substrate is reduced to the 0.6 mm, the resonance frequency shift toward to higher frequencies as the absorption bandwidth is decreased. Simultaneously, as the thickness of the substrate increased from 0.8 mm to 1 mm, the resonance frequency shift towards lower

frequencies, resulting in a massive drop in the absorption rate and absorption bandwidth as observed in Fig. 34.

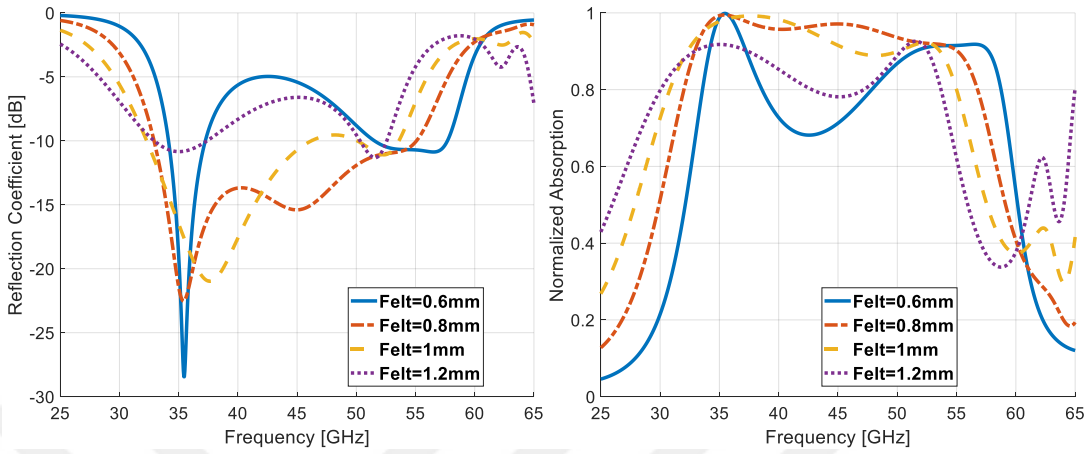

a) b)

Figure 34. The effects of the substrate thickness on A&S design MMA a) reflection coefficients b) normalized absorption rates

3.6.5. Effect of different textile-based materials on A&S MMA

The simulations are performed on three different textile-based fabric substrates in this comparison, namely, Felt, Denim, and Polyester, as shown in Table 17.

Table 17. Physical parameters of textile-based Felt, Denim, Polyester substrates.

Textile Type	**Dielectric Constant**	**Tangent Loss**	**Thermal Conductivity (W/m.K)**
FELT	1.22	0.016	0.050
DENIM	1.7	0.025	0.050
POLYESTER	1.9	0.0045	0.14

Figure 35 depicts the results of the reflection coefficients and the absorption rates. Among the three textiles, the Felt fabric substrate has the lowest dielectric constant, resulting in the best results in term of reflection coefficients and absorption rates.

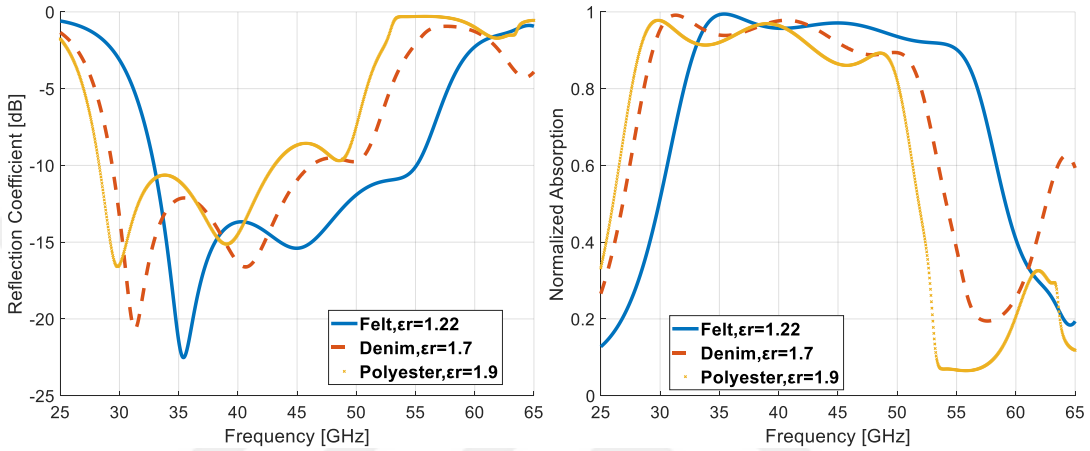

a) b)

Figure 35. The effects of the textile-based substrate type on A&S MMA a) reflection coefficients b) normalized absorption rates

For Felt, Denim, and Polyester, the achieved fractional absorption bandwidths are 50.36 %, 44.49 %, and 41.42 %, respectively.

3.6.6. Effect of Incident Angle on The Absorption Rates of A&S MMA

This part is focusing on the determination of a consistent common resonance band for various angles of incidence of the electromagnetic waves reaching the unit cell. The characteristics of the Felt substrate are analyzed as a function of the incident angles from θ=0° to 30° as given in Fig. 36.

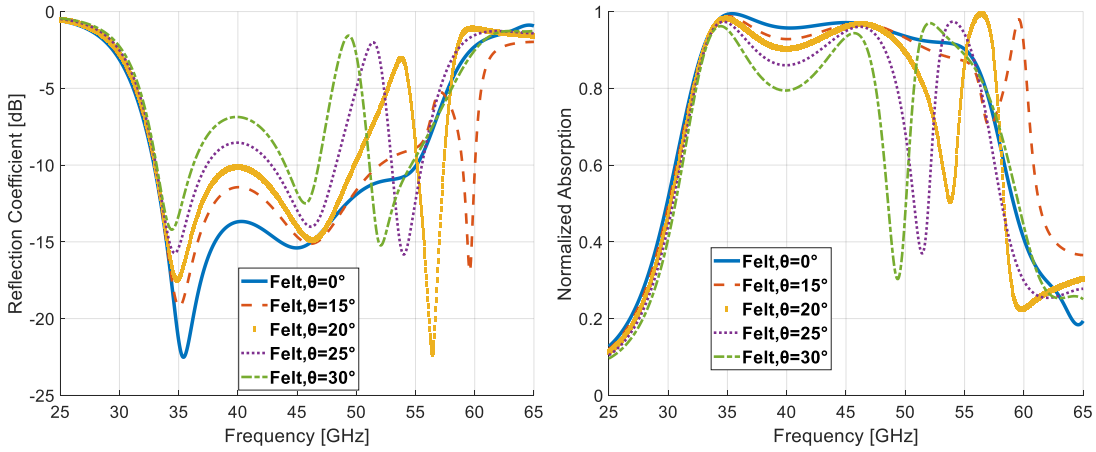

a) b)

Figure 36. The effects of the incident angles on A&S MMA a) reflection coefficients b) normalized absorption rates

The absorption rate of the proposed MMA unit cell diminishes as the angle of incidence increases. According to the obtained results, for incident angles between 0° and 25°, a common bandwidth of roughly 16 GHz is found with an average absorption rate of about 90%.

3.6.7. Bending Effects on the A&S MMA

Lightness, flexibility, and breathable characteristics are some of the essential attributes of textile-based MMAs. Simulations are run in this section to determine the impacts of elasticity on the proposed MMA. Under diverse bending situations, the produced MMA must retain the same performance, operation frequencies, and absorption rates. To investigate the bending effects, several cylinders with radii of 3, 5, 7, 9, 11, 12 mm are employed as shown in Fig. 38.

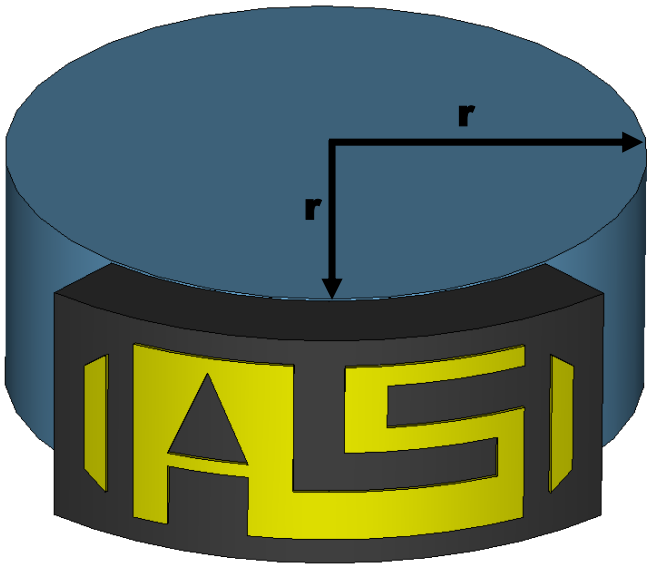

Figure 37. An illustration of the proposed A&S MMA with a cylindrical bent angle r.

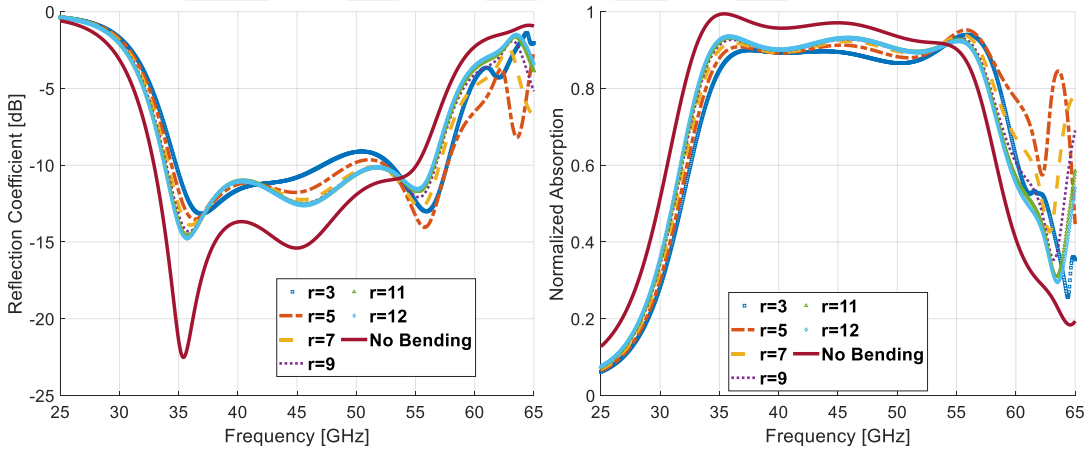

a) b)

Figure 38. Impacts of the bending on the A&S MMA a) reflection coefficients b) normalized absorption rates

It is worth noting that, based on the reflection coefficient and normalized absorption rates shown in Fig. 37, the MMA retains ultra-wideband bandwidth and decent absorption rates under various bending situations. Nonetheless, between the curvatures r = 3 - 12 mm, there are some minor shifts toward higher resonance frequencies. The 3 mm radius of curvature results in a significant right-handed shift

and slight reductions in absorption rate. The maximum absorption rates are obtained when the structures are at flat level. Under high curvature circumstances, the bandwidth drops. This may be explained by the worsening of the impedance matching between the air and the unit cell of the MMA, which causes the reflection coefficient to increase.

The results show an inverse relationship between the reflection coefficient and the rate of curvature, with larger curvature resulting in narrower bandwidths and higher absorption rates. Finally, even under varying different bending situations, the suggested MMA preserves the ultra-wideband feature with absorption rates more than 90%.

After completing the whole parametric studies, the achieved final results of the developed MMA are compared with the other previously developed studies as seen in Table 18.

Table 18. A comparison of the Textile-based flexible MMAs and proposed A&S MMA's obtained absorptivity values in term of dimensions with the related previous studies.

Material Type	**Frequency Range**	**Absorption Fractional Bandwidth**	**Absorptivity (%)**	**Unit Cell Size (mm^3)**	**References**
FELT	9–10.5 GHz	15.43 %	≈ 90	30 x 30 x 1.0	(Tak and Choi, 2017)
FELT	4.9-5.06 GHz	3.21 %	≈ 99	18 x 18 x 2.0	(Bait-Suwailam *et al.*, 2019)
FELT	32.92-55.08 GHz	50.36%	≈ 99	4.35 x 2.32 x 0.8	Our MMA

In comparison to previous recent researches, as shown in Table 15, the new designed unit cell is significantly smaller, compact, and demonstrates an ultra-wideband characteristic with a low-profile structure, allowing for easy production.

3.6.8. Conclusion of A&S MMA Design

This research is focused on the development of textile-based ultra-wideband MMA that can be used in a variety of textile application while a unique unit cell shape is developed and optimized. The current study takes into account three distinct fabrics: Felt, Denim, and Polyester. According to the simulation results, the Felt fabric substrate has the largest -10 dB fractional bandwidth of 50.36%, followed by Denim and Polyester with 44.49% and 41.42 %, respectively. The bending of the structure has minor effect on the absorption rate, indicating that the designed unit cell shape is well tailored for textile-based applications. The study concludes that textile-based fabric substrates may outperform rigid PCB-based MMAs in terms of ultra-wideband feature and persistent absorption rates. The three textile-based fabrics, Felt, Denim, and Polyester, all have a common bandwidth of around 10 GHz. The noteworthy finding of the current study is the ultra-wideband resonance. The suggested MMA can serve as the foundation for military and biomedical textile-based applications, as well as camouflage and health monitoring systems.

3.7. Development of a Split-Ring-Resonator Based Ultra-Wideband Textile-Based Metamaterial Absorber for Millimeter-Wave Applications

Summary: The current research describes the development of a low-profile symmetrical MMA for mm-wave applications. The goal is to develop an ultra-wideband Split Ring Resonator (SRR) structure with high absorptivity rates. The concept is based on SRR with multiple cuts printed on a flexible grounded Felt substrate. This structure's unit cell is designed and improved using the lumped components approach to provide ultra-wideband properties with high absorptivity rates.

The steps followed in the development of structure are as follows:

1) Development of unit cell based on SRR MMA

2) Parametric studies and parameters optimizations

3) Effect of lumped elements

4) Effect of angles of incidence

5) Bending effect

6) Conclusion

3.7.1. Proposed Unit Cell of SRR MMA

Many factors, including the radius of the unit rings, the spacing between the rings, and the width of the rings, must be optimized in the proposed textile-based MMA unit cell architecture as depicted in Fig. 39.

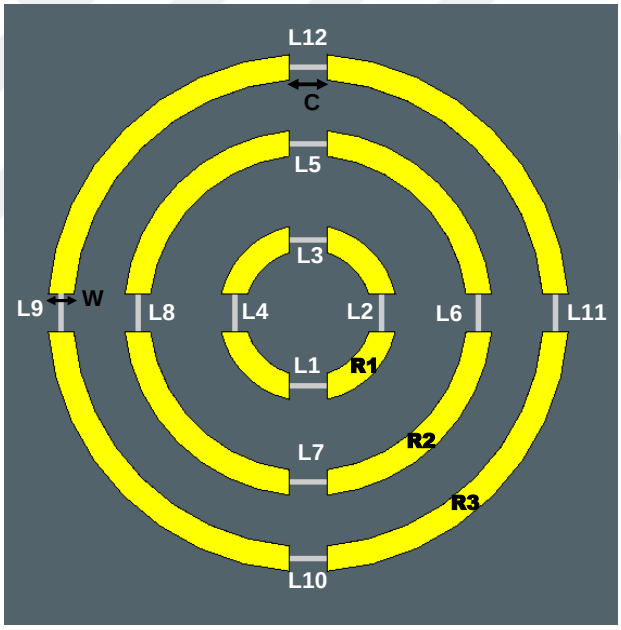

Figure 39. Proposed unit cell of textile-based SRR MMA.

In this study, the Felt textile-based fabric used as a dielectric substrate with a relative permittivity ε_r = 1.22, dielectric loss tangent of tanδ = 0.016, thermal conductivity of 0.05 W/m.K and with a 1.4 mm thickness. The optimized unit cell is developed by using a symmetrical split ring resonator with distinct cuts manufactured

on copper with a thickness of 0.035 mm and a conductivity of 5.96 x 10^7 S/m and printed on grounded 5x5 mm^2 Felt dielectric material. Tables 19 and 20 show the optimal values of the parameters and lumped elements, respectively.

Table 19. Parameter values of the SRR MMA design.

Parameters	**R1**	**R2**	**R3**	**W**	**C**
Value (mm)	0.7000	1.4500	2.0500	0.2096	0.3000

Table 20. Optimized resistor values of the SRR-MMA design.

Parameters	**L_1**	**L_2**	**L_3**	**L_4**
Value (Ω)	400	400	400	400
Parameters	**L_5**	**L_6**	**L_7**	**L_8**
Value (Ω)	400	400	400	400
Parameters	**L_9**	**L_{10}**	**L_{11}**	**L_{12}**
Value (Ω)	400	400	400	400

3.7.2. Parametric studies and results of SRR-MMA

To achieve optimized design and parameters, several parametric studies were conducted on SRR textile-based material. Several simulations were run to increase the narrow-bandwidth of the proposed symmetrical SRR - MMA and to determine the best resistive values of the lumped parts.

3.7.3. Effect of Lumped Elements on SRR MMA

Various plane-wave simulations were used to find the optimal resistor settings for this MMA, Table 17 depicts that a value of 400 ohm is optimal for the whole lumped elements. To demonstrate the effect of lumped resistive elements on MMA

performance, two sets of simulations were computed, the first with lumped elements and the second without; the results are shown in Fig. 40.

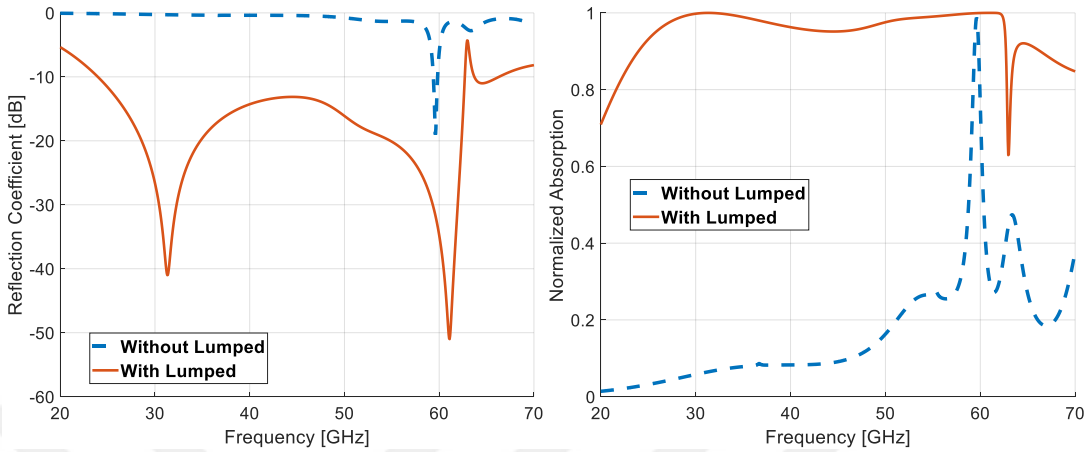

a) b)

Figure 40. The effect of the lumped elements on SRR MMA a) reflection coefficient b) normalized absorption

Table 21. A comparison of two SRR MMA Felt absorber, with and without lumped elements.

Absorber Type	**Frequency Range (GHz)**	**Fractional Bandwidth**	**Absorptivity (%)**	**Unit Cell Size (mm^2)**
Without Lumped	59.38 - 59.83	0.76 %	≈ 98	5x5
With Lumped	24.49 - 60.98	85.38 %	≈ 98	5x5

The absorption rates and bandwidths are significantly improved, as shown in Table 21. The fractional bandwidth of the SRR design with lumped resistors is roughly 84.62% larger than the fractional bandwidth of the structure without lumped parts. The addition of resistive components boosts the absorption rates to a maximum of 99.9 % and to an average value of about 98% throughout the whole bandwidth.

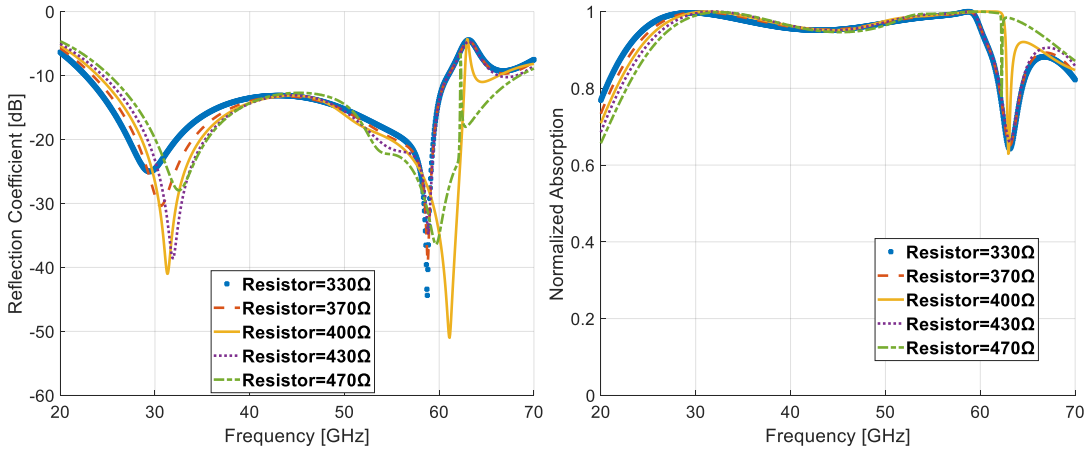

a) b)

Figure 41. The impacts of the resistor values on the proposed SRR MMA a) reflection coefficients b) normalized absorption rates

Changing the resistor values from 330 to 470 ohm, as shown in Fig. 41, the best value for the optimized structure is 400 Ω found, which corresponds to the absorption peak 99.9989%, average absorption rate of 98, and the fractional bandwidth of 85.38%. For dropping resistive value of 400 Ω to 330 Ω resulted with the falling of the fractional absorption bandwidth 1.38% and lessened of the average absorption rate of 1.25%. As a result of this reducing the resistive values consequences in a decrease of the absorption rates, absorption bandwidths and absorption peaks.

3.7.4. Effect of angle of incidences on SRR MMA

The influence of angle of incidence on absorption rates is considered to be essential, materials are exposed to electromagnetic waves at varied incident angles.

The computations are extended for the same SRR MMA design and with incidence angles ranging from θ= 0° to 60°.

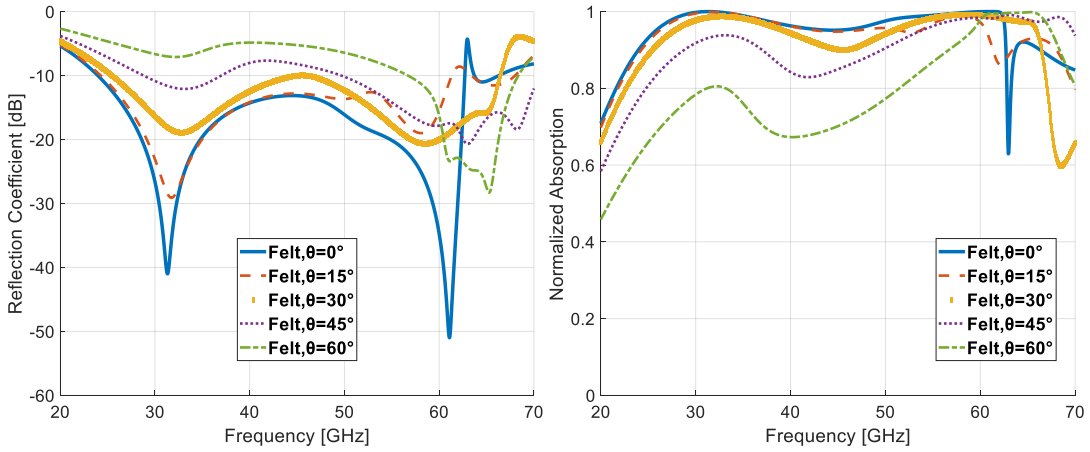

a) b)

Figure 42. The impacts of the incident angle on the proposed SRR MMA a) reflection coefficients b) normalized absorption rates

The data shown in Figure 42 (a & b) reveal that the absorption rates drop as the angle of incidence increases. A common ultra-wideband from 30 to 62 GHz is produced at angles ranging from θ= 0° to 30°, with average absorption rates above 90%. The proposed design exhibits persistent behavior in terms of absorption rates and maintains ultra-wideband behavior up to an angle of θ= 30°.

3.7.5. Bending effect of SRR MMA

The elasticity of textiles provides a fantastic opportunity to produce wearable ideal absorbers for diversity of applications. The elasticity of the existing design is studied in terms of different curvatures in this part, with the goal of ensuring that the MMA maintains constant high performance in terms of absorption rates and operating abilities under diverse curvature values and this bending operations are illustrated in Fig. 43.

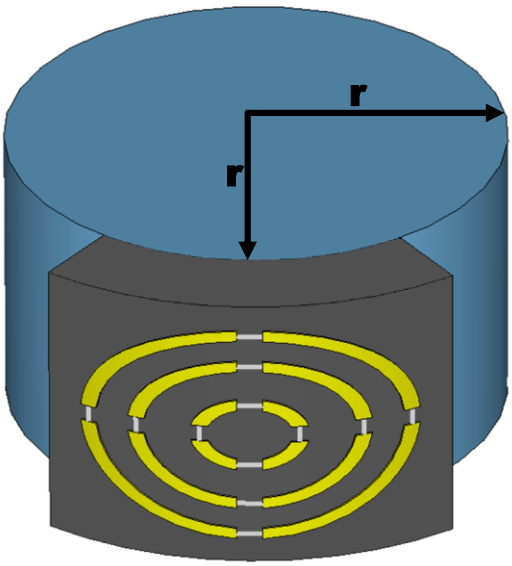

Figure 43. An illustration of SRR MMA with a cylindrical bend angle r.

Various cylinders with radii ranging from 5 to 15 mm are considered, and a visualization of the cylindrical bending is shown in Fig. 43. The obtained findings, as shown in Fig. 44 (a & b), reveals that the ideal scenario with no bending has the widest absorption bandwidth and the highest normalized absorption rate.

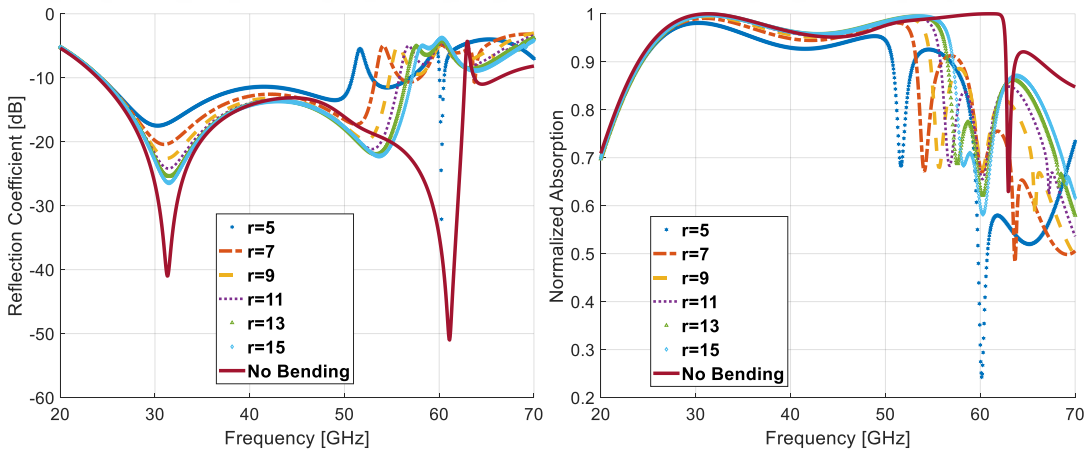

a) b)

Figure 44. The impacts of the bending condition on SRR MMA a) reflection coefficient b) normalized absorption

Table 22. A comparison of the currently obtained SRR - MMA results with previous studies.

Material Type	Frequency Range	Absorption Fractional Bandwidth	Absorptivity (%)	Unit Cell Size (mm^3)	Ref.
FELT	9–10.5 GHz	15.43%	≈ 90	30 x30 x 1.0	(Tak and Choi, 2017)
FELT	4.9-5.06 GHz	3.21 %	≈ 99	18 x 18 x 2.0	(Bait-Suwailam *et al.*, 2019)
FELT	24.49-60.98 GHz	85.38%	≈ 98	5 x 5 x 1.4	Current MMA

A comparison with other recent researches, as shown in Table 22, reveals that the present unit cell design has an ultra-wideband property with a low profile structure and high absorptivity rates, allowing for the easy fabrication of textile-based mm-wave application systems.

3.7.6. Conclusion of SRR-MMA

The current study is primarily concerned with the creation of an ultra-wideband symmetrical SRR-MMA for mm-Wave applications. With the use of resistive lumped components, the unit cell of this structure is particularly developed and optimized for high absorptivity rates and ultra-wideband properties. The obtained results show that the suggested SRR - MMA has a reflective ultra-wideband -10 dB on the textile-based Felt fabric as a substrate. According to this research, using resistive lumped parts increased the fractional bandwidth by a factor of roughly 112.34. The suggested design maintains extremely high performance throughout a wide range of incidence angles. For angles ranging from θ= 0° to 30° and absorption rates above 90%, a consistent common ultra-wideband spanning 30 – 62 GHz is achieved. Under varied elasticity margins, the suggested MMA still exhibits ultra-wideband behavior and large absorption rates. This study's results are encouraging for the development of ultra-wideband smart-textile-based wearable applications such electromagnetic energy harvesters, health monitoring, and camouflage systems.

3.8. A novel textile-based 6G metamaterial absorber for 6G mm-wave applications

Summary: The current study proposes a new development of a low-profile asymmetrical textile-based MMA for 6G mm-wave applications. The objective is to design an MMA structure with high absorptivity rates in THz frequency ranges. The design is based on the combination of the number "6" and the letter "G" printed on a flexible grounded Felt substrate. The achieved results are encouraging and can be considered as basic blocks for future development of 6G smart wearable applications.

The steps followed in the development of the structure are as follows:

1) Designing unit cell of textile-based 6G MMA

2) Parametric studies of 6G MMA

3) Effects of different textile-based materials on the performance of the 6G MMA

4) The effect of substrate thickness on the 6G MMA

5) Effects of angles of incidence on the absorptivity rates of the MMA

6) Bending effects on 6G MMA

7) Conclusion

3.8.1. Proposed Unit Cell of Textile-based 6G MMA Design

In this study, the Felt textile fabric is employed as a dielectric substrate with a relative permittivity ε_r = 1.22, dielectric loss tangent of tanδ = 0.016, thermal conductivity of 0.05 W/m.K and with a 0.5 mm thickness. The reason of this choice is the very high performance (high absorptivity rates and ultra-wideband widths properties) shown in our previous studies. The optimized unit cell is designed by combining the number "6" with a letter "G", both are made of copper with a thickness of 0.035 mm and a conductivity of 5.96 x 10^7 S/m printed on grounded 2.1x2.1 mm^2 Felt dielectric material. As shown in Fig. 45 and Table 23, the unit cell design and parameters are depicted.

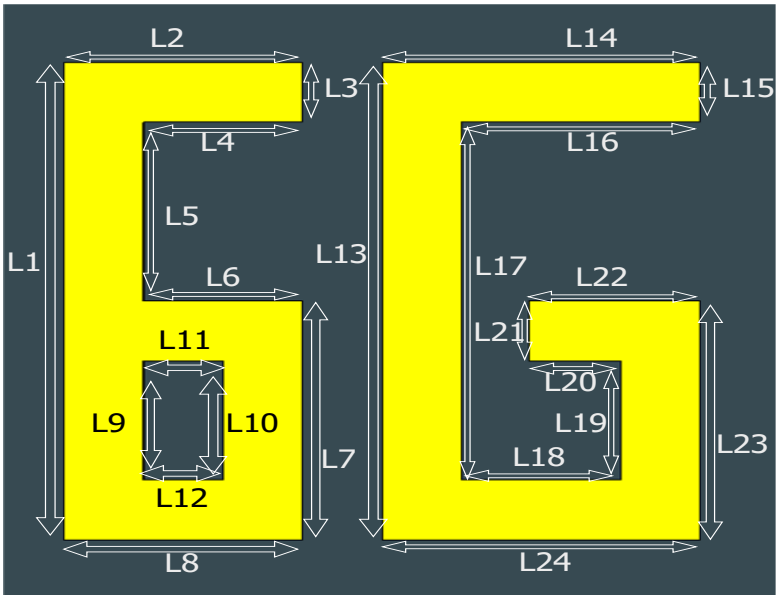

Figure 45. Proposed unit cell of textile-based 6G MMA.

Table 23. The design parameters of textile-based 6G MMA.

Parameters	**L1**	**L2**	**L3**	**L4**	**L5**	**L6**
Value (mm)	1.648320	0.618120	0.206040	0.412080	0.618120	0.412080
Parameters	**L7**	**L8**	**L9**	**L10**	**L11**	**L12**
Value (mm)	0.824160	0.618120	0.412080	0.412080	0.206040	0.206040
Parameters	**L13**	**L14**	**L15**	**L16**	**L17**	**L18**
Value (mm)	1.648320	0.824160	0.206040	0.618120	1.236240	0.412080
Parameters	**L19**	**L20**	**L21**	**L22**	**L23**	**L24**
Value (mm)	0.412080	0.238120	0.206040	0.444160	0.824160	0.824160

3.8.2. Parametric Studies on 6G MMA

Several parametric studies in 6G textile-based design were undertaken to obtain optimum design and parameters. Numerous simulations were performed in order to better understand the reaction of the proposed MMA and to identify the optimal material.

3.8.3. Response of Different Textile-based Materials on 6G MMA

Textile-based substrates are investigated in this comparative research, and simulations are performed on two distinct textiles with dielectric constants as shown in Table 24.

Table 24. A physical properties of Felt and Denim fabric materials.

Textile Type	Dielectric Constant	Tangent Loss	Thermal Conductivity (W/m.K)
FELT	1.22	0.016	0.050
DENIM	1.7	0.025	0.050

Fig. 46, depicts the computed reflection coefficients S_{11} and the absorption rates. The Felt material shows the highest results in term of operating frequency bandwidths, reflection coefficients, and absorption rates, while having the lowest dielectric constant of the two fabrics.

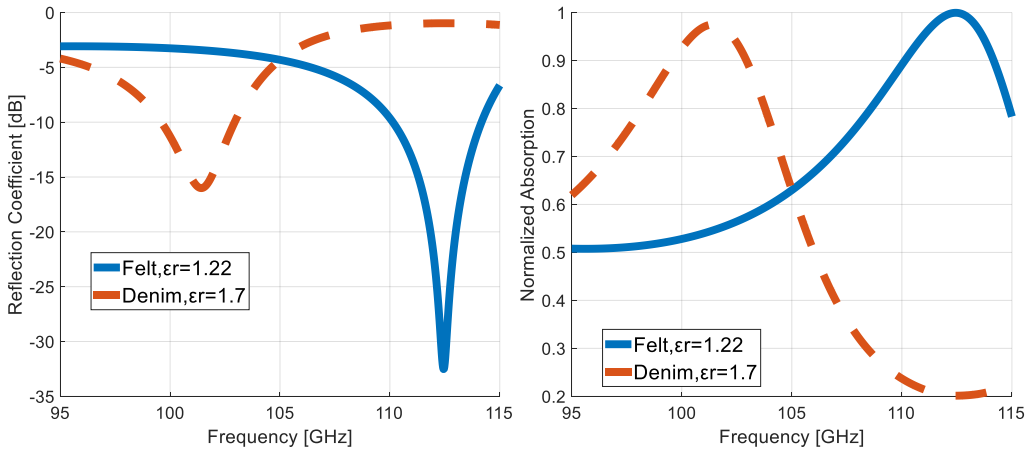

a) b)

Figure 46. The effects of the different textile-based substrate type on 6G MMA a) reflection coefficients b) normalized absorption rates

3.8.4. The effect of substrate thickness on the 6G MMA

Parametric experiments were conducted in five Felt thicknesses to examine the influence of increasing dielectric thickness on the operating performance of the proposed design: 0.2 mm, 0.4 mm, 0.5 mm, 0.6 mm, and 0.8 mm.

According to Fig. 47, increasing the thickness has an effect on the absorption bandwidth while resonances shift or reduce. The optimal thickness of 0.5 mm provides the optimum absorption bandwidth and absorption rate. It is crucial to note that the thickness of the substrate has a significant impact on the absorption rates.

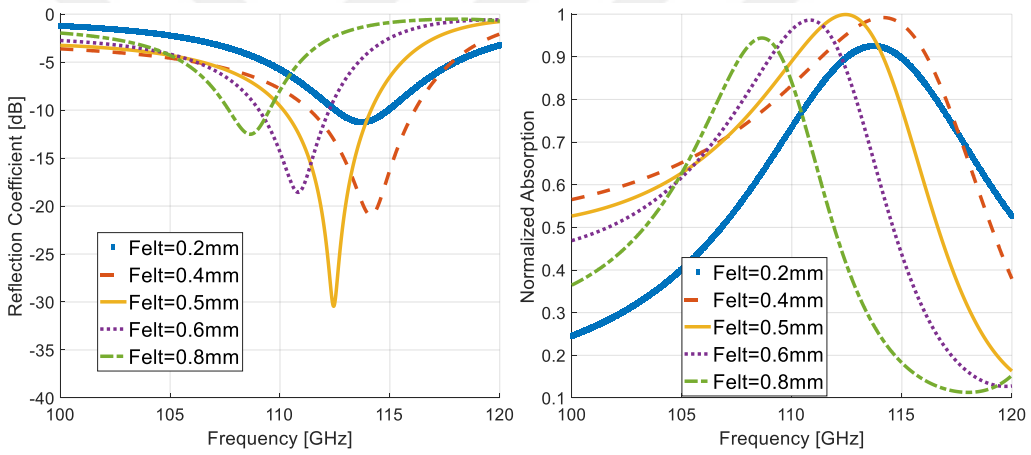

a) b)

Figure 47. The effects of the substrate thickness on textile-based 6G MMA a) reflection coefficients b) normalized absorption rates

3.8.5. Effects of angles of incidence on 6G MMA

In MMAs, dealing with diverse incidence angles is critical, as the incident waves can travel at varying angles and the absorption rates are greatly affected. Several parametric studies are carried out with numerical plane-wave computations to observe the absorptivity rates at various angles of incidence.

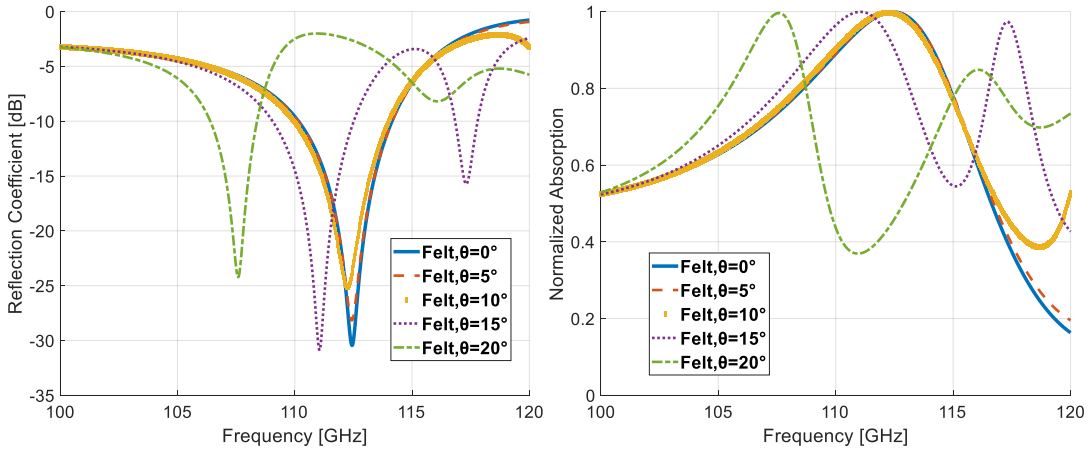

a) b)

Figure 48. The effects of the different incident angles on textile-based 6G MMA a) reflection coefficient b) normalized absorption

As seen in Fig. 48, increasing the incidence angle has great effects on the reflection coefficients and the average absorption rates. For an incident angles in the range 0°-10°, the proposed MMA preserves the absorption bandwidth about 2 GHz and for incident angles in the range θ= 15°-20°, the proposed MMA's operating frequency is shifted to the lower frequencies. But even for a 15° and 20° the proposed 6G MMA still preserves its absorption rate close to unity with a 99.7%.

3.8.6. Bending effects on 6G MMA

One of the major strengths of textile-based materials is their elasticity, for that this part emphasizes the effects of bending scenarios on the textile-based dielectric material MMA. The flexibility of the structure in textiles can influence the absorption and the impedance matching of the structure, thus numerous numerical simulations are performed to evaluate the performance of absorption rates under different bending situations. The bending conditions were simulated with respect to the cylindrical bending as given in Fig. 49.

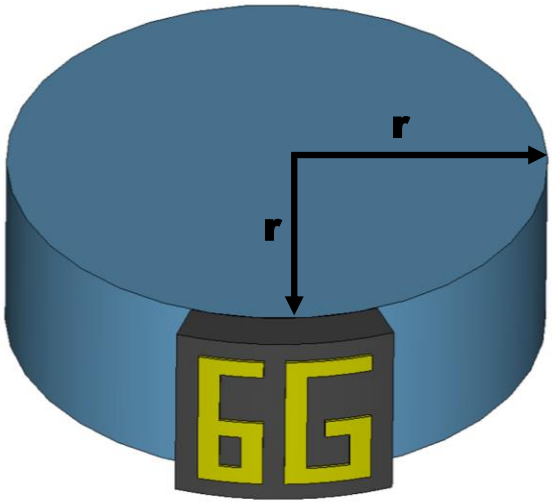

Figure 49. An illustration of cylindrical bending on textile-based 6G MMA.

As seen in Fig. 50, the cylindrical bending are performed for radii of 6 mm, 8 mm, 10 mm, 12 mm, 14 mm, 16 mm, respectively.

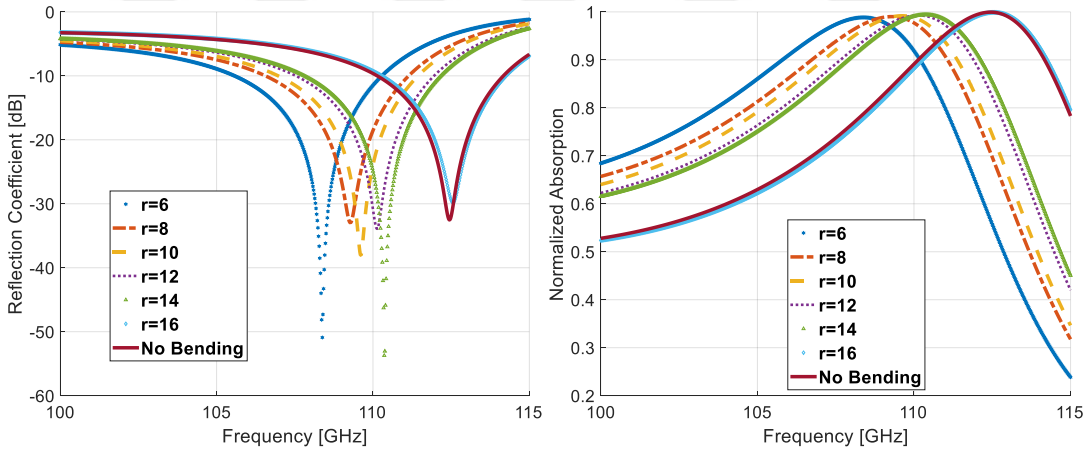

a) b)

Figure 50. The effects of the bending on textile-based 6G MMA a) reflection coefficient b) normalized absorption

A slight left-handed resonant frequency shift occurred in the cylindrical bent with radii between 6-16 mm, whereas a significant left-handed shift occurred in the cylindrical bent with radii of 6 mm. The trend in bandwidth and absorption can be expressed by the free-space matching impedance being influenced by the bending

operation and the impedance mismatching begins to advance with the increase in *r*-values.

3.8.7. Double verification of textile-based 6G MMA

In this part of the study, two numerical simulation tools (CST studio suite and Ansys HFSS) were run to confirm the obtained results and to understand whether the designed absorber is perfectly operating in the obtained operating frequencies. As shown in Fig. 51, the suggested textile-based 6G MMA works flawlessly and produces comparable results using both simulation tools.

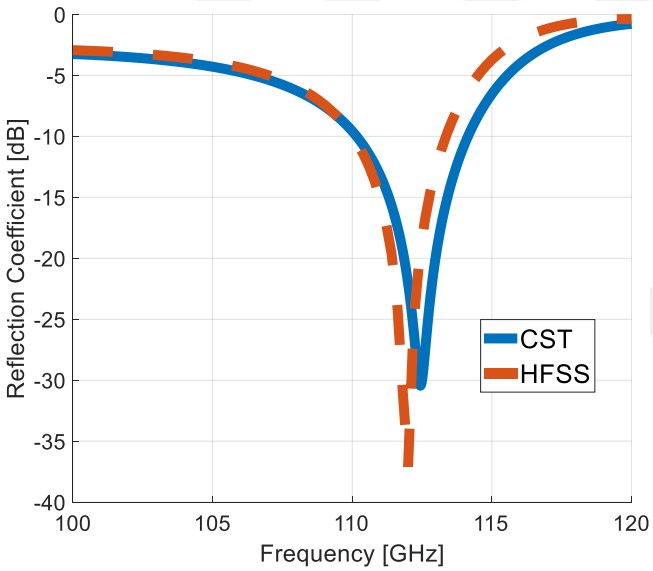

Figure 51. The reflection coefficients of proposed 6G MMA using two different simulation tools.

3.8.8. Conclusion of 6G MMA Design

In this study a novel textile-based ultra-thin MMA is developed for 6G mm-wave applications (in the range from 110 GHz to 114 GHz). The developed unit cell consist of the combination of number 6 and the letter G on the grounded Felt substrate. The achieved results indicate that the proposed MMA operates in the frequency range of 110-114 GHz with high absorptivity rate roundly 99.68%.

Achieved results proved that the bending conditions and different angles of incidence affect the performance of the suggested MMA since the absorption rate of MMA is dropped about 1.45% and shifted to another frequencies. The comparison and simulation of two different simulation software are performed to analyze the boundary condition and to confirm the performance of the suggested design. The obtained results show very slight differences which is retained to the different numerical methods and to the numerical accuracies and errors in both methods.

3.9. Experimental verification of G&S MMA

Summary: Our target is to confirm the obtained theoretical results by lab measurements. In this part the developed unit cell of G&S MMA is optimized and tuned according to the facilities of fabrication criteria. The operating frequency of designed MMA shifted from 18-26 GHz to the operating frequency of 10 - 13.8 GHz, to smoothly measure the proposed MMA with the available VNA, as the probes of horn antennas did not support higher frequencies.

The structure of this experimental study is as follows:

1) The fabrication of the proposed unit cell G&S MMA

2) Simulation results and la measurements

3) Effects of incident angles on the fabricated G&S MMA

3.9.1. Proposed unit cell of fabricated G&S MMA

In this part of this study the tuned and optimized values of the redeveloped G&S MMA unit cell were given in the Fig. 52 and Table. 25.

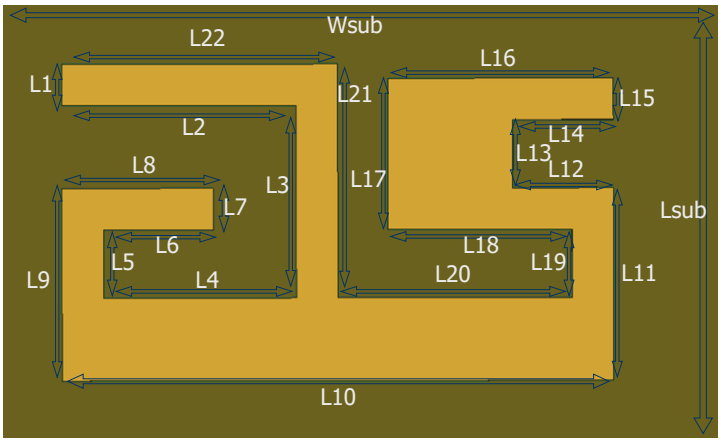

Figure 52. The redeveloped fabricated G&S MMA unit cell with design parameters.

Table 25. Design parameters of redeveloped fabricated G&S MMA.

Parameters	**L_1**	**L_2**	**L_3**	**L_4**	**L_5**
Value (mm)	0.4728	2.6714	2.1986	2.1986	0.7802
Parameters	**L_6**	**L_7**	**L_8**	**L_9**	**L_{10}**
Value (mm)	1.2529	0.4782	1.7258	2.1986	6.2885
Parameters	**L_{11}**	**L_{12}**	**L_{13}**	**L_{14}**	**L_{15}**
Value (mm)	2.1986	1.1505	0.7802	1.1505	0.4728
Parameters	**L_{16}**	**L_{17}**	**L_{18}**	**L_{19}**	**L_{20}**
Value (mm)	2.5690	1.7258	2.0962	0.7802	2.6714
Parameters	**L_{21}**	**L_{22}**	**W_{sub}**	**L_{sub}**	**H_{sub}**
Value (mm)	2.6714	3.1442	9.1259	5.5704	2.4000

As stated in Table. 25, the re-developed unit cell is much wider, longer, and thicker than the first developed MMA as the facilities of fabrication requires lower frequencies.

3.9.2. Simulation Results of Fabricated G&S MMA

This part belongs to the comparison of simulated and measured results. To fabricate a design of redeveloped MMA, a 20 x 20-unit cell structure was created and fabricated on FR-4 with a thickness of 2.4 mm. The structure was created with a use

of CST Studio, and the created 20 x 20 design was exported as a step file. In addition to these, a CNC routing machine etched the FR-4 plate with respect to the step file of 20 x 20-unit cell.

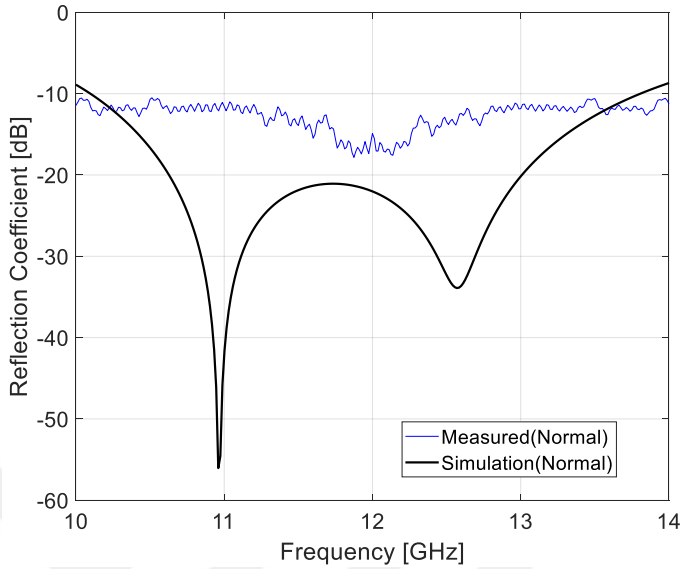

Figure 53. The fabricated G&S MMA unit cell comparison with measured and simulated results.

As shown in Fig. 53, the fabricated absorber have wideband absorption property and also had similar results of simulation. The outcomes of this study indicate that the proposed novel MMA could smoothly operates in the desired frequency spectrum.

3.9.3. Laboratory setup of fabricated G&S MMA

The fabricated G&S MMA is measured on the special laboratory setup with a laboratory equipment's of VNA, transmitting and receiving horn antennas, and the DUT which is centered in the middle of setup. The image of fabricated metamaterial absorber and representation of the laboratory setup is given in Fig. 54 and 55.

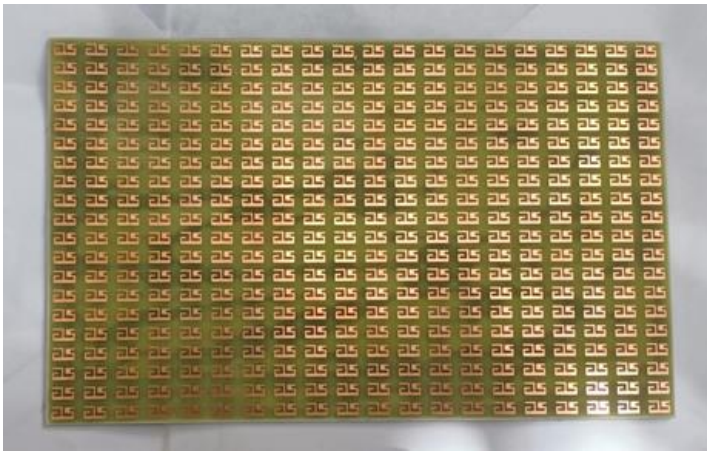

Figure 54. The fabricated G&S MMA.

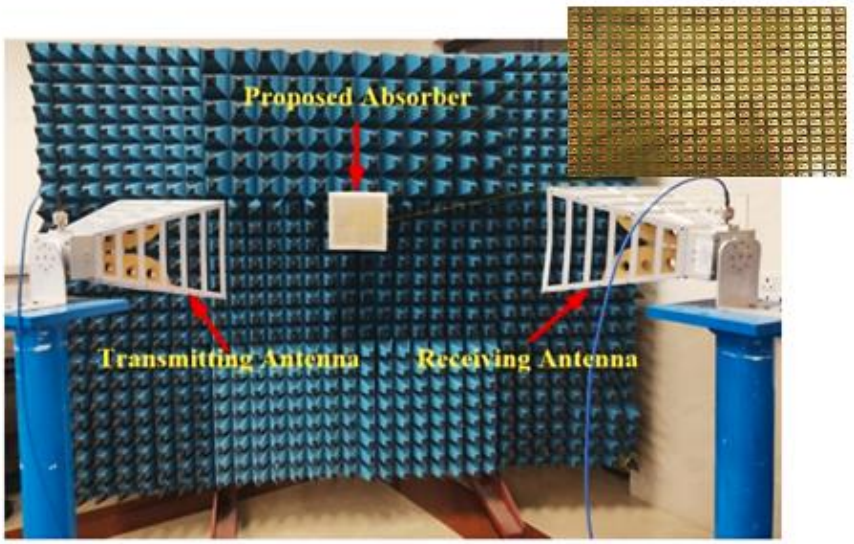

Figure 55. The representation of laboratory setup.

3.9.4. Effect of the incident angles on fabricated G&S MMA

To analyze and compare the fabricated and simulated absorbers operating under different oblique incident angles, various measurements and plane-wave simulations were done. The fabricated 20 x 20 cm absorber design is faced with the

oblique incident angle up to 45^0 while the simulations were also computed in that frequency. The outcomes of the 45^0 incident angle measurements and effects of oblique incident angles on measured and simulated results of the absorber are given in Fig. 56.

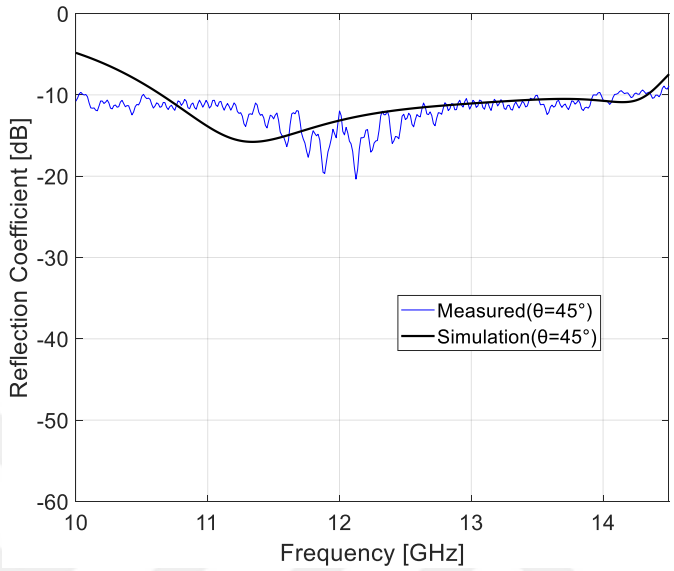

Figure 56. The effects of oblique incident angle on fabricated and simulated reflection coefficients.

3.9.5. Conclusion of Experimental Verifications

With this experimental setup we proved that our simulated results of the proposed absorber are matched with the fabricated absorber and operates on the desired operating frequency ranges. The outcomes of the measurements proved that changing the incident angles, the fabricated absorber can smoothly absorb the electromagnetic waves with a high absorptivity rates. A common bandwidth of 3.42 GHz is found according to the measurements of this fabricated absorber.

CHAPTER 4: CONCLUSION

The continuous development of modern technologies and today's demands of new materials beyond the existential opened a new field of utilization for the use of metamaterials. The extraordinary features of metamaterials made them essential substances for supplying extra demands for various applications and technologies. Traditional and bulky conventionally developed absorbers cannot supply the enormous demands of absorption requirements in modern applications. This led to the evolution of metamaterial-based absorbers with their new capabilities and perfect absorption rates of ambient electromagnetic waves. Many types of metamaterial-based absorbers can be developed on rigid PCB based conventional materials and on flexible materials (e.g., smart textile). However, most of the developed and published metamaterial-based absorbers are not successfully providing the wide and ultra-wideband necessities of absorbers, low abruption rates in addition to their large sizes and they do not operate at higher frequencies as of today's communication requirements. Even though, some of the published PCB-based rigid conventional symmetrical metamaterial absorbers are successfully absorbing ambient electromagnetic waves with higher rates, they are not operating over wide bandwidths. Conversely, the asymmetrical conventional rigid metamaterial absorbers show the wide bandwidth behaviors, but they are efficient at higher incident angles of electromagnetic waves.

The problems of low absorption efficiencies at higher angles of incidence and the narrow operating bandwidths are not solved properly. The main motivation of this thesis is to develop novel wideband, ultra-wideband metamaterial-based absorbers (PCB and smart textile-based) that can fit the demands of today's and future's modern application requirements at the mm-wave ranges.

In this thesis, the designed metamaterial-based absorbers are specifically developed to fit for the usage with 5G, 6G, mm-Wave and RF energy harvesting applications. The wideband and ultra-wideband properties with high absorptivity rates are achieved for a both the conventional rigid PCB and textile-based dielectric materials.

The first study of this thesis which is named as “PCB-Based A Novel 5G Wideband Metamaterial Based Absorber for Microwave Energy Harvesting Applications”, shows that the designed special novel geometry of combined letter-shape (G&S) patch perfectly operates on FR-4 based developed absorber which can absorb over a bandwidth of about 8.6 GHz, in the frequency range from 18 GHZ to 26.6 GHz. Replacing the FR4 dielectric with Rogers RT5880 shows that the operating bandwidth can be enhanced and reaches about 9 GHz in the range from 21 GHz to 30 GHz with average of absorption rates of about 96% (FR4) and 99% (Rogers RT5880), respectively. Both absorbers are properly operating with different angles of incidence in the range θ=0-30 degrees.

In the second study of this thesis which is named “PCB-Based Multiband Double-Layered Metamaterial Based Perfect Absorber for Microwave Energy Harvesting Applications”, our target was to study the effect of double layers on the absorption rates and the operating bandwidth. We aimed also to further enhance both the operation bandwidth and the absorptivity rates using a double-layered absorber structure and to examine the design parameters. The absorber is designed and operates over a frequency range from 26 GHz to 42 GHz with triple-band absorption peak of about 99.98%. This double-layered design proved that an absorber which has single band feature could extended to multiband with a multi-layer structure design.

For the “Development of Ultra-Wideband Textile-Based Metamaterial Absorber for mm-wave Band Applications” study, the outcomes are clearly indicating that the use of different textile-based substrates led the way for the development of a state-of-the-art textile-based ultra-wideband mm-wave absorbers. The developed Felt fabric absorber is operating over the frequency range from 32.32 to 49.44 GHz with an average absorption rate of 99%. Apart from the ultra-wideband feature of this developed absorber, it has only 1.0 mm thickness. The other parametric studies showed that the Denim and Polyester fabrics are also good candidates for ultra-wideband absorbers. The parametric studies of this study demonstrated that the developed absorber could absorb at different angle of incidences up to 30 degrees and under different bending conditions.

After the development of the first textile-based ultra-wideband MM absorber, the possibility of PCB-based ultra-wideband is examined and a novel design is

developed for the fourth study of this thesis which is “A PCB-based Novel Ultra-Wideband Metamaterial-Based Perfect Absorber for 5G Millimeter-Wave Applications”. In this study a novel ultra-thin, ultra-wideband MM absorber is developed for 5G mm-wave applications which operates from 27.67 GHz to 43.87 GHz with an average absorption rate of 96.995%. The outcomes of this study showed that a design of ultra-wideband PCB-based MMA can be achieved with a proper geometry and side patches.

The fabrication and the usage of symmetrical absorbers is sometimes preferable, so to take advantage of the symmetrical absorber geometries, a novel symmetrical design is developed and then the bandwidth of this symmetrical design is improved on the next study of this thesis which is named as “Development of metamaterial absorber with lumped elements for the bandwidth improvements in usage of 5G millimeter-wave applications”. This study proved that the use of lumped resistive resistor elements improves the fractional bandwidth of the absorber from 0.104% to 19.50% with an average absorption rate of 98% which operated on the frequency range of 25.96 GHz to 31.57 GHz. These results are very promising for the future’s symmetrical PCB-based ultra-wideband absorbers.

In a study named “Development of a novel ultra-wideband textile-based metamaterial absorber for mm-wave band applications”, a novel textile-based MMA is developed for the mm-wave applications which operates at the frequency range from 32.92 GHz to 55.08 GHz with an average absorption rate of 94%. The outcome of this study also proves that the utilization of the other fabrics also enhances the ultra-wideband feature with a fractional bandwidths of above 41.42% in comparison to the traditional PCB based absorbers. Even for different angles of incidence and under different bending conditions, the textile-based absorber preserves its ultra-wideband property with about of 92% absorption rate on the incident angle of θ=20-25 degrees.

For the achievement of symmetrical ultra-wideband textile-based MMA the study of “Development of a Split-Ring-Resonator Based Ultra-Wideband Textile-Based Metamaterial Absorber for Millimeter-Wave Applications” shows that the Felt fabric and the resistive lumped elements could enhance the narrow bandwidth of the SRR absorber. The fractional bandwidth is increased by a factor of approximately 112.34. The developed textile-based SRR absorber operates from 24.49 GHz to 60.98

GHz with an average absorption rate of 85.38% which is very suitable for higher frequencies of mm-wave smart-wearable applications.

Future 6G based applications require developing flexible absorbers, for this task a study named “A novel textile-based 6G metamaterial absorber for 6G mm-wave applications’ is the first textile-based 6G mm-wave metamaterial absorber. The design is based on the combination of the number “6” and the letter “G”. The obtained average absorption rate is about 99.68% and the operating frequencies are from 110 GHz to 114 GHz. The achieved results proves that the bending of the flexible absorber and facing with different oblique incidences above 20 degrees do not greatly affect the performance of the MMA, the absorption rates decrease by a about 1.45%.

The developed absorbers in this work are designed to solve the issues of the previously developed absorbers which are mainly, the narrow bandwidths, being not operating at higher frequencies of 5G mm-wave applications, narrow bandwidths of textile-based absorbers, narrow bandwidths of symmetrical designs, lower absorption rates of textile-based absorbers, narrow bandwidth of textile-based SRR designs, and the lack of absorbers for 6G applications.

The final part of this thesis includes the experimental verification of the first developed absorber in order to confirm the obtained simulated results. The available fabrication possibilities and the existing measurement facilities required new optimized absorber design to operate at lower frequencies. The absorber design is re-optimized for the existing laboratory setup since the VNA did not support the mm-wave spectrum. The operation frequency of the re-optimized G&S absorber is 10-13.8 GHz for the normal incidence angle and for the 45-degree incidence angle where a common bandwidth of 3.42 GHz is achieved.

With a development of this absorbers and studies, in this thesis the deficiencies of the conventional metamaterial absorbers were filled, and great enhancements are achieved. The outcomes of this studies prove that with a usage of ultra-wideband, compact sized, low-profile PCB and textile-based absorbers will be fully adequate for today’s 5G applications and future’s wearable smart applications.

Herein, this thesis deeply investigated and analyzed the physical properties of the textile-based fabric dielectric materials for different bending conditions to control characteristics of absorbers' when the developed textile-based absorbers are

implemented on textile applications. The results of this textile-based absorbers are found out that under extreme increase in the curvature of the material, the absorption bandwidth and absorption rates are remarkably decreased but under lower curvature rates or normal bending conditions of the proposed absorbers, they still preserve their proper features.

In this thesis, various absorbers were developed for 5G, 6G, mm-wave and harvesting applications. The obtained designs and results of this study confirmed that the obtained designs are of ultra-wideband and wide-angle metamaterial absorbers. This ultra-high frequency and high absorption rates can be achieved with the employment of textile-based fabrics exploiting of their low dielectric constants and losses. The obtained designs are very important for the military camouflage applications and personal monitoring of the health, tracking of the location and self-consistent-smart-wearable applications which will be possible with the use of textile-based metamaterial absorbers.

REFERENCES

Achard, F. (2005), *James clerk maxwell, a treatise on electricity and magnetism, first edition (1873)*, Landmark Writings in Western Mathematics 1640-1940, No. 1873, pp. 564–587.

Akarsu, G., Taher, H., Zengin, E.B., Nakmouche, M.F., Fawzy, D.E., Allam, A.M.M.. and Cleary, F. (2022), *Development of Ultra-Wideband Textile-Based Metamaterial Absorber for mm-wave Band Applications*, 2022 16th European Conference on Antennas and Propagation (EuCAP), pp. 1–5.

Almoneef, T.S. and Ramahi, O.M. (2013), *Harvesting electromagnetic energy using metamaterial particles*, IEEE Antennas and Propagation Society, AP-S International Symposium (Digest), IEEE, pp. 1046–1047.

Amer, A.A.G., Sapuan, S.Z., Nasimuddin, N., Alphones, A. and Zinal, N.B. (2020), *A comprehensive review of metasurface structures suitable for RF energy harvesting*, IEEE Access, Vol. 8, pp. 76433–76452.

Andrews, J.G., Buzzi, S., Choi, W., Hanly, S. V., Lozano, A., Soong, A.C.K. and Zhang, J.C. (2014), *What will 5G be?*, IEEE Journal on Selected Areas in Communications, IEEE, Vol. 32, No. 6, pp. 1065–1082.

Bait-Suwailam, M.M., Almoneef, T.S. and Alomainy, A. (2019), *A wearable reconfigurable electromagnetic metamaterial absorber using artificial magnetic inclusions*, 2019 IEEE International Symposium on Antennas and Propagation and USNC-URSI Radio Science Meeting, APSURSI 2019 - Proceedings, Vol. 1, pp. 1623–1624.

Brown, W.C. (1969), *Experiments Involving a Microwave Beam to Power and Position a Helicopter*, IEEE Transactions on Aerospace and Electronic Systems, Vol. AES-5, No. 5, pp. 692–702.

Campo, E.A. (2008), *Electrical Properties of Polymeric Materials*, Selection of Polymeric Materials, Elsevier, pp. 141–173.

Caspers, F. (2012), *RF engineering basic concepts : S-parameters*, CAS - CERN Accelerator School: RF for Accelerators, pp. 67–93.

Chambers, B. and Tennant, A. (2006), *Active Dallenbach radar absorber*, 2006 IEEE Antennas and Propagation Society International Symposium, IEEE, pp. 381–384.

Chen, T., Li, S. and Sun, H. (2012), *Metamaterials application in sensing*, Sensors, Vol. 12, No. 3, pp. 2742–2765.

Cheng, Y.Z., Fang, C., Zhang, Z., Wang, B., Chen, J. and Gong, R.Z. (2016), *A compact and polarization-insensitive perfect metamaterial absorber for electromagnetic energy harvesting application*, 2016 Progress In Electromagnetics Research Symposium, PIERS 2016 - Proceedings, IEEE, Vol. 1, pp. 1910–1914.

Clemens, M. and Weiland, T. (2001), *Discrete electromagnetism with the finite integration technique*, Progress in Electromagnetics Research, Vol. 32, pp. 65–87.

Costa, F., Monorchio, A. and Manara, G. (2016), *Theory, design and perspectives of electromagnetic wave absorbers*, IEEE Electromagnetic Compatibility Magazine, IEEE, Vol. 5, No. 2, pp. 67–74.

Courant, R. (1943), *Variational methods for the solution of problems of equilibrium and vibrations*, Bulletin of the American Mathematical Society, American Mathematical Society, Vol. 49, No. 1, pp. 1–23.

Cummer, S.A., Christensen, J. and Alù, A. (2016), *Controlling sound with acoustic metamaterials*, Nature Reviews Materials, Vol. 1, No. 16001,.

Din, N.M., Chakrabarty, C.K., Bin Ismail, A., Devi, K.K.A. and Chen, W.Y. (2012), *Design of RF energy harvesting system for energizing low power devices*, Progress in Electromagnetics Research, Vol. 132, No. September, pp. 49–69.

Diouf, B. and Pode, R. (2015), *Potential of lithium-ion batteries in renewable energy*, Renewable Energy, Elsevier Ltd, Vol. 76, pp. 375–380.

Dong, Y. and Itoh, T. (2012), *Metamaterial-Based Antennas*, IEEE, Vol. 100, No. 7, pp. 2271–2285.

Freire, M.J., Marques, R. and Jelinek, L. (2011), *Experimental demonstration of a = 1 metamaterial lens for magnetic resonance imaging Experimental demonstration of a = − 1 metamaterial lens for magnetic*, Vol. 231108, No. 2008, pp. 2006–2009.

Georgiadis, A., Collado, A. and Tentzeris, M.M. (2021), *Energy Harvesting*,

Cambridge University Press.

Gil, M., Bonache, J., García-García, J., Martel, J. and Martín, F. (2007), *Composite right/left-handed metamaterial transmission lines based on complementary split-rings resonators and their applications to very wideband and compact filter design*, IEEE Transactions on Microwave Theory and Techniques, Vol. 55, No. 6, pp. 1296–1303.

Ha, D.T., Tung, B.S., Khuyen, B.X., Pham, T.S., Tung, N.T., Tung, N.H., Hoa, N.T., Lam, V.D., Zheng, H., Chen, L. and Lee, Y., (2021), *Dual-Band, Polarization-Insensitive, Ultrathin and Flexible Metamaterial Absorber Based on High-Order Magnetic Resonance*. In Photonics Vol. 8, No. 12, pp. 574-574.

Hannan, S., Islam, M.T., Hoque, A., Singh, M.J. and Almutairi, A.F. (2019), *Design of a novel double negative metamaterial absorber atom for Ku and K band applications*, Electronics (Switzerland), Vol. 8, No. 8, pp. 1–16.

Hoffman, A.J., Alekseyev, L., Howard, S.S., Franz, K.J., Wasserman, D., Podolskiy, V.A., Narimanov, E.E., Sivco, D.L. and Gmachl, C., (2007). *Negative refraction in semiconductor metamaterials*. Nature materials, 6(12), pp.946-950.

Iwaszczuk, K., Strikwerda, A.C., Fan, K., Zhang, X., Averitt, R.D. and Jepsen, P.U. (2012), *Flexible metamaterial absorbers for stealth applications at terahertz frequencies*, Optics Express, Vol. 20, No. 1, pp. 635-635.

Jeong, E., Tak, J. and Choi, J. (2016), *A metamaterial absorber for reducing false image in 24GHz automotive radar system*, 2015 International Symposium on Antennas and Propagation, ISAP 2015, The Institute of Electronics, Information and Comm, pp. 14–16.

Karaaslan, M., Bağmancı, M., Ünal, E., Akgol, O., Altıntaş, O. and Sabah, C. (2018), *Broad band metamaterial absorber based on wheel resonators with lumped elements for microwave energy harvesting*, Optical and Quantum Electronics, Springer US, Vol. 50, No. 5, pp. 1–18.

Karaaslan, M., Bağmancı, M., Ünal, E., Akgol, O. and Sabah, C. (2017), *Microwave energy harvesting based on metamaterial absorbers with multi-layered square split rings for wireless communications*, Optics Communications, Vol. 392, No. September 2016, pp. 31–38.

Khanna, Y. and Awasthi, Y.K. (2020), *Wideband ultra-thin metamaterial absorber for Ku K-band applications*, 2020 7th International Conference on Signal Processing and Integrated Networks, SPIN 2020, No. 1, pp. 367–371.

Knott, E.F. and Lunden, C.D. (1995), *The two-sheet capacitive Jaumann absorber*, IEEE Transactions on Antennas and Propagation, Vol. 43, No. 11, pp. 1339–1343.

Lai, A., Caloz, C. and Itoh, T. (2004), *Composite right/left-handed transmission line metamaterials*, IEEE Microwave Magazine, IEEE, Vol. 5, No. 3, pp. 34–50.

Landy, N.I., Sajuyigbe, S., Mock, J.J., Smith, D.R. and Padilla, W.J. (2008), *Perfect metamaterial absorber*, Physical Review Letters, Vol. 100, No. 20.

Lu, X., Wang, P., Niyato, D., Kim, D.I. and Han, Z. (2015), *Wireless networks with rf energy harvesting: A contemporary survey*, IEEE Communications Surveys and Tutorials, IEEE, Vol. 17, No. 2, pp. 757–789.

Lv, H., Yang, Z., Ong, S.J.H., Wei, C., Liao, H., Xi, S., Du, Y., Ji, G. and Xu, Z.J. (2019), *A Flexible Microwave Shield with Tunable Frequency-Transmission and Electromagnetic Compatibility*, Advanced Functional Materials, Vol. 29, No. 14, pp. 1–8.

Marklein, R. (2002), *The Finite Integration Technique as a General Tool to Compute Acoustic , Electromagnetic , Elastodynamic , and Coupled Wave Fields*, Review of Radio SCience: 1999-2002 URSI, pp. 201–244.

Munk, B.A., Munk, P. and Pryor, J. (2007), *On Designing Jaumann and Circuit Analog Absorbers (CA Absorbers) for Oblique Angle of Incidence*, IEEE Transactions on Antennas and Propagation, Vol. 55, No. 1, pp. 186–193.

Pendry, J.B. (2000), *Negative refraction makes a perfect lens*, Physical Review Letters, Vol. 85, No. 18, pp. 3966–3969.

Pendry, J.B., Holden, A.J., Robbins, D.J. and Stewart, W.J. (1998), *Low frequency plasmons in thin-wire structures*, Journal of Physics Condensed Matter, Vol. 10, No. 22, pp. 4785–4809.

Pendry, J.B., Holden, A.J., Robbins, D.J. and Stewart, W.J. (1999), *Magnetism from conductors and enhanced nonlinear phenomena*, IEEE Transactions on Microwave Theory and Techniques, Vol. 47, No. 11, pp. 2075–2084.

Perhirin, S. and Auffret, Y. (2013), *A low consumption electronic system developed for a 10km long all-optical extension dedicated to sea floor observatories using power-over-fiber technology and SPI protocol*, Microwave and Optical Technology Letters, Vol. 55, No. 11, pp. 2562–2568.

Piñuela, M., Mitcheson, P.D. and Lucyszyn, S. (2013), *Ambient RF energy harvesting in urban and semi-urban environments*, IEEE Transactions on Microwave Theory and Techniques, Vol. 61, No. 7, pp. 2715–2726.

Ramya, S. and Srinivasa Rao, I. (2017), *A compact ultra-thin ultra-wideband microwave metamaterial absorber*, Microwave and Optical Technology Letters, Vol. 59, No. 8, pp. 1837–1845.

Root, D.E., Verspecht, J., Horn, J. and Marcu, M. (2013), *S-parameters – a concise review*, X-Parameters, Cambridge University Press, pp. 1–19.

Rufangura, P. and Sabah, C. (2015), *Dual-band perfect metamaterial absorber for solar cell applications*, Vacuum, Elsevier Ltd, Vol. 120, pp. 68–74.

Saad, W., Bennis, M. and Chen, M. (2020), *A Vision of 6G Wireless Systems: Applications, Trends, Technologies, and Open Research Problems*, IEEE Network, IEEE, Vol. 34, No. 3, pp. 134–142.

Schurig, D., Mock, J.J., Justice, B.J., Cummer, S.A., Pendry, J.B., Starr, A.F. and Smith, D.R. (2006), *Metamaterial electromagnetic cloak at microwave frequencies*, Science, Vol. 314, No. 5801, pp. 977–980.

Sevgi, L. (2014), *FDTD-Based Metamaterial (MTM) Modeling and Simulation*, Vol. 56, No. 5, pp. 289–303.

Shelby, R.A., Smith, D.R. and Schultz, S. (2001), *Experimental verification of a negative index of refraction*, Science, Vol. 292, No. 5514, pp. 77–79.

Singh, A.K., Abegaonkar, M.P. and Koul, S.K. (2018), *Penta band polarization insensitive metamaterial absorber for EMI/EMC reduction and defense applications*, IEEE MTT-S International Microwave and RF Conference, IMaRC 2017, IEEE, pp. 243–246.

Smith, D.R., Padilla, W.J., Vier, D.C., Nemat-Nasser, S.C. and Schultz, S. (2000), *Composite medium with simultaneously negative permeability and permittivity*,

Physical Review Letters, Vol. 84, No. 18, pp. 4184–4187.

Taflove, A. (1980), *Application of the Finite-Difference Time-Domain Method to Sinusoidal Steady-State Electromagnetic-Penetration Problems*, IEEE Transactions on Electromagnetic Compatibility, Vol. EMC-22, No. 3, pp. 191–202.

Tak, J. and Choi, J. (2017), *A Wearable Metamaterial Microwave Absorber*, IEEE Antennas and Wireless Propagation Letters, IEEE, Vol. 16, pp. 784–787.

Tao, H., Landy, N.I., Bingham, C.M., Zhang, X., Averitt, R.D. and Padilla, W.J. (2008), *A metamaterial absorber for the terahertz regime: design, fabrication and characterization*, Optics Express, Vol. 16, No. 10, pp. 7181.

Tröltzsch, U., Kanoun, O. and Tränkler, H.R. (2006), *Characterizing aging effects of lithium ion batteries by impedance spectroscopy*, Electrochimica Acta, Vol. 51, No. 8–9, pp. 1664–1672.

Turnbull, G. (2013), *Maxwell's equations [Scanning our Past]*, Proceedings of the IEEE, Vol. 101, No. 7, pp. 1801–1805.

Veselago, V.G. (1968), *Electrodynamics of substances with simultaneously negative and.* Usp. fiz. nauk, Vol. 92 No 7, pp. 511-514.

Wang, B., Teo, K.H., Nishino, T., Yerazunis, W., Barnwell, J. and Zhang, J. (2011), *Experiments on wireless power transfer with metamaterials*, Applied Physics Letters, Vol. 98, No. 25, pp. 1–4.

Wartak Marek S., Tsakmakidis Kosmas L. and Hess Ortwin. (2011), *Physics in Canada.*, Physics in Canada, Canadian Association of Physicists, Vol. 50, No. 27, pp. 30–34.

Watts, C.M., Liu, X. and Padilla, W.J. (2012), *Metamaterial electromagnetic wave absorbers*, Advanced Materials, Vol. 24, No. 23.

Weiland, T. (1977), *A discretization model for the solution of Maxwell's equations for six-component fields*, Archiv Elektronik Und Uebertragungstechnik, Vol. 31, pp. 116–120.

Xin, W., Binzhen, Z., Wanjun, W., Junlin, W. and Junping, D. (2017), *Design, Fabrication, and Characterization of a Flexible Dual-Band Metamaterial Absorber*,

IEEE Photonics Journal, Vol. 9, No. 4, pp. 1–12.

Yee, K.S. (1966), *Numerical Solution of Initial Boundary Value Problems Involving Maxwell's Equations in Isotropic Media*, IEEE Transactions on Antennas and Propagation, Vol. 14, No. 3, pp. 302–307.

Yoo, Y.J., Zheng, H.Y., Kim, Y.J., Rhee, J.Y., Kang, J.H., Kim, K.W., Cheong, H., Kim, Y.H. and Lee, Y.P. (2014), *Flexible and elastic metamaterial absorber for low frequency, based on small-size unit cell*, Applied Physics Letters, Vol. 105, No. 4.

APPENDIX

Appendix A: List of Publications from this work

Published in or submitted to indexed conference proceedings:

1. Akarsu, G., Nakmouche, M.F., Fawzy, D.E., Allam, A.M.M.A., Başköy, K. and Cengiz, M.F. (2021), *A novel 5G wideband metamaterial based absorber for microwave energy harvesting applications*. In 2021 8th International Conference on Electrical and Electronics Engineering (ICEEE), pp. 309-312.

2. G. Akarsu, M. F. Nakmouche, D. E. Fawzy, (2021), *Multiband Double Layered Metamaterial Based Perfect Absorber for Microwave Energy Harvesting Applications*, X. URSI (International Union of Radio Science) - TURKEY 2021 Scientific Congress, Gebze Technical University, Kocaeli.

3. Akarsu, G., Taher, H., Zengin, E.B., Nakmouche, M.F., Fawzy, D.E., Allam, A.M.M.A. and Cleary, F. (2022), *Development of Ultra-Wideband Textile-Based Metamaterial Absorber for mm-wave Band Applications*. 2022 16th European Conference on Antennas and Propagation (EuCAP), pp. 1-5.

4. Akarsu, G., Nakmouche, M. F., Fawzy, D. E., & Allam, A. M. M. A. (2022), *A Novel Ultra-Wideband Metamaterial-Based Perfect Absorber for 5G Millimeter-Wave Applications*. 2022 9th International Conference on Electrical and Electronics Engineering (ICEEE), pp. 129-132.

5. Akarsu, G., Zengin, E. B., Nakmouche, M. F., Cengiz, M. F., Fawzy, D. E., Allam, A. A., & Taher, H. (2022), *Development of A Symmetric Metamaterial Absorber with Bandwidth Improvements for 5G Millimeter-Wave Applications*. 2022 9th International Conference on Electrical and Electronics Engineering (ICEEE), pp. 112-116.

6. Akarsu, G., Cengiz, M. F., Fawzy, D. E., Zengin, E. B., Allam, A. A., Taher, H., ... & Nakmouche, M. F. (2022), *Development of A Novel Ultra-Wideband Textile-Based Metamaterial Absorber for mm-wave Band Applications*. 2022 International Workshop on Antenna Technology (iWAT), pp. 220-223.

7. G. Akarsu, M.F Cengiz, E. B. Zengin, D. E. Fawzy, A.M.M.A. Allam, H. Taher. (2022), *Development of A Symmetric Ultra-Wideband Textile-Based Metamaterial Absorber for Millimeter-Wave Applications*. (Presented at European Conference on Electronic Engineering 2022, Berlin, Germany)

8. G. Akarsu, M. F. Cengiz, D.E. Fawzy, A.M.M.A Allam, H. Taher. (2022), *Development of A Novel Textile- Based Metamaterial Absorber for 6G Applications*. (In Preparation)